January 2013

Impact Of Choices When Creating Average Proximity Soundings As Applied To Lp/cl/hp Supercell Environments

Alexander Zarnowski

Recommended Citation

Zarnowski, Alexander, "Impact Of Choices When Creating Average Proximity Soundings As Applied To Lp/cl/hp Supercell Environments" (2013). *Theses and Dissertations*. 1494.
https://commons.und.edu/theses/1494

IMPACT OF CHOICES WHEN CREATING AVERAGE PROXIMITY SOUNDINGS AS APPLIED TO LP/CL/HP SUPERCELL ENVIRONMENTS

by

Alexander Robert Zarnowski
Bachelor of Science, University of North Carolina at Charlotte, 2009

A Thesis

Submitted to the Graduate Faculty

of the

University of North Dakota

In partial fulfillment of the requirements

for the degree of

Master of Science

Grand Forks, North Dakota
May
2013

This thesis, submitted by Alexander Robert Zarnowski in partial fulfillment of the requirements for the Degree of Master of Science in Atmospheric Sciences from the University of North Dakota, has been read by the Faculty Advisory Committee under whom the work has been done, and is hereby approved.

Matthew S Gilmore

Dr. Matthew Gilmore, Chairperson

Mark Askelson

Dr. Mark Askelson, Committee Member

Dr. Jianglong Zhang, Committee Member

This thesis is being submitted by the appointed advisory committee as having met all of the requirements of the Graduate School at the University of North Dakota and is hereby approved.

Dr. Wayne E. Swisher,
Dean of the Graduate School

Enter the Date

PERMISSION

Title	Impact of Choices When Creating Average Proximity Soundings as Applied to LP/CL/HP Supercell Environments
Department	Atmospheric Sciences
Degree	Master of Science

In presenting this thesis in partial fulfillment of the requirements for a graduate degree from the University of North Dakota, I agree that the library of this University shall make it freely available for inspection. I further agree that permission for extensive copying for scholarly purposes may be granted by the professor who supervised my thesis work or, in his absence, by the Chairperson of the department or the dean of the Graduate School. It is understood that any copying or publication or other use of this thesis or part thereof for financial gain shall not be allowed without my written permission. It is also understood that due recognition shall be given to me and to the University of North Dakota in any scholarly use which may be made of any material in my thesis.

Signature: Alexander [illegible]
Date: May 1, 2013

TABLE OF CONTENTS

LIST OF FIGURES

LIST OF TABLES

ACKNOWLEDGMENTS

I wish to express my sincere appreciation to my advisor, Dr. Matthew Gilmore, and advisory committee, Dr. Mark Askelson and Dr. Jianglong Zhang, for their guidance and support during my time in the Atmospheric Sciences graduate program at the University of North Dakota. I would like to thank my Family for their continued support and words of encouragement throughout my time in the graduate program. The faculty in the Atmospheric Sciences department has given me the confidence and knowledge to be a successful scientist in the field. Thank you. I would like to thank my fellow graduate students that I can now call friends for spending late nights working on homework, projects, and coding together. Special thank you to Dr. Jason Naylor for his guidance and ideas while working in the Tornado research group. I am truly grateful for the opportunity and experience that the University of North Dakota's Atmospheric Sciences Department has given me.

ABSTRACT

The first half of this two-part study explores two ways of producing composite environmental soundings (feature averaging versus height averaging; FA vs. HA), why those composites differ from one another, how the compositing technique itself affects the resulting thermodynamic and wind parameters, and which technique results in preserving features. This exploration was applied to three groups of supercell proximity soundings: low-precipitation (LP), classic (CL), and high precipitation (HP) and the HA analysis from the Rasmusssen and Straka (RS98) paper are reanalyzed in both the FA and HA framework. The second half of this study investigates how well previously reported LP, CL, and HP supercell radar behavior (Beatty et al. 2009) is reproduced in an idealized three-dimensional cloud model using both the original and composite soundings.

Reanalyzing the results from RS98 in both HA and FA frameworks, the LP group of soundings have a mean mixed-layer LCL (MLLCL) and mean MLLFC that are both significantly different ($p < 0.05$) than those from the other sounding groups. Also, the HP group of soundings has a mean MLLFC that is significantly different ($p < 0.05$) than the means from the other sounding groups. The HP sounding mean BL to 9 km shear and mean 4-10 km shear magnitude are significantly different ($p < 0.05$; RS98 found $p < 0.02$) and the mean HP sounding 9-10 km storm relative wind is significantly different ($p < 0.02$) compared to the other sounding groups.

Wind parameters and thermodynamic parameters computed from surface-based parcels for both the FA and HA composite sounding lay within one standard deviation of the distribution mean for each sounding group and mixed-layer parcel parameters lay farther from the distribution mean. The FA soundings parameters are not consistently closer to distribution means despite features such as the capping inversion and low-level moisture being preserved better within the FA sounding. Using relative humidity for the LP and CL FA and HA soundings (and vapor pressure for the HP soundings) produces the largest CAPE and least CIN, although averaging water vapor mixing ratio is arguably the most accurate and appropriate.

From the dataset, 29 individual sounding cases were simulated--10 CL, 10 LP, and 9 HP supercells-- and only three storms in each class lasted at least 7200 seconds with an updraft helicity greater than 480 m^2 s^{-2}. Only two of these nine individual cases produced long lived supercells, one each from the LP and HP sounding classes, transitioned from a forward flank dominant to rear flank dominant maximum precipitation (following Beatty et al. 2009). The other seven cases maintained a forward flank dominant maximum precipitation. Compositing using only the three successful cases in each class only succeeded in producing long-lived supercells only for CL FA and HA composites and the HP HA composite. These cases produced forward flank dominant precipitation maximums, with no transition. Due to the lack of consistency in storm behavior within each class, it is concluded that cases should be simulated and studied individually, as compared to creating a composite sounding – particularly when studying environments with a very small sample size.

CHAPTER I

INTRODUCTION

Supercell thunderstorms are prolific severe weather producers capable of producing heavy rain, strong winds, damaging hail, and tornadoes. Supercells have distinct storm characteristics and form in environments that are distinct from other classes of moist convection (i.e. single cell thunderstorms and multicell thunderstorms; e.g., Weisman and Klemp 1982). The environments are known from rawindsonde (balloon sounding) measurements that have been collected across the United States since the late 1930's (NOAA 1997). Supercell thunderstorms form in conditionally unstable environments having large low-level vertical wind shear, a veering wind profile, and positive buoyancy (e.g., Weisman and Klemp 1982). This criterion is most prevalent in the Northern Hemisphere, located in the Plains of the United States. The most distinct difference relative to other storm types is supercells develop a dominant, singular, quasi-rotating updraft that sustains warm, moist inflow into the storm. Strong low-level vertical wind shear can lead to a strong midlevel mesocyclone after tilting/stretching of the vorticity (Wilhelmson and Klemp 1978), the result of which induces an upward-directed dynamic vertical pressure gradient forcing on the storm flanks and propagation to the right of the mean wind (Rotunno and Klemp 1985).

After initial radar observations of supercell storms in the 1950s and dynamic descriptions in the 1970s and 1980s, some subsequent research has focused on supercell subclasses that are, in part, distinguished by their visual characteristics. Donaldson and

Browning (1965) first documented the unusual visual differences between different types of supercell storms in Oklahoma on 26 May 1963. Donaldson and Browning (1965) documented that the supercell storm had a bell shape appearance--suggesting a lack of precipitation; they were later named “low precipitation supercells” (hereafter denoted LP). This bell shaped appearance for supercells was also documented by Davies-Jones et al. (1976), which occurred in central Oklahoma. LP supercells also have visually narrower central updraft regions with the precipitation core seen on radar being downwind of the central rotating updraft (Bluestein and Parks 1983). The other two classifications are classic (hereafter denoted CL) and high precipitation (hereafter denoted HP) supercells, schematics of which were developed by Moller et al. (1994; see Fig. 1) based upon photographs by storm observers and radar/satellite imagery. The CL supercell visually has the heaviest precipitation downwind of the cloud base or wall cloud region (updraft), which is consistent with the larger reflectivities being north or slightly downshear of the hook echo (updraft region) on radar. The most common supercell in the United States is the HP supercell, since most CL supercell thunderstorms evolve into HP supercells (Rasmussen and Straka 1998; hereafter RS98). HP supercells have more of a lima bean shape when viewing radar PPI displays, with heavier and a visually opaque precipitation region located upshear of the hook.

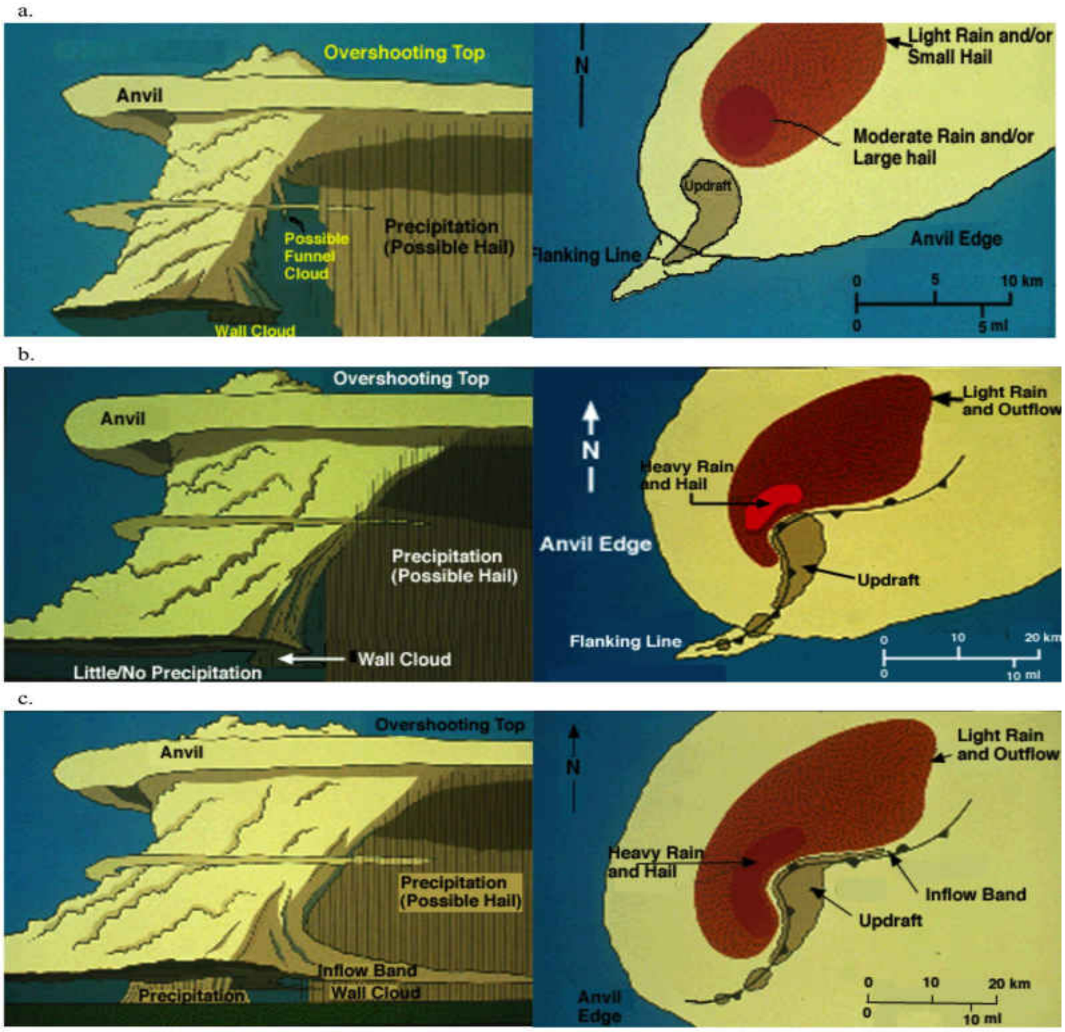

Fig 1. a) Visual side-view schematic of supercell storm cloud and precipitation (left) and associated low-level plan view radar/satellite and gust front schematic (right) for the a) Low-Precipitation Supercell, b) Classic Supercell, and c) High Precipitation Supercell. Reprinted from Moller et al. (1994)

Beatty et al. (2009) developed a semi-objective classification system using radar observations alone and found that the distance and direction between the updraft region, defined by the bounded weak echo region, and the precipitation echo centroid was distinctly different between HP supercells and CL/LP supercells. Both CL and LP supercells were found to have their main radar reflectivity echo centroid downshear of the hook, whereas HP supercells had their echo centroids upshear and much closer to the hook (Fig. 2). While their radar classification is robust, they concluded that further investigation is needed regarding the following microphysics observations across the supercell spectrum: occurrences of larger hail in LP supercell storms and raindrop size distribution for all supercells.

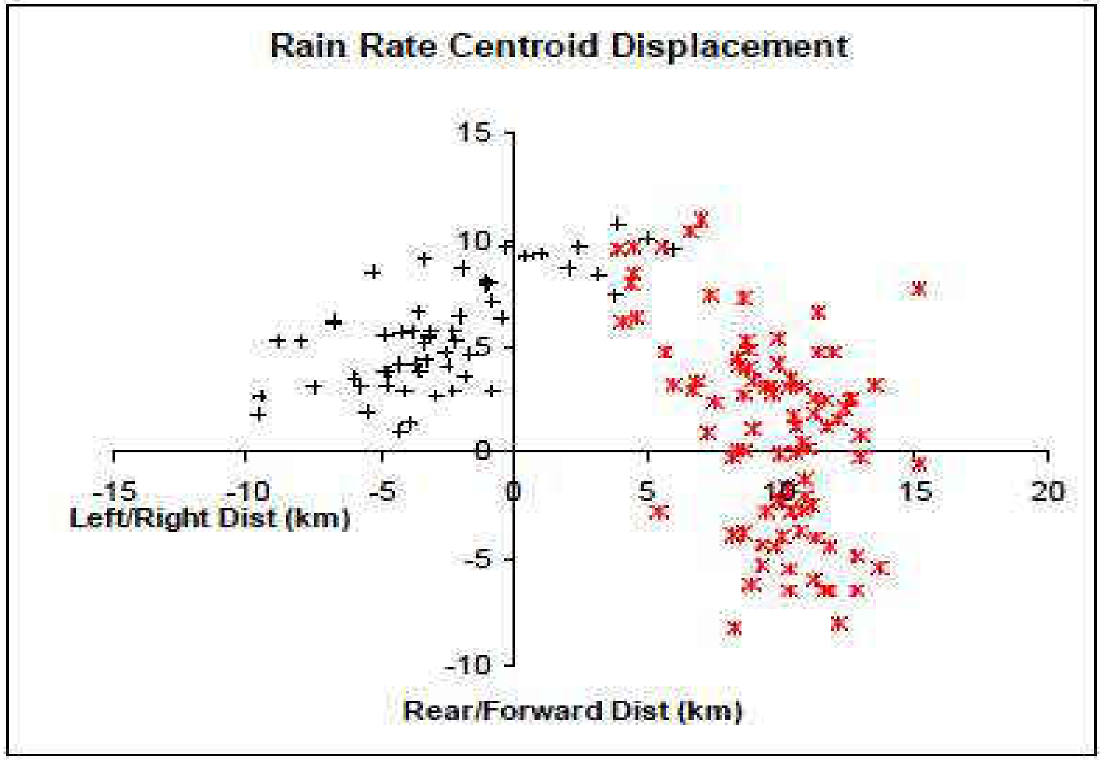

Fig 2. Location of updraft (origin) relative to the maximum rain rate centroid in visually confirmed HP supercells (black plus signs) and visually confirmed LP/CL supercells (red stars). Reprinted from Beatty et al. (2009).

The following, Table 1, will summarize the differences between each classification of supercell thunderstorms observed in nature. The differences range from spatial converge of precipitation, rain accumulation rates, visual differences in person, tornado occurrences, and differences in radar characteristics to name a few.

Table 1. Comparison of features of LP, CL, and HP supercells. LP features documented in Burgess and Davies-Jones (1979), Bluestein and Parks (1983), and Bluestein and Woodall (1990). CL features documented in Browning and Ludlam (1960,1962), Browning and Donaldson (1963), Browning (1965, 1977), Chisholm (1973), Browning and Foote (1976), Lemon and Doswell (1979), and Rotunno and Klemp (1985). HP features documented in Doswell (1985), Nelson (1987), Moller and Doswell (1988), Moller et al. (1990, 1994), Doswell et al. (1990), and Doswell and Burgess (1993).

	LP	Classic	HP
Ground Precip. compared to CL	Smaller	-------	Larger
Size of Precip. Echo compared to CL	Smaller	-------	Larger
Precip. Location w.r.t. updraft	Forward flank	Forward flank	Rear Flank
Shape of Hook Echo on Radar	-------	Fish Hook	Fat/Lima Bean
Hook Echo on Radar	Faint/None	Yes	No
Downdraft Strength	Weak	Moderate	Strong
Tornadoes	Rare	Yes	Yes
Tornado Location	Mid-level extension	Occlusion	Along gust front
Large Hail Possible	Yes	Yes	Yes
Hail Amount compared to CL	Less	-------	More
Most Frequent Geographic Location	High Plains	Great Plains	Eastern USA

a) Past modeling research relating the LP/CL/HP classification to microphysics treatment and initiation method

The storm environment helps determine storm type, mesocyclone strength and precipitation growth within the storm. However, the internal storm microphysics itself may strongly influence the supercell type. Several modeling studies, described below, have also noticed that varying the microphysics assumptions in the model may affect precipitation efficiency and behavior near ground. This strongly suggests that microphysics growth processes also affect the supercell classification and how quickly a storm can change classes. For the same storm environment, microphysics factors leading to LP-like behavior (Gilmore et al. 2004b) or CL behavior (van den Heever and Cotton 2004) occurs when hail/graupel hydrometeor size distributions are weighted more towards smaller-sized particles. Both Gilmore et al. (2004b) and van den Heever and Cotton (2004) found changes to the assumed hail size distribution impacts the size of the resulting hail, storm cold pool, and morphology of the simulated storm. In both studies, hail (approximately ≥ 7 mm) settings produced more accumulated rain and hail at the surface and were said to be more representative of an HP supercell – however only in the Gilmore et al. (2004b) case was the HP supercell associated with the coldest outflow (consistent with nature – RS98; Bunkers et al. 2000). The weakest and warmest cold pool (most consistent with an LP according to RS98) was found when using either small graupel (Gilmore et al. 2004b) or very large hail (Gilmore et al. 2004b and van den Heever and Cotton 2004).

In simulated supercells, the presence of ice will tend to produce stronger downdrafts due to hail shedding and melting compared to liquid-only schemes (Gilmore et al. 2004a). The types of hydrometeors present in the storm and number concentrations influence storm dynamics, cold pool propagation strength and depth, and characteristics (LP/CL/HP). In supercell simulation studies, changing the mean hail diameter affected the type of supercell (Gilmore et al 2004b; van den Heever and Cotton 2004). However, the results varied somewhat depending upon whether the intercept or slope was held constant (Gilmore et al. 2004c). Smaller-hail simulations sometimes produced stronger downdrafts in van den Heever and Cotton (2004) and sometimes weaker (Gilmore et al. 2004b). From model simulations, smaller-hail cases produce more CL or LP supercell characteristics, while larger hail cases produce HP supercell characteristics because more evaporation occurs owning to the shedding of the larger hail (Gilmore et al. 2004b; van den Heever and Cotton 2004).

In the smaller hail cases there can be more rapid melting, more complete melting, and greater rates of low-level evaporative cooling, resulting in stronger near surface downdrafts (van den Heever and Cotton 2004). For the smaller hail cases there was a spatially wider distribution of precipitation compared to the larger hail cases (van den Heever and Cotton 2004), in part due to stronger environmental winds. No matter what the wind shear, due to slower fall velocities, smaller hail/graupel also have more time to be advected and spread over a larger area (Gilmore et al 2004b).

Brooks and Wilhelmson (1992) simulated an LP supercell by using an artificially weakened triggering bubble, consistent with the weak initiation hypothesis of Bluestein and Parks (1983). Brooks and Wilhelmson's simulated storm's weaker updraft produced less precipitation for an extended period of time, and hence was a simulated LP storm, despite using a liquid-only scheme with only warm rain microphysics processes (no ice).

b) Microphysical feedbacks influencing supercell downdraft dynamics and effects on low-level rotation and tornadogenesis in LP/CL/HP supercells

When simulating supercell thunderstorms, the microphysical parameterization has a large impact on the cold pool and can influence storm longevity (Gilmore et al. 2004a). Understanding microphysical impacts on the cold pool is also important due to virtual potential temperature and pseudo-equivalent potential temperature being dependent on temperature and moisture. It has been noted that warmer, typically moister supercell cold pools are associated with tornadoes (e.g., Markowski et al. 2002). Early supercell studies that focused on understanding storm dynamics used simplified microphysical schemes having only liquid hydrometeors (cloud water and rain water; e.g., Wilhelmson and Klemp 1978). However, the inclusion of ice results in significant differences in downdraft strength and, thus, storm dynamics, morphology, and propagation (Gilmore et al. 2004a; van den Heever 2004). Simulated storms with ice included in the microphysical parameterization have stronger downdrafts, resulting in cooler cold pools and more accumulated precipitation, as compared to storms simulated with a liquid only scheme (Gilmore et al. 2004a). The liquid-ice (3-ICE) scheme used in Gilmore et al. (2004a), produces stronger downdrafts from melting and sublimation of hail/graupel, which leads to production of more rain and more accumulated surface precipitation (Gilmore et al. 2004a).

The reason that the temperature of the downdraft may be important is because warmer downdrafts have been associated with more near-ground vorticity in both VORTEX-1 observations as well as axisymmetric numerical simulations (Markowski et al 2002). Hydrometeor-driven downdrafts affect the strength and depth of the cold pool, which in turn can influence the amount of baroclinic vorticity production along the gust front (e.g., Rotunno and Klemp 1985) as well as surface vorticity (and tornadogenesis) (Markowski 2002). Precipitation driven downdrafts can enhance horizontal vorticity at the surface, which becomes tilted vertically by the updraft, leading to strong 0-1 km rotation (Klemp and Rotunno 1983; Rotunno and Klemp 1985). Davies Jones (2009) showed that a hydrometeor-driven downdraft could also transport angular momentum about a vertical axis towards the surface where convergence occurs with the updraft, resulting in tornado formation, based upon the earlier Fujita Recycling Hypothesis (Fujita 1975). Surface vortices are stronger and last longer as the buoyancy of downdraft parcels increase (warmer downdrafts) in idealized axisymmetric tornado simulations (Markowski et al. 2003). There is a higher probability of simulated tornadogenesis in high low-level shear, moist boundary layer environments having lower lifted condensation levels (LCL) and small surface dew point depressions (Markowski et al. 2003; Thompson et al. 2003).

Thus, the near-storm environment may influence tornado potential through its influence on downdraft characteristics. The thermal and moisture profile, along with shear, and microphysical characteristics determine the downdraft intensity. Cooler/moister soundings will have less evaporative cooling and weaker downdrafts compared to warmer/drier soundings (Cohen and McCaul 2006). Warmer and drier soundings will promote more evaporative cooling through the column, leading to cooler, more negatively buoyant air. In addition, greater shear in the low-levels can weaken downdraft strength for the same thermodynamic profile from entrainment (Gilmore and Wicker 1998).

In summary, there are many factors that determine the mode of supercell convection (LP/CL/HP), with the microphysical and thermodynamic characteristics of the downdraft being an important factor. It has been found that more sophisticated microphysical parameterization schemes, adding of ice species, changes the downdraft dynamics (Gilmore et al. 2004a; van den Heever 2004).

c) Environmental impacts on microphysics and LP/CL/HP classification

Two primary studies have considered environmental differences between visually confirmed LP, CL, and HP storms by using 00 UTC "proximity soundings". These are RS98 and Bluestein and Parks (1983). Both required soundings to be close enough spatially and temporally to represent the environmental air mass where the storm developed and the sounding could not show contamination from neighboring storms[1]. Before reviewing their findings below, it should be noted that there are some differences between the respective studies. First, Bluestein and Parks (1983) considered only LP versus CL environments whereas RS98 considered all three environments (LP, CL, and HP). Furthermore, the soundings were modified in different ways. RS98 adjusted the surface sounding data in a few cases to be consistent with near-storm conditions whereas Bluestein and Parks (1983) removed superadiabatic layers in their soundings. RS98 used the virtual temperature correction noted in Doswell and Rasmussen (1994) when computing the representative surface-based parcel path whereas Bluestein and Parks

---

[1] Weisman et al. (1998) showed an existing storm can modify its local environment as far out as 30 km, suggesting that the "nearest possible" sounding, taken after a storm has already formed, may not always be the best choice. However, likely due to difficulty in knowing just how much the environment had been modified, previous studies have not addressed this.

(1983) did not. This should have resulted in larger CAPE, smaller CIN, and lower LFC heights in RS98 than in Bluestein and Parks (1983). These caveats stated, both obtained similar results regarding LP and CL storm environments differences, which will be reviewed below.

i) Thermodynamic profile and derived variables associated with LP/CL/HP

The environmental sounding-derived variables that were tested by RS98 for statistically significant differences across the supercell spectrum are: upper tropospheric storm relative wind velocity, Lifted Condensation Level (LCL), Level of Free Convection (LFC), Convective Available Potential Energy (CAPE), depth-weighted Mean Relative Humidity from 0 to 5 km AGL (0-5 km *RH%*), Precipitable Water (*PW*) integrated between the surface and 5 km, and extinction height. Since the variables are based upon surface parcels, hereafter the names will be SBCAPE, SBCIN, SBLCL, and SBLFC. These parcel-dependent variables were also calculated using the virtual temperature correction (Doswell and Rasmussen 1994), whereby environmental moisture is included in the integration of parcel buoyancy with height. Precipitable water in RS98 is defined by

$$PW = \frac{1}{\rho} \int_{0}^{5\,km} q\, \rho\, dz, \qquad (1)$$

where q is mixing ratio and ρ is air density.

RS98 found that HP supercell environments had highest mean *PW* (in), mean extinction height (km), and mean SBLFC height (km). The three previous mentioned variables have significantly different means compared with all other supercell classes mean for that particular mean at an 98% confidence level (Fig. 3). HP storms had the highest mean values of SBLFC heights and extinction heights, thus producing potentially colder low-level outflow given the larger implied precipitation amounts (larger *PW*).

LP supercell environments had the lowest mean 0-5 km *RH%*, though this value was not different in a statistically significant way from those from CL and HP environments. LP storms also had a statistically significant difference in lower mean SBCAPE at the 98% confidence level and a higher mean SBLFC height at the 95% confidence level compared to the other classes. Bluestein and Parks (1983) obtained similar results, with LP supercells having higher SBLCL heights relative to CL supercells. These higher SBLCL heights are consistent with less low-level moisture (found by Bluestein and Parks 1983). However, the moisture difference between LP and CL storm environments is not apparent when moisture is integrated through a deeper 0-5 km layer (i.e., *PW* computed in RS98). These differences and why they may be important to microphysics are discussed further in a later section.

From the RS98 study, CL storms had the lowest mean SBLCL and SBLFC heights (consistent with less evaporation potential in the boundary layer) and had the highest mean SBCAPE value. The mean CL SBCAPE was statistically significant difference at a 95% confidence level compared to LP/HP means. The 0-5 km mean *RH%* was similar across the three storm classifications.

ii) Vertical Wind Shear Profile

The Brooks et al. (1994) modeling study focused on the connection between the midlevel mesocyclone and low-level mesocyclone and how they are linked to the precipitation distribution in the storm. Brooks et al. (1994) found that with low-shear, simulated storms have mid-level rain falling closer to the updraft and the mesocyclone is able to wrap the precipitation around the west and southwest side of the updraft.

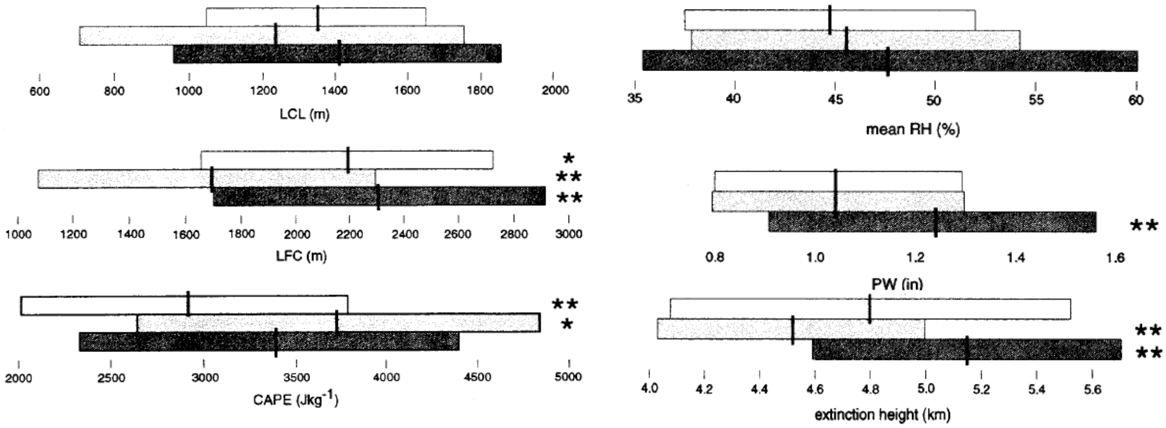

Fig. 3. Bar graphs of LCL height (m AGL), LFC height (m AGL), CAPE (J Kg^{-1}), Mean RH (%), and 0-5 km integrated Precipitable water (in). The white bar represents LP supercells, the gray (middle) bar represents CL supercells, and the black bar represents HP supercells. The black vertical tick mark represents the mean value, which extends +/- 1 standard deviation from the mean. A single star beside the bar indicates that the mean is statistically different than all other supercells at a 0.05 *p*-value, and a double star indicates that the mean is statistically different than all other supercells at the 0.02 *p*-value. From RS98.

Yet, the fact that the low-level (0-3 km) vertical wind shear helps to determine the midlevel mesocyclone strength suggests a close interplay between the low-level environmental winds that help to determine mesocyclone intensity and midlevel environmental winds that help determine how precipitation is advected around the updraft (Brooks et al. 1994). Similar to Brooks et al. (1994), RS98 hypothesized that the upper-tropospheric storm-relative winds play a crucial role in determining the number and size distribution of hydrometeors that will be circulated around the updraft for further growth and sedimentation, or advected downshear away from the storm, which they suggest would influence supercell class.

As part of their analysis, RS98 developed a composite hodograph for each class (LP/CL/HP). They did this by averaging the wind profiles for each class as a function of height using a technique developed by Brown (1993) and later followed by Rasmussen and Blanchard (1998) and Bunkers et al. (2000). For the composite wind profile, hodographs were first translated and rotated into a common framework (RS98), a process that will be explained further in the methodology section (section II herein). The resulting hodograph composites showed some evidence that the upper tropospheric storm-relative winds may be a distinguishing factor between classes in that the LP and CL composites show backing and stronger upper-level winds whereas the HP composite shows veering and weaker upper-level winds (Fig. 4b). They hypothesized that the stronger 9-12 km storm-relative winds in the LP cases transport small hydrometeors downwind and away from the central updraft, limiting their re-ingestion into the storm updraft and thereby reducing the number of hydrometeors that may grow into precipitation-sized particles. The CL cases showed slightly weaker 9-12 km storm-relative winds than the LP cases (Fig. 4b) and they therefore hypothesized this would result in having the hydrometeor distribution closer to the central updraft region. The HP cases had the weakest 9-12 km storm-relative winds of the three classifications (Fig. 4b), presumably allowing for greater amounts of hydrometeors to be re-ingested into the updraft and more growth before falling to the surface. RS98 also noted the tendency for the HP cases to deviate more in their motion – likely due to stronger cold pool production. The Bunkers et al. (2000) composite/mean proximity hodograph of 35 supercells with highly deviant storm motion is similar to the RS98 HP composite, with veering winds above 6 km and weaker upper-level storm-relative winds (Fig. 4a). [Both studies used a similar averaging procedure. However, the Bunkers et al. (2000) highly deviate storm motion composite had more low-level curvature than did any of the RS98 composites.] Likewise, the non-deviant, Bunkers et al. (2000) supercells (225 cases) showed backing upper-level winds similar to RS98 LP and CL composites (Fig. 4a). In contrast, RS98 reported that in their study LP storms propagated slower and further to the right, enhancing upper tropospheric storm-relative winds compared to the other storms, while HP storms propagated more randomly with a few propagating along the boundary layer to 4 km shear vector, which hindered upper tropospheric storm-relative winds. Thus, highly deviant composite LP storm hodographs from RS98 may ***not*** be comparable to the highly deviant composite hodographs by Bunkers et al. (2000) due to these inconsistencies in how the soundings were collected and composited.

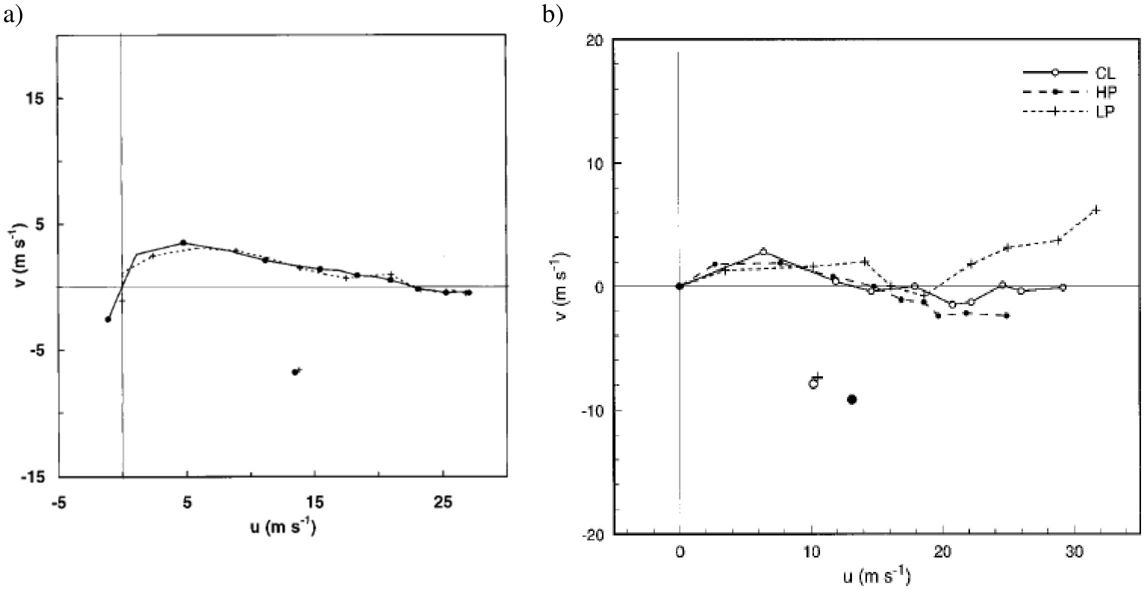

Fig. 4. Height average of LP/HP/CL soundings from a) 95 typical (solid) vs. 35 atypical (dash) composite 0-8 km hodographs from Bunkers et al. 2000 (1 km increment markers) and b) from RS98. Figures have been resized to match in scale. Symbols correspond to storm type indicating storm motion.

d) Hail association with and possible importance to determining LP/CL/HP classification

Not much is known about the occurrence of hail across the supercell spectrum and whether certain classes are associated with smaller or larger hail sizes. There is anecdotal evidence that LP storms can produce giant hailstones while lacking visually opaque smaller raindrops (Straka and Gilmore 2006). Previous studies that artificially changed the hail size distribution (e.g., Gilmore et al. 2004; van den Heever and Cotton 2004) did not address the role of the environment in naturally changing supercell precipitation distributions.

What is known, however, from artificially changing the hail size and distribution within simulated supercell storms and simpler ice microphysics schemes is that these changes affect hailstone terminal velocities and rates of cooling within the storm and at the surface (e.g., van den Heever and Cotton 2004). For instance, van den Heever and Cotton (2004) found that smaller hail diameters with slower-falling hail induce more melting and shedding, stronger downdrafts, and faster propagating cold pools. As mentioned earlier, stronger outflow is generally associated with greater deviant motion that is more likely with HP supercells (RS98; Bunkers 2000). In some cases, for weaker vertical wind shear, a supercell updraft may meet an early demise if the cold pool is too strong (Gilmore et al. 2004; Gilmore and Wicker 1998).

Even though not much is known about the differences in hailstone growth and behavior between actual LP/CL/HP supercells, understanding a typical supercell hailstone growth trajectory is of interest. Previous studies of hail formation indicate that hailstone embryos are transported vertically by the updraft past the freezing point, fall back towards the surface, and then are re-ingested into the updraft and grow until the hailstones reach terminal fall velocities that the updraft can no longer suspend. This is shown in Fig. 5, taken from Browning and Foote (1976).

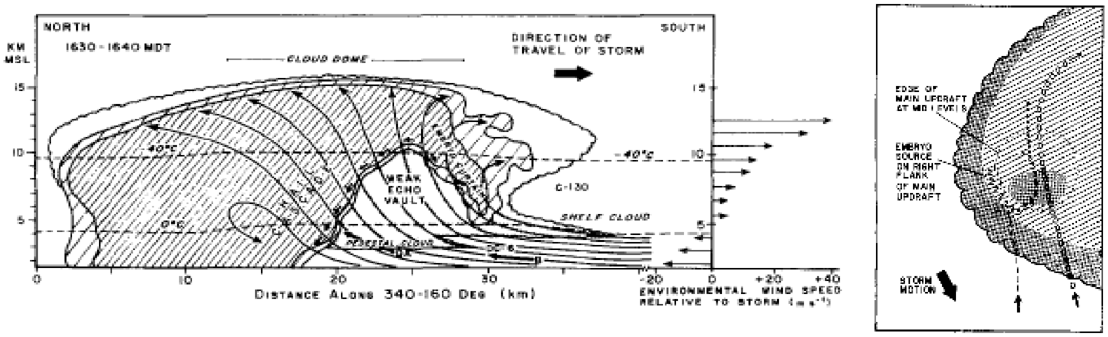

Fig. 5. Favorable and unfavorable growth trajectories along with associated features of the visual cloud boundaries and radar reflectivity (shading), from the perspective of a) vertical cross section, also showing the 0°C and –40°C isotherms where hail growth occurs; and, b) horizontal plan view (Reprinted from Browning and Foote 1976).

Browning and Foote (1976; hereafter BF76) proposed a three-stage hail growth model, based upon calibrated radar and multiple aircraft observations, and showed that the trajectory of a hailstone embryo plays a critical role in hail growth. They found that the wet and dry growth layers within hailstones can be explained by the hailstone experiencing a single up and down trajectory – contrary to the earlier theory that required multiple recycling excursions (e.g., Humphries 1964) [2].

BF76 found that an unfavorable trajectory is through the central updraft, where lightweight hail embryos quickly rise in the updraft and are ejected into the anvil (Fig. 5). Instead, the ideal region for hail development and initial hail embryo trajectory is in the rear midlevels of the storm along the edge of the updraft, upshear of the central updraft

---

[2] Not all hailstone embryos follow such a path. Shed drops or ice fragments likely rise within the updraft and form hailstones without following such a trajectory (Koenig 1964; Dye and Hobbs 1968).

core (Fig. 5). This is in a region of weak updrafts, providing the lightweight hail embryos, a longer residence time whereby they can grow larger through accretion of supercooled liquid water droplets [3]. The result is small hail with faster terminal fallspeeds, which can therefore spend more time in the main updraft near adiabatic liquid water contents during the final stages of the hail trajectory, eventually exiting the updraft once the hailstone terminal fallspeeds exceed the updraft speed. Miller et al. (1990) found that for a Montana hailstorm, small hail (10-20 mm) followed a trajectory in the storm that placed the particles in more dry growth region above 11 km. Large hail (40-50 mm) took a more favorable path in the storm with higher amounts of cloud water and supercooled droplets resulting in spongy growth within the central core of the mesocyclone during this final stage.

In support of BF76, Tessendorf et al. (2005) is among several recent studies that have provided evidence by using trajectories to disregard the recycling theory. The criteria for a supercelluar storm to produce large hail is small embryonic sized particles (near-millimeter to millimeter) must be present. There must be a mechanism, such as inflow along the right flank of the storm, to transport these particles into the updraft. The updraft must have sufficient strength and size (diameter of the updraft) to grow in these regions of favorable growth. The mesocyclone strength is a result of the shear in particles into hail sizes, and the horizontal winds must keep the growing particles within the low to midlevel winds, which is the most favorable region for maximum growth. If these criteria are not met, then the particles will not grow to the size of hailstones, thus

---

[3] A significant percentage of hailstone embryos can be from frozen raindrops (Koenig 1963, 1965).

being transported through the updraft to the anvil level of the storm (BF76, Tessendorf et al. 2005).

e) Summary and experimental hypotheses

In summary, this review of past research suggests that whether a supercell is LP/CL/HP may be a function of both the near storm environment and the internal storm microphysics. Anecdotal evidence suggests that both LP and HP supercells can produce giant hail, but LP storms seem to be missing the opaque raindrops and may produce fewer hailstones (Bluestein and Woodall 1990). HP storms should produce more evaporative cooling near the ground due to their greater total precipitation content, which may result in greater deviant motion, but RS98 found that the LP storms actually had the most deviate motion. When considering deviant storms as a separate class, Bunkers et al. (2000) found that those soundings were more like the HP composites from RS98 than the LP composites. Thus, there are inconsistencies from previous studies that may be resolved through numerical modeling.

One way of validating that composites are representative of the respective LP, CL, or HP storm environments is to check which ones are able to reproduce the precipitation behavior in a model. Of particular interest are the growth trajectories that influence low-level rain/hail sedimentation (how LP/CL/HP is classified by radar), influence the low-level cold pool, and influence low-level rotation and tornado potential.

Scientific hypotheses or research questions related to the research herein include:

1) The feature average composite will lead to preserving higher amounts of moisture, particularly in the boundary layer, compared to the height average composite.

This will lead to the feature average composite always outperforming the height average composite when preserving parcel based calculations such as CAPE and CIN, which are highly dependent on near surface moisture and temperature.

2) The feature average composite sounding technique will support simulated LP/CL/HP supercells that represent their appropriate precipitation characteristics (both amount and location with respect to the updraft) because features important to their development will be better preserved (compared to height average technique). This will be tested with Beatty et al. (2009) plots. An associated hypothesis is that simple ice and liquid microphysics is sufficient as long as the sounding is well represented.

3) The use of feature average soundings in Cloud Model 1 (hereafter, CM1) will produce longer duration storms compared to the use of height average soundings in CM1 due to the increased CIN values (decreased boundary layer moisture) present in the height average soundings.

4) Because the Bunkers et al. (2000) predicted storm motion suggests greater rightward propagation for HP storms relative to RS98, this is what is expected for the simulated storms.

CHAPTER II

METHODOLOGY

As mentioned above, the goal of this research is to understand how precipitation develops within supercells and how that affects supercell type (LP/CL/HP). To do this, an accurate depiction of the separate environments associated with actual LP/CL/HP supercells is required. In addition, a sophisticated microphysics scheme might be required to capture a realistic evolution of precipitation (especially hailstones and rain) inside the supercell. A simple microphysical parameterization scheme would be single moment Kessler liquid-only or single moment Lin, Farley and Orville (3-ICE) scheme. A sophisticated microphysics will have multiple ice species and usually more than one moment predicated, usually mixing ratio (q_v) and/or total number concentration (N_t). (The purpose of this section is to describe: 1) how environmental conditions associated with LP/CL/HP supercells will be determined, 2) the model and microphysics scheme that are used, and 3) the analysis techniques used to investigate precipitation development.

a) Sounding selection and preparation

The RS98 study provided 43 supercell storms that were visually classified as LP, CL, or HP and that were paired with the nearest representative environmental sounding location, that data set is used herein. Following Bluestein and Parks (1983), RS98's soundings had to be located in the same environmental air mass as the supercell storm and could not have been affected by a frontal passage, cold outflow from neighboring storm, or effects from precipitation cooling the air. RS98 then modified these soundings using surface data that were closer to the observed storm. Because RS98 did not provide the sounding locations and because details regarding storm locations were missing in 25% of cases, a reanalysis of the nearest sounding location was performed herein following RS98 except that near-storm surface observations were not used to modify the soundings. Sounding data were retrieved from the Plymouth State University's archive database. Using reanalysis (synoptic) maps, skew-T diagrams, and Google maps, a subset of 29 of the locations from RS98 and Beatty et al. (2009) were identified: 10 CL, 10 LP, and 9 HP sounding locations. Fourteen storm locations from RS98 could not be unambiguously identified. Perhaps future studies could include multiple sounding locations that seem reasonable into the averaging process. The raw sounding data (of pressure, temperature, relative humidity, wind speed, and direction) were obtained from Plymouth State, and are in FSL sounding format. This format was used because it is the input format used in the skew-T log-p plotting program used herein. That same program saves a model input sounding that contains height, potential temperature θ, water-vapor mixing ratio q_v, the east-west component of the wind u, and the north-south component of the wind v.

The moisture variable chosen for averaging during the compositing process should affect the resulting soundings and this sensitivity is also tested herein, as it has not previously been tested in the literature. The moisture variables considered are dew point temperature T_d, relative humidity RH, water vapor mixing ratio q_v, vapor pressure e, and wet-bulb potential temperature θ_w. Moisture differences associated with the use of different variables in the compositing process could lead to parcel-dependent differences if the virtual temperature correction is applied.

Prior to compositing, the hodographs from each sounding are rotated and translated following Brown (1993), RS98, Rasmussen and Blanchard (1998), and Bunkers et al. (2000). A hodograph is a plot connecting the tip of each wind vector between adjacent height levels and the local magnitude of the vertical wind shear vector is proportional to the length of the hodograph between each level. Hodographs can be safely rotated because the mode of developing convection has been shown to only depend upon the magnitude and direction of shear as it changes with height (Klemp and Wilhelmson 1978b; Rotunno and Klemp, 1982) –in other words, the environments are Galilean invariant.

The exact procedure described here follows RS98 and is illustrated in Fig. 6. The 0-500 m average boundary layer (BL) wind speed vector was calculated first, with the whole hodograph then translated such that the tip of the average BL wind vector would be at the origin of the hodograph. The next step was to use the mean 500 m winds along with the wind at 4 km AGL to calculate the 500 m to 4 km shear vector. The hodograph was then rotated such that the mean 500 m to 4 km shear vector was parallel to the x-axis. This resulted in a new hodograph with u' and v', which are rotated/translated winds relative to the original u and v. The rotated/translated hodographs in each class could then be averaged.

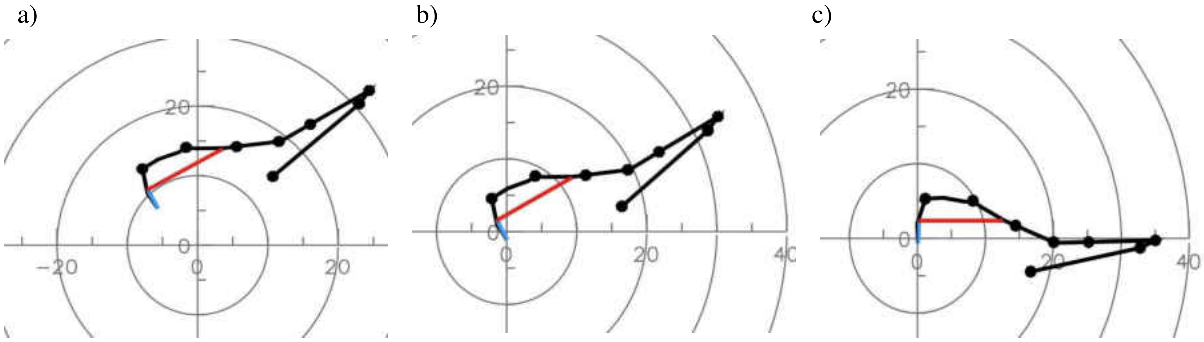

Fig. 6 An example hodograph showing the steps in the translation and rotation process: a) original hodograph, b) after translation, and c) after rotation. The lowest 500 m average BL wind vector is in blue and the shear vector between 500 m and 4 km is in red.

RS98 noted that, at times, sounding surface data were replaced with more representative surface data closer to the storm's inflow (as long as it was not being affected by cold storm outflow and was within the same air mass as the supercell). RS98 did not report the values or cases where surface temperatures, dew points, and boundary layer winds were adjusted and, thus, this process could not be replicated herein.

Storm motions for each sounding were estimated using the Internal Dynamics (ID) method (Bunkers et al. 2000). Accurately estimating storm motion is important for computing hodograph-derived storm-relative sounding variables such as storm-relative wind and storm-relative helicity. Predicted storm motions are also useful for estimating morphology, storm track, and longevity (Bunkers et al. 2006). More discussion regarding supercell storm motion estimation is provided in Appendix A.

b) Development of a sounding composite for each class

Previous investigators have characterized *mean* near-storm environments using two methods, and both are used herein. The most popular approach is the height averaging technique where each sounding variable is averaged at each altitude above ground for a group of soundings. This approach has been used in many proximity-sounding studies since the 1950s (Fawbush and Miller 1952, 1954; Beebe 1955). The other, less-well-known, less understood, and less tested method is the feature averaging technique where the common features of each variable (θ, moisture, and wind) and their corresponding heights are averaged separately (Brown 1993). Neither technique provides guidance as to which moisture variable is most appropriate for averaging (q_v, T_d, RH, e, wetbulb-potential temperature), so several versions of each are calculated herein. Darkow (1969) studied tornadic proximity soundings to estimate average environmental soundings for Central Plains, Gulf Coast, and High Plains storms. The Darkow (1969) methodology included pairing the proximity sounding with a "check" sounding collected at the same time as the proximity sounding. The check sounding was obtained from the closest upper air station that was in the upstream direction of the mean low level moisture flow. There were significant differences in the T_d profiles, with values being higher in the average proximity sounding as compared to the average check sounding. Darkow (1969) concluded that the differences between the proximity and check soundings are most recognizable when comparing the equivalent potential temperature, wet-bulb potential temperature, and static energy. Lucas and Zipser (2000) noted that specific humidity (mixing ratio) could be reduced to unrealistically low boundary layer values during averaging of numerous tropical soundings.

For the winds, either feature or height averaging requires an initial preparation of the hodograph by rotating and translating prior to averaging (as discussed in the previous section). Also, in the feature-averaging technique, no guidance is provided as to how many soundings in a group need to have a particular feature before it is preserved as an average feature.

As an alternative to creating composite/mean soundings for each class, other researchers have simply kept the soundings separate and just computed common sounding-derived variables and associated those with various types of severe weather (e.g., Thompson et al. 2003). As an alternative to compositing, some scientists have performed simulations using all of the soundings in each class and then analyzed each group statistically in terms of model output (e.g., Cronce et al. 2006). Finally, some scientists have used k-means cluster analysis to group common soundings prior to averaging (Lucas and Zipser 2000).

i) Height averaging technique

The following variables are averaged at each height above ground level (AGL): temperature T (C), dew point temperature T_d (C), u wind speed, and v wind speed. To illustrate the height averaging technique, the following figures will display two soundings with slight differences in CAPE, CIN, and capping inversion heights. Because each sounding has data at slightly different elevations, all soundings were linearly interpolated to a common grid having a vertical spacing of 100 m before averaging.

Previous studies (Fawbush and Miller 1952, Beebe 1955, Darkow 1969, Brown 1993) have noted the importance of the amount of moisture in the boundary layer and the temperature inversion that occurs most frequently between 900 – 800 mb. Brown (1993) was the first to attempt to preserve these features, based off of proximity soundings, for one average or composite sounding that represents a storm's environment. Brown (1993) noted that the temperature inversion, in particular, would be smoothed with traditional height averaging.

ii) Feature averaging technique

To avoid smoothing thermodynamic and wind features between *n* soundings, feature averaging can be performed (Brown 1993) whereby both the variable of interest and the height, z, are separately averaged to produce a single composite sounding. This averaging technique results in capturing features that are consistent with each sounding and eliminating features that are not consistent. An example comparing the two different compositing techniques for two soundings is shown in Fig. 7. It has previously been cited in only seven scientific papers (Blanchard 2011, Market el al. 2006, Ramsay and Doswell III 2005, James et al. 2005, Davies-Jones 2003, Bunkers 2002, and Bluestein and Banacos 2002) and it was used in only three of these. James et al. (2005) used the Brown (1993) methodology to preserve boundary layer features of squall line environments - separately averaging T, T_d, and height above ground. The feature found to be most consistent between the soundings in both James et al. (2005) and Market et al. (2006) was the elevated mixed-layer above the surface, and incidentally this is one of the features preserved in the study herein.

The five other papers mention the utility of the Brown (1993) method but do not use it: Blanchard (2011), Ramsay and Doswell (2005), Davies-Jones (2003), Bunkers (2002), and Bluestein and Banacos (2002). Blanchard's only reference to Brown (1993) was in the introduction where it was stated that a clockwise-rotating hodograph is indicative of severe weather (Bunkers et al. 2000; Brown 1993; Maddox 1976). Ramsay and Doswell (2005) included 26 hodographs from Brown (1993) in their dataset but did not utilize the feature averaging technique. Bunkers (2002) deemed the approach to be too complex for his large dataset.

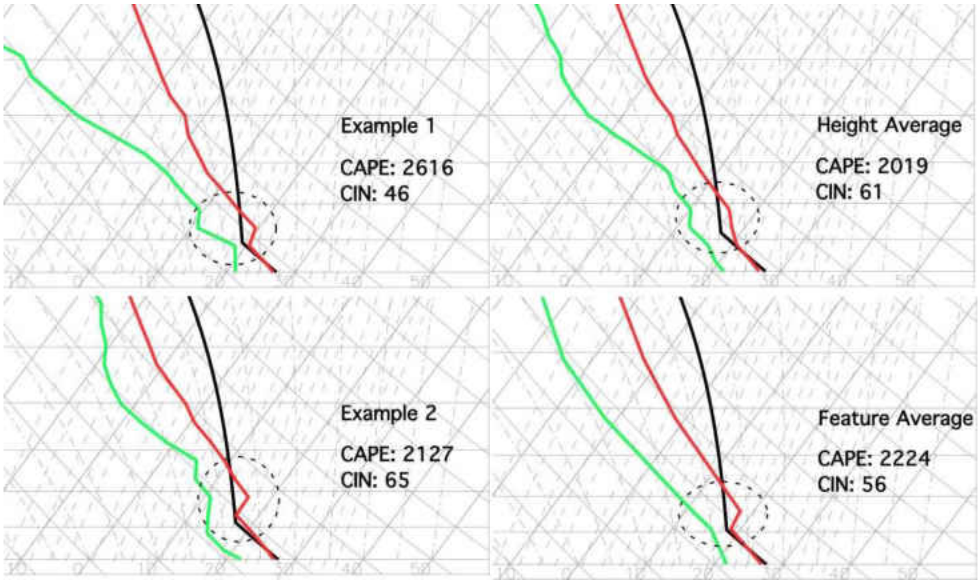

Fig. 7. (Left) Two Idealized soundings showing the capping inversion located at different heights. (Right) The height averaging technique smooth's the capping inversions (top); the feature averaging technique retains a capping inversion (bottom). A lowest-100 mb average parcel was used to compute the CAPE and CIN values shown.

"Features" herein may be a single point, two points describing a linear change with height, or series of points approximating a curved feature (nonlinear) in thermodynamic or kinematic fields. Herein, each point of a feature was separately averaged (but an alternative to this is described in Appendix C). For instance, at a single point location "*a*", one would first average all of the θ values and then all of the z values using

$$\bar{\theta}_a = \frac{\Sigma(\theta_{1a}+\theta_{2a}+\cdots+d\theta_{na})}{n_a}, \tag{2}$$

and

$$\bar{z}_a = \frac{\Sigma(z_{1a}+z_{2a}+\cdots+z_{na})}{n_a} \tag{3}$$

One would use the same approach when averaging moisture and wind values (not shown).

Although no previous investigators recommended a threshold, herein at least 80% of the soundings had to have a particular feature to be included in a feature average sounding. The heights of each of the points comprising a feature were separately averaged following Brown (1993) using (3). One nuance not discussed in Brown (1993) is which moisture variable should be averaged: T_d, RH, q_v, e or θ_w. Tests using different moisture variables are discussed below in section (*II.b.vi.*).

Another nuance is whether the moisture variable should also be averaged if there is only a temperature feature or vice versa. (The alternative is to linearly interpolate the other variable.) Herein, regardless of whether the sounding had a feature in temperature or moisture, both temperature and moisture parameters were always included in the average at height (z). Then θ, moisture, and height were separately averaged for each point. The winds were not taken from a specific level if there was only a thermodynamic feature and not a wind feature in the hodograph at that particular level.

The features that were common among all classes (found in more than 80% of soundings in each class) are as follows and are shown in Fig. 8. The first feature is at the surface in all soundings where potential temperature, dew point, wind, and pressure are all averaged separately for each sounding group. These surface averages are identical between the height average and feature average sounding approaches. The second feature is comprised of two points (linear) and is nearly dry-adiabatic in temperature from the surface (already computed) to approximately the bottom of the capping inversion, which is the same as the top of the boundary layer (BL). One only need compute the averages at the top of the BL due to the linear feature being defined by a previously computed point the surface. The third (linear) feature is where the temperature lapse rate becomes isothermal, near isothermal, or increases with height (i.e., the “capping inversion”) and is bounded by the top of the BL and top of the inversion. A few soundings did not have this capping layer feature and were excluded from the average. The fourth feature (linear) that is preserved is the elevated mixed layer- EML, which is bounded by the top of the inversion and wherever the EML departs from dry adiabatic – usually several hundred meters above the inversion top. Continuing up the thermodynamic profile, the fifth feature is the location of minimum temperature (a single point). The sixth feature (non-linear) is found between the minimum location and the tropopause. All of these features are shown in Fig. 8.

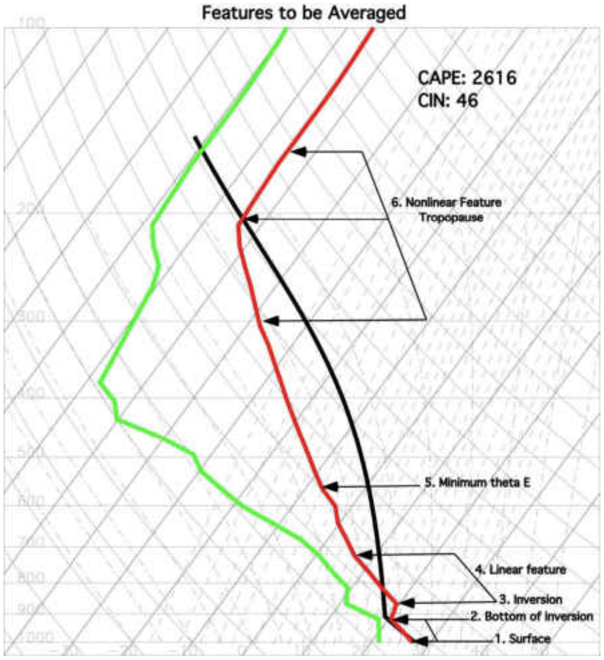

Fig. 8 Thermodynamic features common to the soundings in this study.

Feature averaging for the winds presented some problems due to the complexity of each individual sounding. However, in summary, the following features were averaged for *u*', *v*', and height: surface, nonlinear curving hodograph in the lowest 1 km, maximum *v*' in the 1-2 km level above ground, the minimum wind shear level, and the wind maximum (jet stream) level. The first feature was the surface winds in the *u*' and *v*' components. The second feature (nonlinear) was defined using the first sounding point above the surface as the lower bound and the first point above the 1 km height as the upper bound with a single midpoint between those points. It is important to capture the low-level winds because of their significance in determining the 0-1 km helicity, which is known to be an important parameter that is helpful in forecasting supercell tornado intensity (e.g., Thompson et al. 2003). The third feature was the maximum *v*' in the 1-2 km layer above ground level, as proposed by Brown (1993). The fourth feature was the minimum shear layer. The fifth feature (linear) was the maximum (jet level height) wind as proposed by RS98 – thought to be critical for storm relative flow that influences supercell precipitation characteristics (LP/CL/HP). It was the only feature specifically chosen by height because RS98 noticed it in their height average hodographs (Fig. 9.)

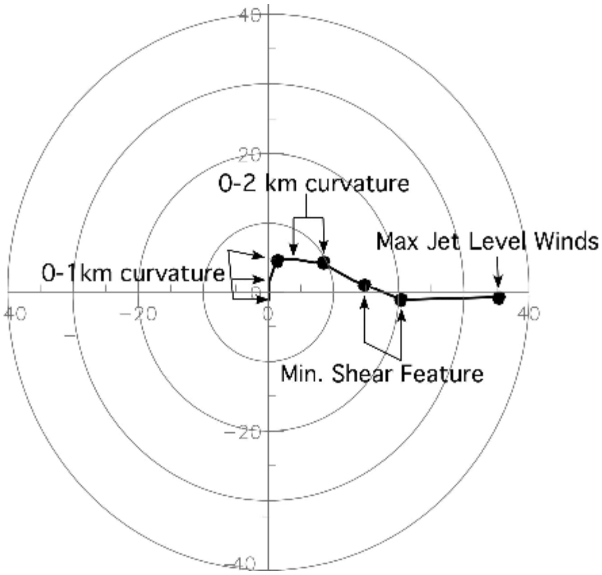

Fig. 9 Common features to be averaged between hodographs to create feature average composite hodographs.

The next step in the feature averaging process is to combine the feature average thermodynamic profile with the feature average *u*' and *v*' rotated and translated winds. This is necessary since most models require all state and kinematic variables to be defined at each level in the vertical. There are two ways to combine the these: 1) feature average all sounding variables, based upon a feature present in only one variable, regardless of whether features were present in other variables, or 2) interpolate the feature average wind profile to the feature average thermodynamic profile and vice versa. Brown (1993) did not clearly state which version should be used, but instead treated the averaging as two separate entities. It is argued herein that the second method is more appropriate to avoid introducing false features. For instance, if one has a thermodynamic feature at 2500 m AGL, but with no wind feature, then the wind should be interpolated from the feature average wind profile to avoid introducing a false wind feature. The same can be said for thermodynamic variables: they should be interpolated to the altitude of a wind feature.

iii) Final sounding preparation before use in a Cloud Model

Environmental soundings have realistic features such as superadiabatic layers near the ground that are not favorable in CM1. Thus, individual and composite soundings can have absolutely unstable layers in which the gradient Richardson number (*Ri*) is less than 0.25 (e.g., Kundu 1990). These will cause immediate overturning in the model, thereby changing the sounding and causing spurious clouds to form throughout the domain. To eliminate this problem, one final modification to the soundings was necessary prior to simulation in the model. The thermodynamic profile in each $Ri \leq 0.25$

layer was automatically modified such that $Ri = 0.251$ (refer to appendix B). This is about the minimum change necessary to avoid spontaneous overturning. This resulted in superadiabatic lapse rates to be decreased to 9.75° km^{-1}. The algorithm is described in Appendix B. Because of the perceived importance of winds and wind shear profiles in this study, winds were not decreased to increase the *Ri*.

iv) Sounding variables computed

One must choose a representative parcel when computing sounding variables. Many previous modeling studies advocate using a lowest-100-mb mixed-layer parcel. This was used in addition to RS98's surface-based parcel for comparison purposes. The Storm Prediction Center (NOAA 2006) uses both mixed-layer and surface-based parcels when determining parameters like CAPE, CIN, LCL, and LFC. Herein, results for both types of parcels will be shown.

For each of the composite soundings and original soundings, the following parameters are computed: MLCAPE, MLCIN, MLLCL, MLLFC, SBCAPE, SBCIN, SBLCL, SBLFC, *PW*, and *RH* between certain layers, based upon RS98. One parameter that was previously found to be significant is precipitable water (*PW*) content that was calculated from the surface to 5 km using (1). HP supercell environments do not necessarily have more *RH* as compared to CL and LP supercell environments, but HP supercells have, on average, a statistically significant increase in PW in their environments (RS98).

c) Moisture variable to be averaged

There are different motivations for using different moisture variables (RH, T_d, e, q_v, or θ_w) when averaging, and it will be shown that each gives slightly different answers for the height and feature average soundings. The temperature in Celsius was converted to potential temperature, which was paired with the different moisture parameters. This cause differences in parcel-dependent parameters such as CAPE, CIN, PW, and 0-5 RH, which will, in turn, cause differences in storm updraft buoyancy in the simulated storms. Strengths and weakness of using each of these moisture variables are presented below.

Relative humidity (RH) might be chosen because it is directly measured in the sounding data. RH relates the amount of water vapor pressure to the saturation water vapor pressure. Since evaporation and sublimation rates are inversely proportional to RH (e.g., Bohren 1987), and those rates influence the cold pool temperature (e.g., Gilmore et al. 2004a), cold pools might be better represented between classes if RH is averaged. On the other hand, the relative humidity may not be the best measure of moisture content since it is dependent on both T and moisture content. Even if the moisture content stays unchanged, the relative humidity value will lower if T is increased.

The dew point temperature T_d is a direct measure of the amount of water vapor in the air. It indicates the temperature where saturation will occur if an air parcel is cooled isobarically. If T_d is high, then the water vapor content is high, and vice versa. The difference between temperature T and dew point temperature T_d is inversely proportional to RH: the closer the spread (a.k.a. dew point depression) the higher the relative humidity. The dew point depression at the surface is related to the LCL height and both are valuable forecasting parameters for tornadogenesis (Rasmussen and Blanchard 1998). T_d is not conserved during adiabatic vertical motion. Moving an unsaturated air parcel adiabatically upward by 1 km will reduce its T_d by about 2 °C. Since averages between T_d values occur at different altitudes there may be an unintended bias in the resulting average T_d. That said several previous studies have apparently averaged T_d when creating feature average soundings (Market et al. 2006). Furthermore, when using height averaging, since the AGL height is used, some studies have consequentially averaged T_d at different pressure altitudes.

Vapor pressure, e, for a given volume of air is dependent on temperature and density of water vapor molecules. Water vapor makes up a very small percentage of the total atmospheric mass. Vapor pressure is thus defined as the pressure exerted by the molecules of a given vapor (AMS, Glossary). Since e is dependent on temperature this will have implications determining how much moisture is present, meaning if temperature rises and moisture stays constant e will decrease even though the moisture has stayed constant.

The water vapor mixing ratio q_v, which is very closely related to specific humidity, is defined as the mass of water vapor per mass of dry air. The units are commonly denoted as number of grams of water vapor per kilogram of dry air. The advantage of using q_v is that it does not change as air adiabatically expands or contracts during vertical motion, and it is not dependent upon T[4]. For example, if a kilogram of air contains one gram of water vapor, it will still contain one gram of water vapor after the kilogram of air is heated. One might argue that mixing ratio or specific humidity is most appropriate moisture variable to average between different sounding locations/levels

---

[4] If net condensation or evaporation occurs q_v will change (Tsonis 2007).

having different temperatures. It is also the input moisture variable into CM1 and the Weather Research and Forecasting Model (WRF).

The wet-bulb potential temperature (θ_w) is an important moisture variable, particularly for severe convection. A parcel's θ_w determines its pseudoadiabatic path that it will follow during ascent. Thus, perhaps it would best represent the average updraft adiabat, and associated parcel-derived variables, that would represent all soundings within a class. However, it is slightly more complicated to compute. Once the average θ_w is computed, it must be paired with the average T to retrieve the associated T_d for plotting purposes.

i) The feature average moisture parameters

The first step after obtaining soundings from the Plymouth State server was to convert to the moisture parameter of interest from the dew point temperature. For instance, *water vapor* mixing ratio, q_v, is computed using Teten's formula:

$$q_v = \left(\frac{380}{p}\right) exp\left[\frac{(17.27 * Td - 273.15)}{(Td - 36)}\right], \tag{5}$$

where p is air pressure (Pa), and T_d is dew point temperature (Kelvin). The following relations (from Magnus 1844 using Bolton 1981 coefficients) are used to calculate vapor pressure and saturation vapor pressure, respectively:

$$e(T_d) = 6.112 exp\left(\frac{17.67 * T_d}{T_d + 243.5}\right), \tag{6}$$

and,

$$e_s(T) = 6.112 exp\left(\frac{17.67 * T}{T + 243.5}\right). \tag{7}$$

As the Plymouth State soundings provide T and T_d, relative humidity for each sounding level or feature can be obtained using

$$RH = \left(\frac{e(T_d)}{e_s(T)}\right) * 100. \tag{8}$$

θ_w was computed using the iterative equation from Rogers and Yau (1989),

$$\theta_w = \frac{-B}{\ln\left[\frac{p}{\varepsilon A}\left\{\left(\frac{c_p}{L}\right)[\theta - \theta_w] + qv\right\}\right]}, \tag{9}$$

where B = 5.42 x 10^3 K, p (Pa), A= 2.53 x 10^8 kPa, the specific heat at constant pressure c_p = 1004 J kg^{-1} K^{-1}, the latent heat of vaporization L = 2.5 x 10^6 J kg^{-1}, p is 10^5 Pa, and q_v is first calculated using (5).

Once each moisture parameter is calculated for each level and/or feature, the generic arithmetic mean formula is used to compute required quantities with either the height or feature average technique for "n" number of soundings and is given by

$$\bar{X} = \frac{X_1 + X_2 + \cdots + X_n}{n}, \tag{10}$$

where $\bar{X}$ denotes the moisture parameter to be averaged. The five different moisture variables described above that are independently averaged are: q_v, T_d, e, RH, and θ_w.

The final step after computing averages is converting all of the averaged moisture parameters from each average sounding back to q_v for simulation and plotting purposes. This is computed from $\overline{T_d}$ using (5), while q_v is computed from $\bar{e}$ using

$$q_v = \left(\frac{1000 * .622 * \bar{e}}{\bar{p} - \bar{e}}\right), \tag{11}$$

where $\bar{p}$ is the logarithmically-averaged pressure for that altitude (height average) or logarithmically-interpolated pressure (interpolated to the average height of the feature in the case of feature average sounding). This logarithmic approach was done because pressure does not decrease linearly. At each height where the feature was found the natural log of the pressure at that level was taken. Then the average was calculated from the natural log of the pressures. The exponential function was used to achieve a new average pressure. Values of q_v are also computed from $\overline{RH}$ and average saturation vapor pressure, $\overline{e_s(T)}$, by inserting values of $e_s(T)$ into Eq. 7, then average using Eq. 10 for that altitude or feature, and inserting the result into

$$\bar{e}(\overline{RH}, \overline{e_s}) = \frac{(\overline{RH} * \overline{e_s(T)})}{100}, \tag{12}$$

which is then inserted into (11). Values of q_v are computed from $\bar{\theta}_w$ using an inverted version of (9):

$$q_v = \frac{\varepsilon\, A}{p} exp\left[\frac{-B}{\overline{\theta_w}}\right] - \left(\frac{c_p}{L}\right)[\bar{\theta} - \overline{\theta_w}] \qquad (13).$$

The sounding can then be plotted and the data are ready for simulation in CM1.

d) Model & experimental design

The Cloud Model 1 (CM1), developed by George H. Bryan from the National Center for Atmospheric Research (NCAR) (Bryan and Fritsch 2002), is used to simulate idealized supercells using height and featured averaged soundings and hodographs for the average LP, CL, and HP of the supercell spectrum. The CM1 model is a non-hydrostatic, non-linear, three-dimensional, time dependent numerical model that is used to study idealized atmospheric phenomena. The model domain used herein is a 120 x 120 x 20 km grid with 1 km horizontal grid spacing and 250 m vertical grid spacing for initial test runs. Simulations that produced rapidly weakening storms were re-run at finer resolution. The grid spacing for the final production runs is 250 m in the horizontal. Data are output for 2 hours every 5 minutes. The updraft nudging, hereafter w-forcing, convective initiation method (e.g., Naylor et al. 2012) is on for the first 15 minutes of the model run. W-forcing is used so that sustained convection can develop within these more realistic soundings with inversions and convective inhibition. W-forcing is an updraft nudging approach for convective initiation in CM1. This updraft nudging approach uses the same dimensions as the thermal perturbation (warm bubble approach) that was introduced by Klemp and Wilhelmson (1978). Instead of thermal perturbation, vertical velocity of 10 m s^{-1} starts at t = 0 and last set time determined by user (Naylor et al. 2012). The microphysical parameterization scheme used in the initial runs is the Gilmore et al. (2004) 3-ICE single-moment bulk-mixing ratio scheme for each precipitating class. The lateral boundaries of the model domain are open. The model has 80 vertical layers with a grid spacing of 250 km. A Rayleigh damper is applied above 16 km to damp spurious gravity waves in the stratosphere.

i) Analysis methods

Statistical analysis

The sounding classifications were broken into three groups: LP/HP/CL. The sounding parameters mentioned above (CAPE, CIN, etc.) were checked for normality by using the Anderson-Darling Test:

$$A^2 = -n - S \qquad (10),$$

$$S = \sum_{k=1}^{n} \frac{2k-1}{n} \left[\ln\big(F(Y_k)\big) + \ln\left(1 - (Y_{n+1-k})\right) \right] \qquad (11).$$

For the Anderson-Darling Test to be computed the data must be arranged in ascending order represented by $F(Y_k)$. The computed *p*-value had to exceed 0.05 in order for the distribution to be considered a normal distribution. If the distribution was not normal, the Box-Cox transformation was performed on the distribution. The lambda values used to normalize the distribution were from .1 to 1.5 (Cronce 2006). A lambda value of 0.1 was used to normalize the HP 4-10 km shear magnitude and a lambda value of 1.5 was used to normalize LP LFC. After all parameters distributions were tested for normalization and/or normalized variance testing was preformed to determine which means test was going to be used. The Student's t-statistic was used to determine if the population means were significantly different from one another. The TM_TEST function in IDL was used to perform this task. The *p*-value needed to be less than 0.05 for the populations to be considered significantly different.

Model analysis

Simulations using sounding produced from both techniques, feature averaging and height averaging, are run for all approaches to moisture averaging using simple microphysics. Model output was analyzed using the objective precipitation classification method of Beatty et al. (2009), based upon the location of the precipitation centroid with respect to updraft (Fig. 10). The lowest radar elevation scan of 0.5° was used to estimate the near surface precipitation (Beatty et al. 2009). The low-level updraft location is estimated using a least squares linear regression approach, (see Beatty et al. 2009).

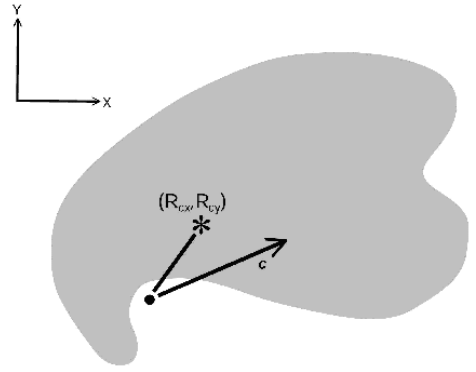

Fig. 10. Idealized supercell radar depiction. The black point is the extrapolated updraft at the map height. The asterisk represents the location of the rain rate centroid. C is the storm motion and speed. From Beatty et al. (2009).

Integrated maximum updraft helicity (Kain et al. 2010) was used as a constraint to keep the maximum updraft location located on the right moving supercell, and the maximum reflectivity centroid was also located with respect to the maximum updraft helicity. Threshold values from Naylor et al. (2012) were used for the various model grid spacing used herein. To determine the mode of convection i.e., rear/forward, the updraft was centered as the origin with the x and y axis being with respect to the updraft. There are some issues with Beatty's analysis methodology that needs to be taken into consideration. Beatty et al. (2009) determined the x-axis to be aligned with the storm motion direction when establishing a coordinate system for classifying forward or rear flank dominant precipitation mode. The current study proposes that this is incorrect and may artificially lead to an HP or rear flank bias. Instead, the current study aligns the x-axis with the 500 m to 4 km shear vector (see section *IIa*. above).

The example hodographs in Fig. 11 are Galilean Invariant, meaning these two wind profiles will produce identical storms in CM1. This is because supercells interact and respond to the vertical-wind shear-induced pressure gradient forces and not due to ground-relative wind speeds (Weisman and Klemp1982). The difference between the two storms is the storm motion direction. The storm on the left will have a storm motion to the northwest, while the storm on the right will have a storm motion to the southeast. This will change the detected mode of the supercell thunderstorm based off of the Beatty et al. (2009) approach of having the storm motion vector as the x-axis for the storm coordinates. To compare both of these methods, the analysis will be conducted both ways.

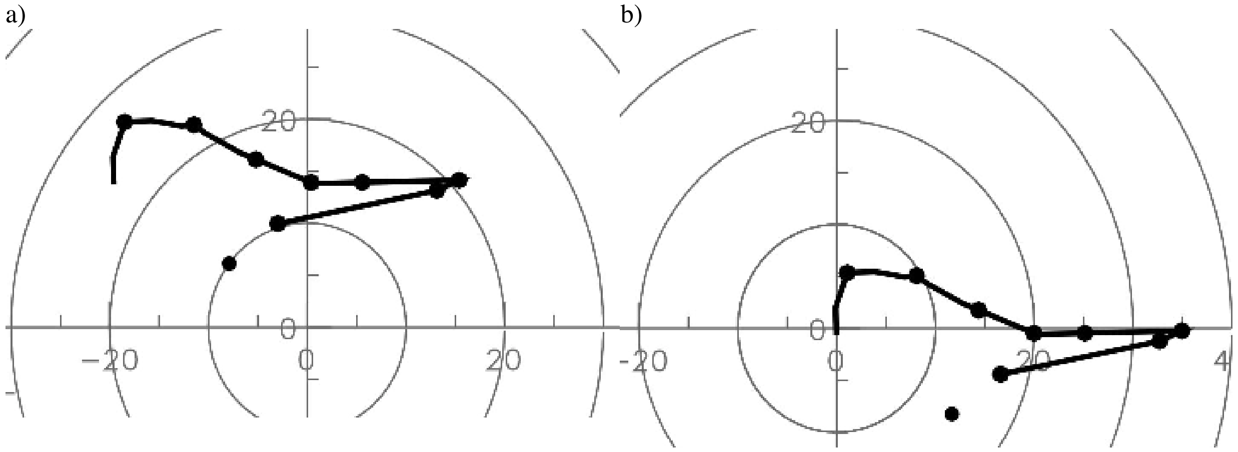

Fig. 11. Depicting the same shear magnitude located at different locations, which results in a different storm motion.

If using the Beatty et al. (2009) methodology this current storm (Fig. 12) simulated using the shown hodograph (Fig. 11a) would be classified as a rear flank precipitation dominant whereas it would be classified as forward-flank precipitation dominant with Fig. 11b. In the current study, using the 0.5-4 km shear vector as the x-axis, it is always classified as a forward flank dominant. Because the Beatty method will not give a consistent storm mode for the same exact storm structure, it seems like a faulty method.

Results from the two averaging techniques, four moisture-averaging techniques, and two methods of classification for the three environments are all compared within the results section. For comparison the cases that initially worked with 1 km horizontal grid spacing were rerun at 250 m horizontal grid spacing. After running every individual case, a new feature and height average composite was created using only the cases for which simulated storms lasted at least two hours. There are three LP, three CL, and three HP for each supercell classification that survived long enough for analysis.

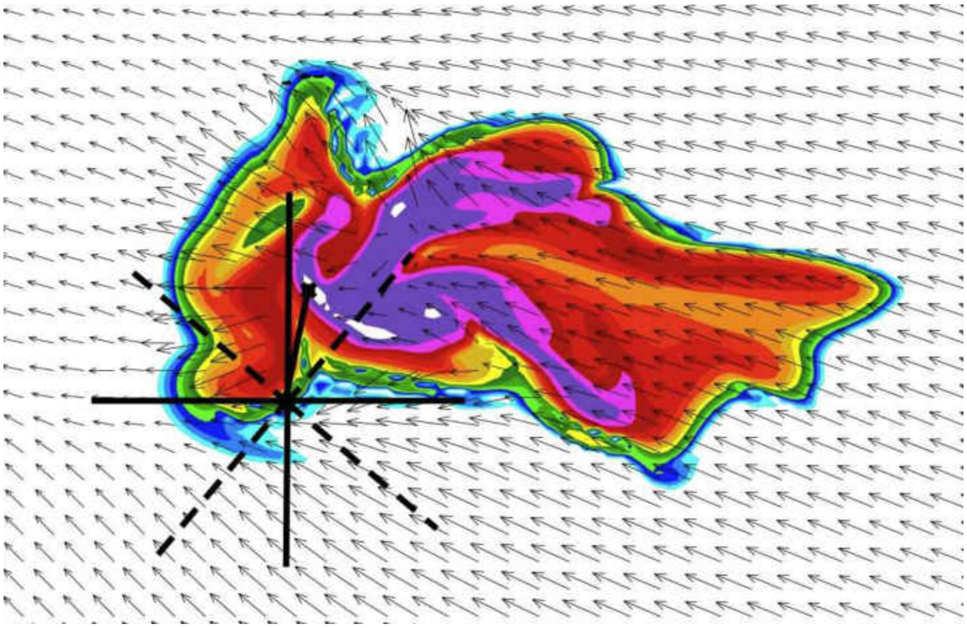

Fig. 12. Simulated reflectivity (dBZ) plot. The dashed lines indicate the x’ and y’ axes based upon the storm motion direction as applied by Beatty et al. (2009). The solid lines indicate x and y axis from current study. The center point for both axis systems is the updraft and the star indicates maximum reflectivity.

CHAPTER III

RESULTS AND DISCUSSION

The following results will be presented and discussed. First, the wind hodographs and associated parameters, will be presented for the individual soundings for comparison to the RS98 study and to determine whether the distribution means are significantly different between the LP, CL, and HP categories. Those distributions mean parameters will also be compared to the corresponding parameters from the feature and height average composite hodographs. A similar analysis will be shown for thermodynamic parameters like precipitable water (PW), CAPE, CIN, LCL, and LFC. Then the sensitivity to which moisture parameter is averaged and the affect that has on CAPE and CIN values for the feature and height averaged soundings will be presented. Finally, the end of the results will discuss preliminary findings from the CM1 simulations of the composite soundings and individual soundings using a modified Beatty et al. (2009) analysis methodology. This is used to determine if the soundings associated with LP/CL in nature result in simulated storms that are forward flank precipitation dominant with respect to the updraft and if soundings associated with HP storms in nature produce simulated storms that are rear flank.

a) Wind hodographs and derived parameters

The wind hodographs for both the feature and height averaged compositing techniques, constructed following the methodology section *II.b.i* and *II.b.ii*, will now be presented. They will be compared to each other, as well as among classes, and compared to the original distribution means. Because radar-observed storm motions were not reported by RS98, the current study uses a storm motion predicted from the mean hodograph following Bunkers et al (2000). There were only two variables that needed to be normalized for the distribution: HP 4-10 km shear magnitude and LP LFC.

i) Comparisons between the two-compositing techniques

There are many similarities between the height and feature average hodographs shown in Fig. 13. One of the biggest differences, though, is the stronger upper-level storm-relative wind for the LP feature average hodograph. In particular, the 9-10 km storm relative winds are approximately 2.5-3.0 m s^{-1} faster in the feature average hodographs than the height average (Table 2). This has a stronger impact on the storm relative winds than the storm motion differences since the respective storm motions in each class are so similar between the two composites (less than 1 m s^{-1} and 2° difference; Table 2). Also shown in Table 2 is that the 0-1 km and 0-3 km helicity differ little between their respective feature average and height average classes.

Table 2. Sounding statistics for feature and height average LP/CL/HP storms using the averaged soundings.

	0-1km Helicity (m^2/s^2)	**0-3km Helicity (m^2/s^2)**	**Bunkers storm speed (m/s)**	**Bunkers storm motion direction heading (degrees)**	**9-10km SRwind avg. (m/s)**	**PW Inches**
LP feature avg.	26	145	12.8	114°	22.4	1.2372
HP feature avg.	71	149	12.3	128°	18.1	1.4326
CL feature avg.	142	226	14.3	120°	23.0	1.3325
LP height avg.	33	139	13.7	114°	19.6	1.1098
HP height avg.	76	141	12.7	129°	15.6	1.2568
CL height avg.	143	225	14.3	122°	20.4	1.1042

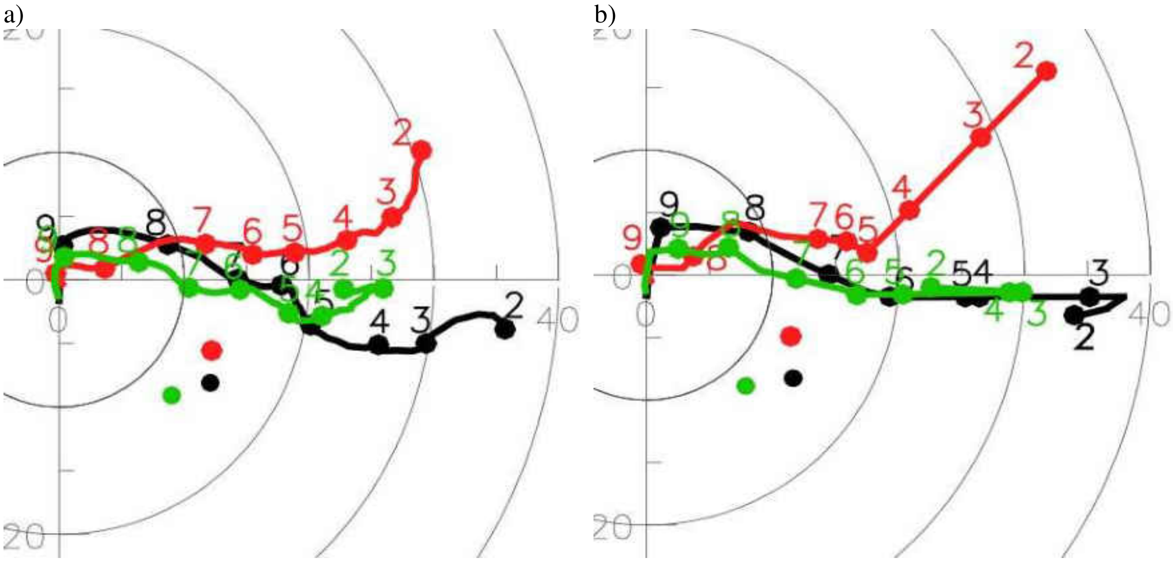

Fig. 13. (a) The LP (red), HP (green), and CL (black) a) height average hodographs and b) feature average hodographs. Corresponding colored dots indicate Bunkers Storm Motion.

ii) Variability in the winds at the location of each averaged feature

The greatest variability (greatest standard deviation) in the feature average hodographs is in the midlevels (Fig. 14) and this is seen by the size of the circle surrounding the 600 mb point. Although it visually seems that the mean HP feature average 0-3 km helicity is weaker, Table 2 shows that the LP mean is similarly weak.

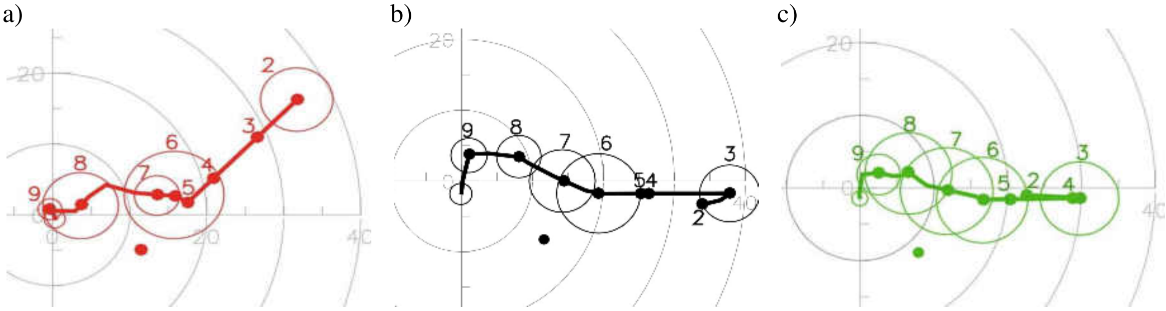

Fig. 14. Feature averaged wind hodographs with one standard deviation shown (radius of the circle) for a) LP, b) CL, c) HP. Note that the uncertainty (circle) is only shown at the average wind features elevations. Dots represent locations of the regular pressure levels in the hodograph where 9 is 900 hPa, 8 is 800 hPa, etc., and any co-located between those and the average elevations is coincidental.

iii) Comparison between average hodographs herein and RS98

Both composite hodograph types herein are in agreement with RS98's LP height average hodograph having a more positive v' component compared to the CL and HP hodographs. Differences between RS98's storm-relative parameters derived from their height average hodograph and the ones herein may also owe to the following: different storm motions used between the two studies; additional cases added herein from Beatty et al. (2009); cases omitted herein from RS98; RS98 modified their surface winds whereas they were not herein; RS98 calculated parcel sensitive parameters CAPE, CIN, LCL, LFC from surface base calculations whereas the study herein calculated using the lowest 100 mb mixed-layer calculations; RS98 only average dewpoint temperature for the moisture, while the study herein compares the differences in averaging of the moisture parameters: RH, T_d, e, q_v, or θ_w.

iv) Statistical differences between classes and comparison to RS98

The 9-10 km storm-relative winds computed with Bunkers et al. (2000) storm motion (herein) are very similar between LP and CL (Fig 15; bottom of first column) and, using statistical means testing (described in section 2c above), the respective distribution means could not be distinguished from one another. If the 9-12 km storm relative winds are indeed a predictor of storm mode (as earlier suggested by Rasmussen and Straka 1998), then this may explain why the radar behavior (shown in Beatty et al. 2009) had a forward flank precipitation maximum in both LP and CL cases.

Means testing of the wind parameters for the sounding groups herein reveals that only the HP-associated soundings differ from all other sounding classes with *p* value less than 0.05 (Fig. 15a).

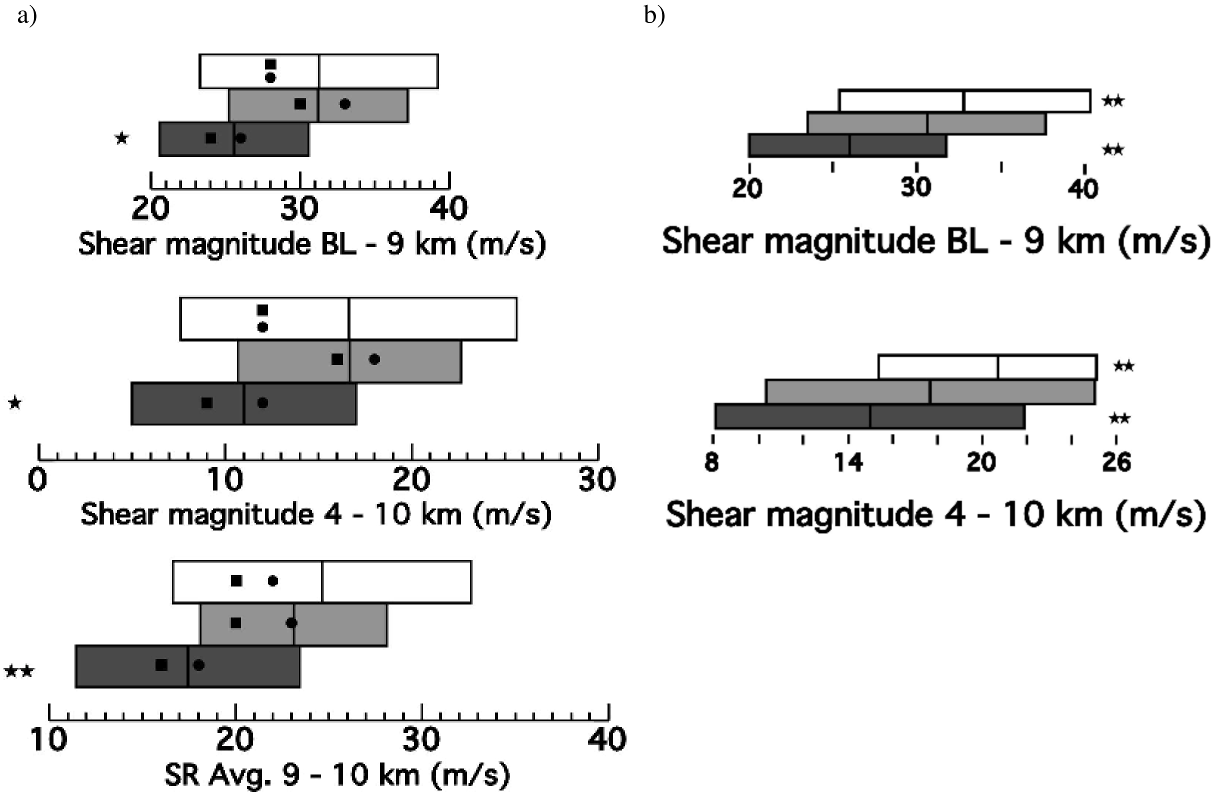

Fig. 15. Distributions of (Top) Shear Magnitude from boundary layer 0-500 m average winds to 9 km winds, (Middle) Shear Magnitude from 4 km winds to 10 km winds, (Bottom) Storm Relative 9 to 10 km average winds for a) the current study and b) RS98. The ends of the boxes represent ±1 standard deviation from the mean, which is the centered vertical line. One star (two stars) indicates that the mean of that category was significantly different than all other categories combined with *p* value less than 0.05 (*p* value less than 0.02). The RS98 paper did not create the SR Avg. 9-10 and so it is omitted. In “a)” the small solid square indicates the parameter computed from the height average composite, while the small solid circle indicates the parameter computed from the feature average composite. The top distribution of each plot is LP (white), middle distribution is CL (gray), and bottom distribution is HP (black).

The mean for BL-9 km shear magnitude and 4-10 km shear magnitude for HP supercells (Fig 15a) are significantly different, with a *p* value less than 0.05 comparing to the mean of CL/LP supercells. The HP mean storm relative 9-10 km winds are also significantly different at p value less than 0.02 when comparing to the mean CL/LP. RS98 differences were more significant (at the 0.02 level) for the LP and HP categories, however; perhaps this is because their dataset included more soundings. Thus, the HP storm results herein did agree with RS98's written claim that HP storms had the slowest 9-10 km storm relative velocities. (RS98 showed a plot of storm-relative winds at that level but did not conduct means testing which is why the plot is only found herein.)

Finally, because the overlaid values from the feature and height average soundings (squares and circles on Fig. 15) were not consistently closer to the distribution mean for all parameters, then one cannot conclude that the feature or height average was consistently more representative of the distribution in that class.

b) Thermodynamic soundings and derived parameters

The soundings using both the feature and height averaged compositing techniques, constructed following the methodology section 2b.i and 2b.ii, will now be presented. They will be compared to each other, as well as among classes, and compared to the original distribution means.

i) Comparisons between the two-compositing techniques

The following shows the mixing ratio composite soundings for LP/CL/HP with the feature and height averaging overlaid for comparison purposes (Fig. 16). As was the case for the wind hodographs, the composite sounding is comprised of all the soundings in a particular class. A second version of these soundings will be considered later in the simulation section, which only contains the average of the soundings that individually produced sustained supercells in the model. Notice that the above composites were constructed using water vapor mixing ratio as the averaged moisture variable. The calculations in the remainder of section 3c use these composites. In section 3d, different moisture variables are averaged to establish sensitivity.

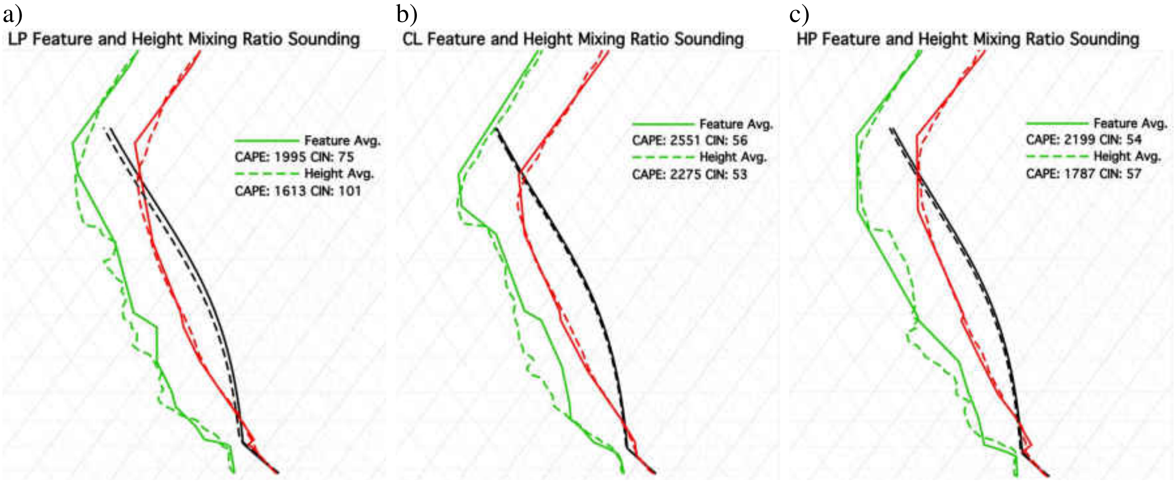

Fig. 16. Skew-T Log P diagrams, with mixing ratio as the averaged moisture parameter, for feature average (solid) and height average (dashed) for the a) LP, b) CL, and c) HP.

Comparing the feature to height average soundings, one can see that the feature average soundings always have more CAPE and less CIN for the HP and LP composites (Fig. 16) and greater *PW* (Table 2) compared to the height average sounding. The capping inversion is well retained in the feature average composite compared to the height average composite.

ii) Variability in the thermodynamics at the location of each averaged feature

Similar to Section 3aii for the wind hodographs, the following figures in this section show the variability in the temperature and moisture profiles (both magnitude and altitude) of each thermodynamic feature that was averaged during the compositing process. It will be shown that there is much more variability, particularly with moisture, in the midlevels than other locations in the sounding. Midlevel moisture is known to be very important to downdraft strength and the resulting cold pool strength at the surface (e.g. Gilmore and Wicker 1998).

Now the LP, CL, and HP composites will be discussed. The LP individual cases that make up the LP composites (feature average) are highly variable at the selected points on the sounding (Fig. 17a,b). The points were arbitrarily picked to visualize the amount of variability in the temperature and moisture. The moisture is more variable compared to temperature (Fig. 17). The whiskers on Figs. 17-19 denote one standard deviation in pressure and in the temperature and moisture. Figs. 18 and 19 shows the corresponding CL and HP feature average sounding, respectively. The CL composite has a smoother capping inversion due to the majority of the individual CL soundings having a weaker inversion (less sharp). Fig. 19, the HP composite sounding, shows the least (most) amount of variability above the 500 mb level (below the 600 mb level) compared to LP/CL composites. The figures below are presented to help visualize the variability in the dataset. Section 3bv below provides the sensitivity of the sounding composite and associated parameters to the moisture variable that is averaged.

iii) Comparison between average skew-T diagrams herein and RS98

Although they constructed average hodographs, RS98 did not construct average skew-T log-*p* diagrams. Therefore, it is not possible to compare the height average diagrams herein to RS98. However, RS98 did calculate statistics for each of their sounding in each class and that will now be compared.

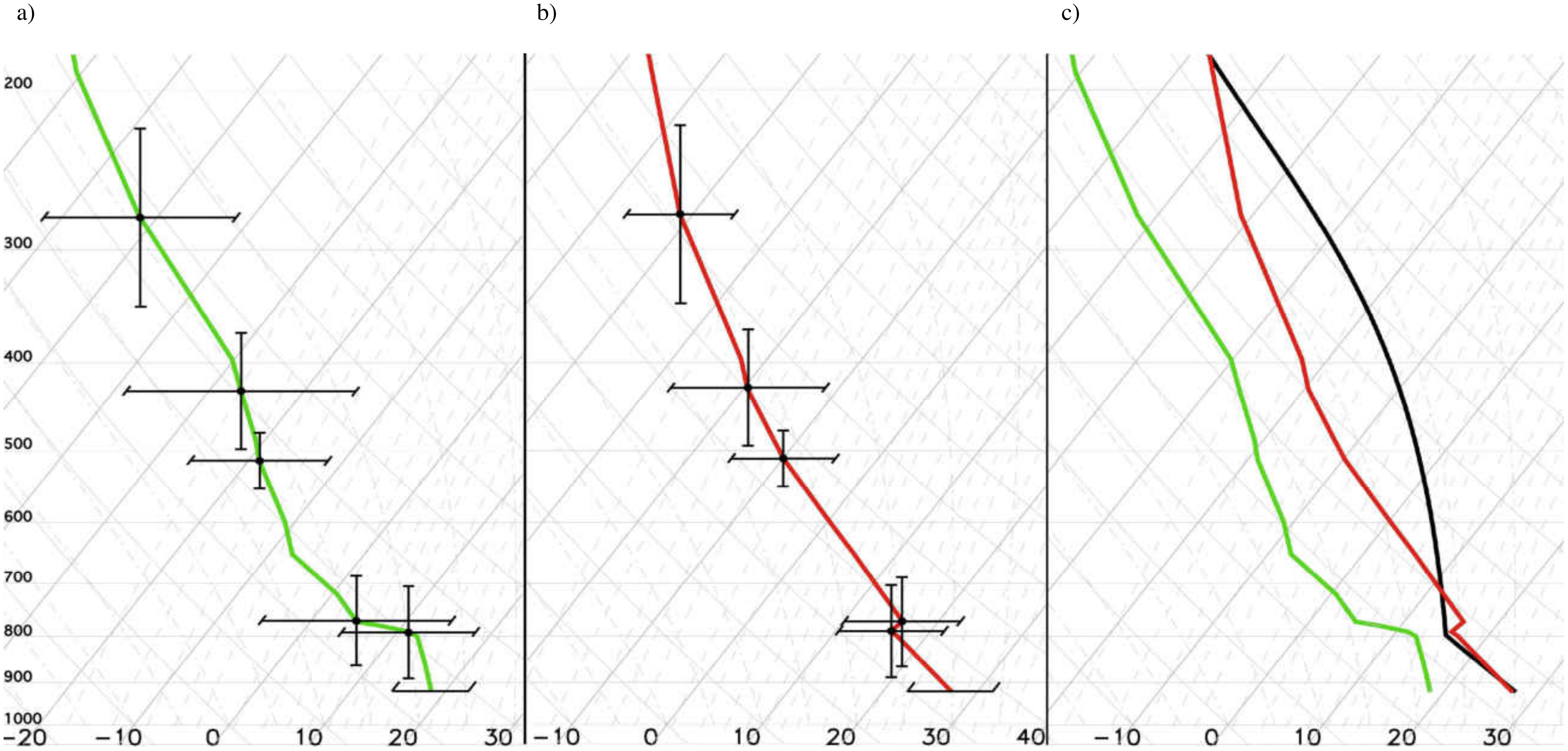

Fig. 17. LP feature average skew-T log-p sounding of a) dewpoint temperature, b) temperature, and c) overlays in temperature (red), dewpoint temperature (green), and lowest-100 mb-averaged parcel path (thicker black line). This was constructed using *qv* as the moisture variable. The darker horizontal and vertical lines in “a)” and “b)” are whiskers showing the standard deviation in temperature and pressure at selected heights.

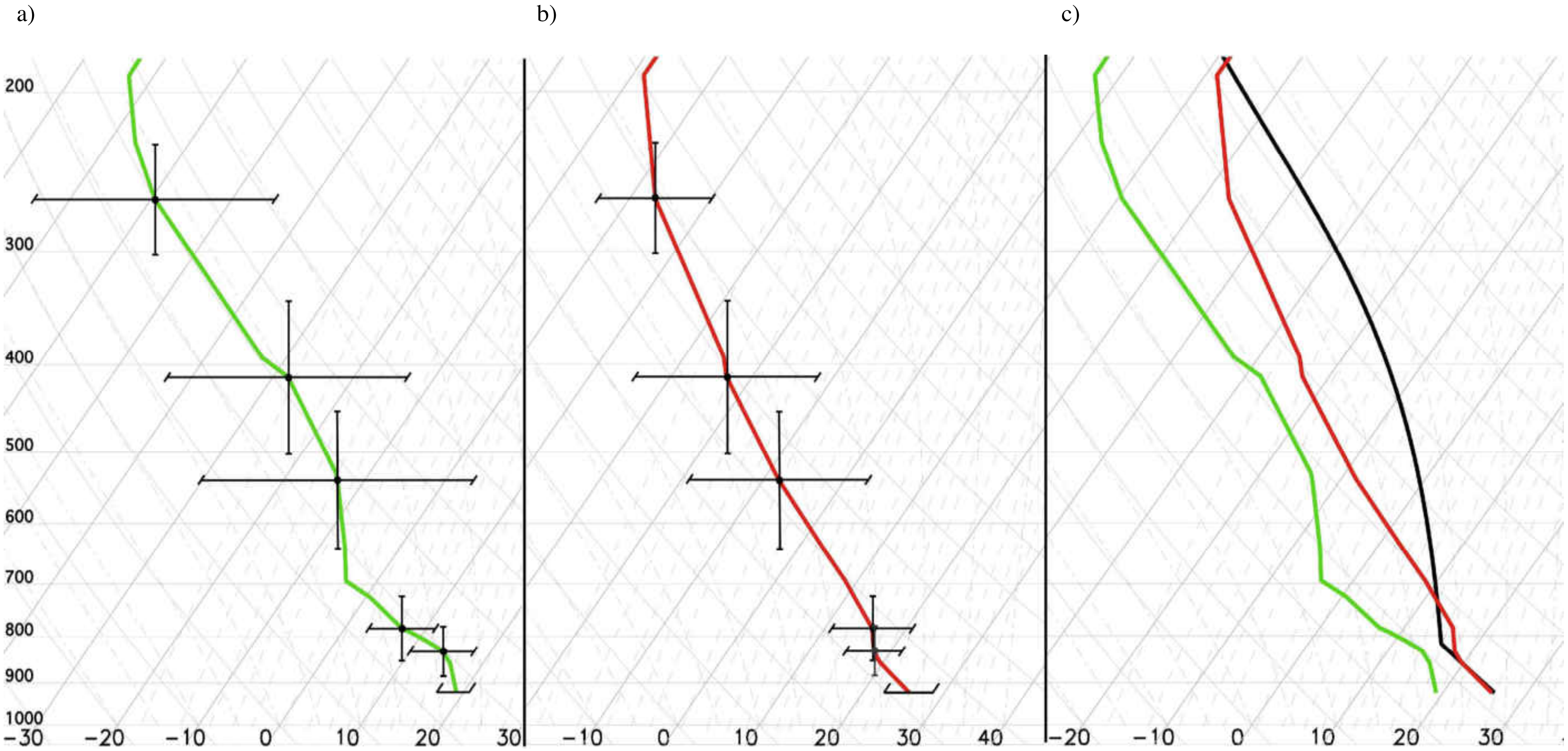

Fig. 18. CL feature average skew-T log-p sounding of a) dewpoint temperature, b) temperature, and c) overlays in temperature (red), dewpoint temperature (green), and lowest-100 mb-averaged parcel path (thicker black line). This was constructed using *qv* as the moisture variable. The darker horizontal and vertical lines in "a)" and "b)" are whiskers showing the standard deviation in temperature and pressure at selected heights.

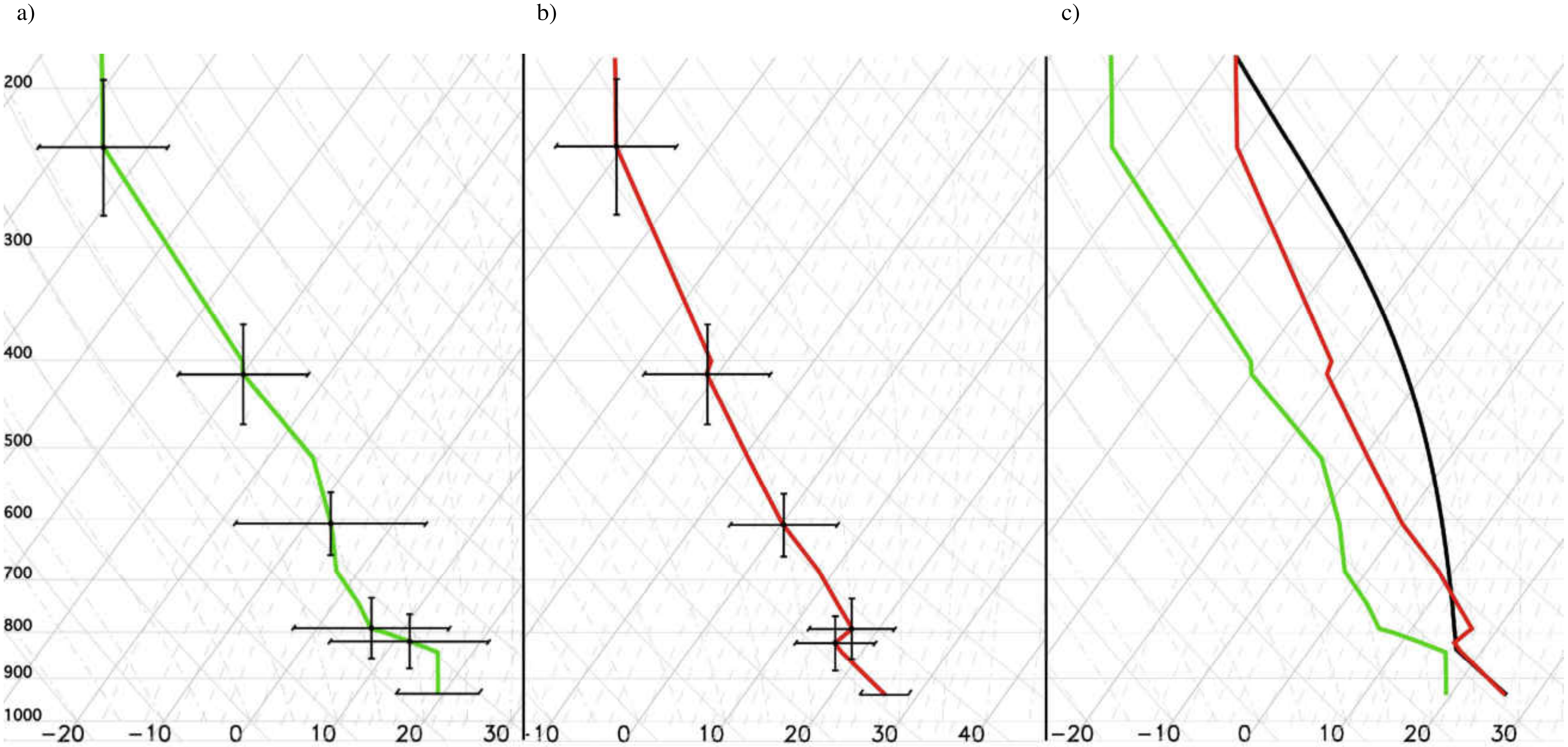

Fig. 19. HP feature average skew-T log-p sounding of a) dewpoint temperature, b) temperature, and c) overlays in temperature (red), dewpoint temperature (green), and lowest-100 mb-averaged parcel path (thicker black line). This was constructed using *qv* as the moisture variable. The darker horizontal and vertical lines in “a)” and “b)” are whiskers showing the standard deviation in temperature and pressure at selected heights.

iv) Statistical differences between classes and comparison to RS98

Similar to what was done for the wind parameters above, the means of the thermodynamic-derived sounding parameters were also statistically compared between the LP, CL, and HP groups. First, it can be seen that the parameters computed from each height average sounding (squares, Fig. 20a) and the feature average (circles, Fig. 20b) composites are consistently, inconsistent. There is one parameter where the feature average value is larger than the mean distribution and the height average value (*PW*), while for some parameters the height average value is lager than the mean distribution and the feature average value (SBLFC). Then for one parameter the mean distribution, feature and height average values are almost identical (SBLCL). Second, the small differences between the distributions for each class herein and from RS98 can likely be attributed to the datasets not being exactly the same (or due to RS98's modification of surface data). There will be more comparisons below.

The distributions of *PW* across the spectrum and individual means for each class appear similar to RS98 (compare Fig. 20a to 20b). However, CL herein (Fig. 20a) has a smaller standard deviation of *PW* compared to that of RS98 (Fig. 20b). Also, there are slightly higher mean *PW* amounts herein, by about 0.2 inches, compared to each respective class in RS98 (c.f., Figs. 20a and 20b). LP and CL mean (Fig. 20a) is approximately 1.2 in., while the RS98 LP and CL mean (Fig. 20b) is slightly over 1.0 in. The HP mean *PW* (Fig. 20a) is slightly over 1.4 in. compared to the HP mean *PW* (Fig. 20b) is slightly over 1.2 in. Also, oddly, in the current study there was no significant difference found between the means across the spectrum, which is not consistent with RS98's finding that the HP mean is significantly different at a *p*-value less than 0.02.

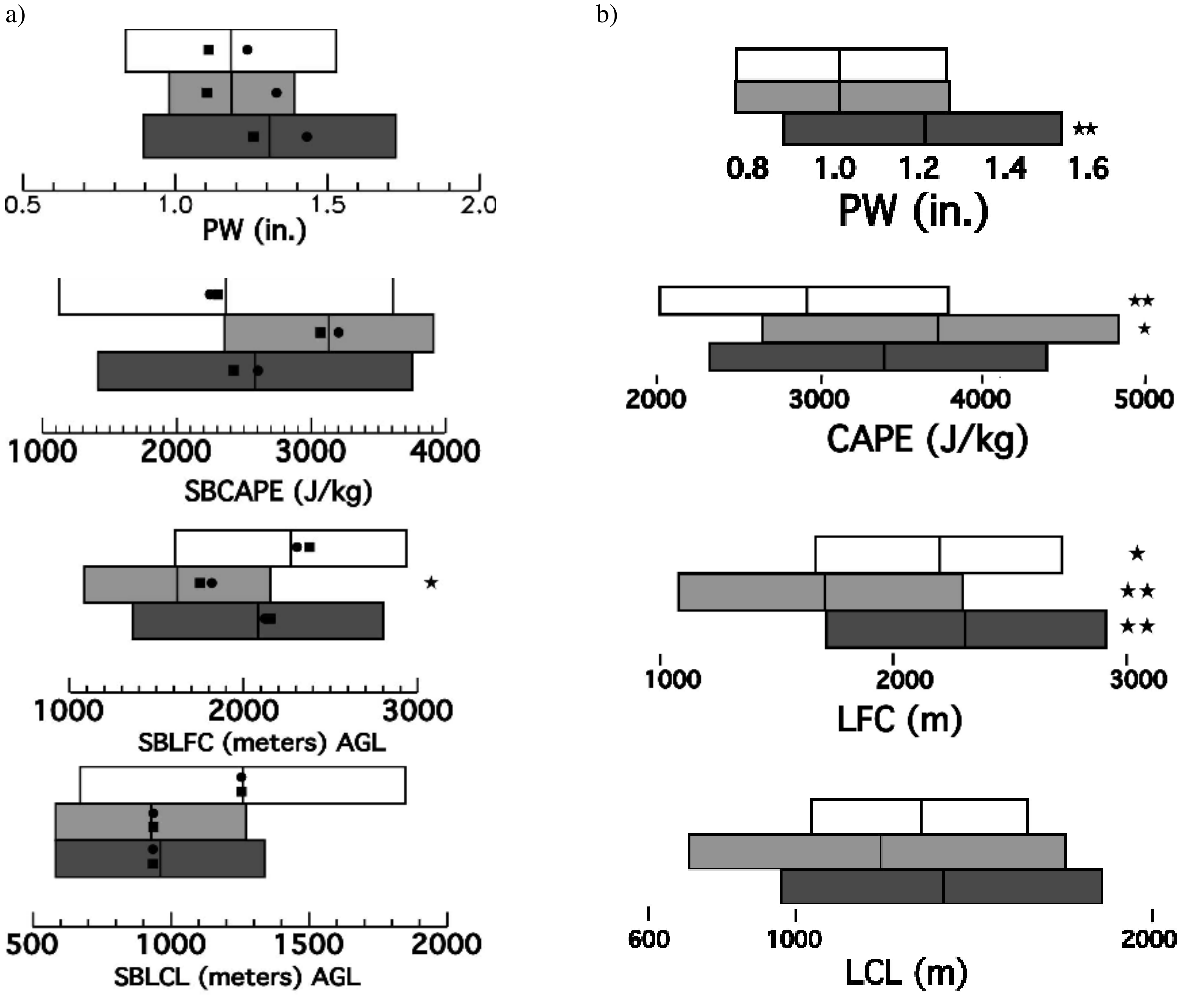

Fig. 20. As in Fig. 15 except showing distributions of Precipitable water (in.), SBCAPE, SBLFC, and SBLCL for the three classifications top (white) LP, middle (gray) CL, and bottom (dark gray) HP for (left). The ends of the boxes represent ±1 standard deviation and the vertical line represents the mean Precipitable Water, surface-based CAPE, surface-based LCL height, and surface-based LFC height from a) soundings used herein and b) soundings used in RS98. Additionally, the small solid squares overlaid in "a)" indicates the values computed from the height average soundings (where *qv* was the averaged moisture variable) and the solid circles indicates the values computed from the feature average soundings.

Comparing the surface based CAPE from the current study to RS98; the relative distributions between LP, HP, and CL are similar between the studies for both CAPE and LFC. Also, the surface based CAPE and LCL values are both slightly lower herein compared to RS98 (Fig. 20b) - likely attributed to RS98's modification of the surface data in the soundings and greater number of soundings used. The CL and HP standard deviations in LCL height are both smaller herein compared to RS98 whereas the opposite is true for the LP LCL standard deviations. Also, the distribution for the current study has overall lower LCL heights for HP class compared to the RS98 study. For instance, the lower end of the standard deviation in the HP class in current study ends at 600 m AGL (Fig. 20a), while the lower end of the standard deviation in the HP class from the RS98 study ends around 900 m. Although the upper ends of the HP LCL heights are similar between the current study and RS98, the current study has a smaller standard deviation (1350 m), compared to RS98 (1800 m; Fig. 20b). The means for the CL and HP distributions are also significantly different with p values less than 0.02. In the current study the CL mean LFC height was found to be significantly different from the means of the LP and HP distributions, with a p value less than 0.05.

Notice that the previous discussion only considered surface-based parcels. However, mixed-layer parcels are sometimes considered more useful by forecasters and would be less sensitive to the surface values (as altered by RS98). Thus, the following section compares how the interpretation of the statistical results changes when using a mixed layer parcel instead of the surface-based parcel as well as how the parcel-dependent parameters change when computed for the feature and height average composites.

Comparing the thermodynamic parameters from distributions using surface-based parcels (Fig. 21b; mimicking RS98) to those from the lowest-100-mb average mixed-layer parcels (Fig. 21a), the following differences are seen. For all supercell categories, the overall CAPE values for the mixed layer calculations are smaller and the CIN standard deviations are larger compared to the surface based parcels. Also, while the mean LP CIN values are very similar between the mixed layer and surface based parcels, they are quite different for CL and HP.

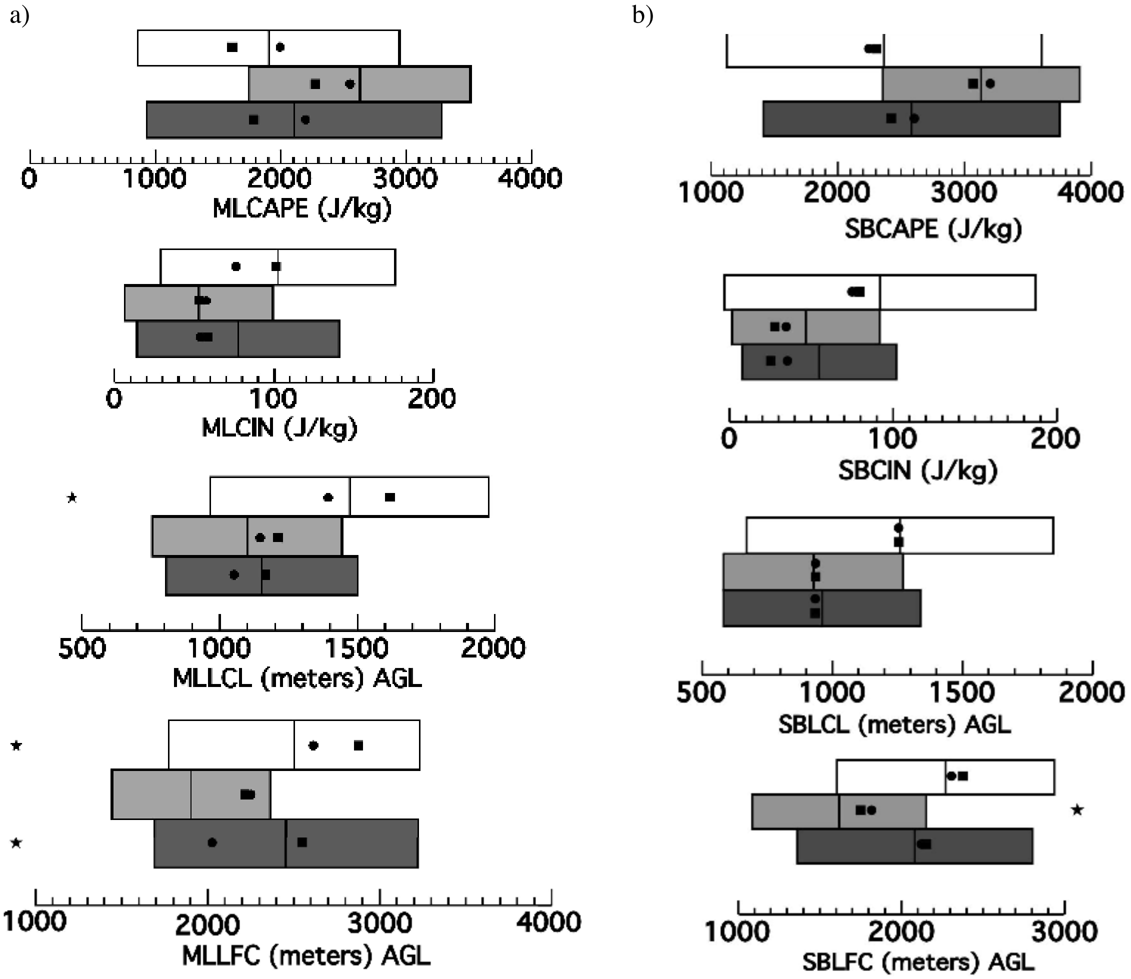

Fig. 21. Same as Fig. 20 except comparing a) mixed-layer parcels to (b) surface-based parcel when computing CAPE, CIN, LCL, and LFC.

How sensitive is the means testing to whether one uses surface based versus mixed layer parcels? This is demonstrated by comparing the LCL and LFC distributions. The mixed layer parcels are able to bring out differences that were not seen with the surface based parcels (Fig. 21). The mixed layer LP mean LCL height is significantly different with a p value less than 0.05 comparing to the CL and HP mean LCL height.

For the surface based parcels, there is no significant difference found between the distribution means. The mixed layer LP mean LFC height and mixed layer HP mean LFC height are significantly different when comparing against the mean value of the other classes (bottom; Fig. 21a). The surface based CL LFC mean height is significantly different compared to the means of the LP and HP mean LFC height (bottom; Fig. 21b).

How do the parameters calculated from the composite sounding compare to the mean parameter values of each distribution? The feature average composite sounding CAPE (small circles overlaid in Fig. 21) is consistently closer to the distribution mean and higher than the height average composites (small squares). The same is not true for the surface based calculations. For the surface based parcels the feature and height average have closer values compared to the mixed layer parcels (Fig. 21b). This makes sense since the average surface values are identical between the height and feature average soundings. Because there is no consistent pattern (in having one composite type closer to the distribution mean for either the surface based or mixed layer parcels), then one ***cannot*** conclude from this analysis that the feature average sounding is a better representation of the overall group than the height average sounding.

c) Sensitivity of the compositing technique to the moisture variable chosen for averaging

As previously discussed in Section 2b, five different moisture variables were averaged using (10). Although it may seem straightforward to average q_v and T_d, it becomes complicated when one chooses to average vapor pressure (e), relative humidity (RH), or wetbulb potential temperature (θ_w). The key to a consistent averaging is to convert all sounding points into the moisture parameter of interest first before using (10).

For instance, when obtaining the average vapor pressure, one must compute all of the vapor pressure individually first (using 14) rather than using the previously computed $\bar{T}_d$ (15).

$$\bar{e}(T_d) = \frac{\Sigma\left[6.112exp\left(\frac{17.67*T_{d1}}{T_{d1}+243.5}\right)+6.112exp\left(\frac{17.67*T_{d2}}{T_{d2}+243.5}\right)+\cdots+6.112exp\left(\frac{17.67*T_{dn}}{T_{dn}+243.5}\right)\right]}{n} \qquad (14)$$

$$e(\bar{T}_d) = 6.112exp\left(\frac{17.67*\bar{T}_d}{243.5+\bar{T}_d}\right) \qquad (15)$$

incidentally, (14) gives a larger vapor pressure compared to (15), thus slightly boosting the amount of moisture for the feature average sounding. This helps to explain why the "e" average in Table 3 always gives a larger CAPE and lower CIN than the T_d average. If one had instead used (15), then the $e(\bar{T}_d(z))$ would give the same plotted moisture profile as $\bar{T}_d(z)$ and no comparison would be necessary.

The composite soundings created by averaging *RH* give the largest values of CAPE and boundary layer moisture, when plotted. This is consistent for the LP and CL for both compositing techniques (both feature and height) whereas HP soundings have second-to-largest values when *RH* is averaged (Table 3). When averaging *RH* there are two possible techniques that were explored but only (16) uses a consistent application of (10). The following denotes both methods:

$$\overline{RH}(e, e_s) = \frac{\Sigma\left(\frac{e_1}{e_{s_1}}*100+\frac{e_2}{e_{s_2}}*100+\cdots+\frac{e_n}{e_{s_n}}*100\right)}{n} \qquad (16),$$

$$RH(\bar{e}, \bar{e_s}) = \left[\frac{6.112*\exp\left(\frac{17.67*\overline{T_d}}{\overline{T_d}+243.5}\right)}{6.112*\exp\left(\frac{17.67*\bar{T}}{\bar{T}+243.5}\right)}\right]*100 \qquad (17).$$

The correct application obtains $\overline{RH}(e, e_s)$ by using *RH* for each level (using *e* and e_s calculated from each level's T_d and T, respectively). A second method would be to use the previous calculations of $\overline{T}_d$ and $\overline{T}$ to calculate the $\bar{e}$ and $\bar{e}_s$ to achieve a mean *RH* (17). The two averaging techniques will give slightly different values with (16) giving higher relative humidity compared to (17). The one that was used and is described in later parts of this thesis is (16) since it is consistent with (10). The following will show the differences in CAPE and CIN between each classification and which moisture parameter was averaged (Fig. 22).

Averaged *RH%* provides the largest CAPE and lowest CIN values, while averaged T_d, which most previous studies average to create a composite sounding, provides the least amount of CAPE and the most amount of CIN. There is up to a 37% variation in the CAPE values (LP; height average) and a 65% variation for the CIN values (HP; feature average) between the largest and smallest moisture parameters chosen for averaging (Table 3). The results sort consistently, with *RH* providing the moistest sounding averages, except for the HP classification where the vapor pressure provides a slightly more moist average resulting in higher CAPE and lower CIN values than *RH*. The feature average composite preserved large CAPE and lower CIN values compared to the height average composite. The moisture parameter that results in the driest sounding average is T_d. This is important to mention since, as mentioned in the methodology all previous studies in the literature apparently averaged T_d when compositing.

Consistent with Table 3 is Fig. 22, which shows the sounding differences, particularly in the boundary layer, that result when creating sounding composites by averaging different moisture parameters. When averaging relative humidity, this gives the largest CAPE values and lowest CIN values for LP and CL supercells.

Table 3. Lowest 100-mb mixed layer parcel CAPE and CIN values for composite soundings that use the shown moisture variable in feature (F) and height (H) averaging procedure. Rows are sorted by decreasing CAPE and increasing CIN (except for first two rows of HP).

Moisture Variable Averaged	**LP**				**CL**				**HP**			
	CAPE		**CIN**		**CAPE**		**CIN**		**CAPE**		**CIN**	
	F	**H**	**F**	**H**	**F**	**H**	**F**	**H**	**F**	**H**	**F**	**H**
RH	2426	1935	53	79	2862	2506	41	42	*2432*	*1909*	40	48
Vapor p	2182	1740	64	92	2735	2429	47	45	*2466*	*1990*	38	42
Mixing Ratio	1995	1613	75	101	2551	2275	56	53	2199	1787	54	57
Theta-w	1964	1522	76	108	2525	2245	57	54	2117	1685	59	64
Dewpoint T.	1814	1460	85	113	2486	2193	60	57	2025	1629	66	69
Variation between largest & smallest	34%	37%	60%	43%	15%	14%	46%	36%	20%	17%	65%	43%

For HP storms preserving the vapor pressure gave slightly larger CAPE and lower CIN values compared to preserving the relative humidity. There is consistency across all three spectrums and both averaging techniques. For LP and CL feature and height average the highest moisture to lowest moisture in boundary layer are as follows: relative humidity, vapor pressure, mixing ratio, wet-bulb potential temperature, and dewpoint temperature. For HP feature and height average the highest moisture to lowest moisture in boundary layer are as follows: vapor pressure, relative humidity, mixing ratio, wet-bulb potential temperature, and dewpoint temperature. As was argued in the introduction, for either the feature or height averaging technique, mixing ratio is likely the best moisture parameter to average because it is not pressure and temperature dependent like the others are (relative humidity, vapor pressure, and dewpoint temperature). In other words, because mixing ratio is preserved as air cools and expands as it rises, then it would seem reasonable that one could mix parcels from different altitudes (at different p and T).

However, for modeling purposes, it may be advantageous to consider preserving *RH* due to the larger CAPE values and lower CIN values to simulate longer-lived supercells.

The following section will introduce the simulation conducted using both the LP/CL/HP supercell composite soundings as well as the individual soundings from each class. The reflectivity plots for each precipitation classification are shown and discussed along with trend plots showing differences/similarities in the updraft strength and updraft helicity (used to determine supercell longevity).

d) Simulations

i) Simulations using composite soundings

The initial simulations were initialized with respective composite LP, CL, and HP soundings to test whether the differences in the storm mode could be captured, as opposed to running every case individually and interpreting each case for LP/CL/HP. In these simulations, every sounding in each class was used in creating the composite soundings and both the height average sounding as well as the feature average sounding was tested. The domain size is 120 km by 120 km by 20 km with 1 km horizontal grid spacing and 250 m vertical grid spacing. The w-forcing storm initiation method was also tested for both 0-900 s and 0-1200 s in order to see which gave storms with at least 10 m/s lasting through 7200 seconds. It was discovered that the 0-900 s application worked best, consistent with Naylor and Gilmore (2012), and all subsequent simulations used that setting. Those simulations that lasted at least 5400 seconds were then re-simulated for 3 hours of cloud time at 250 m horizontal grid spacing. The finer grid spacing runs resolved more features compared to the 1 km run and had stronger updrafts (following Bryan et al. 2003).

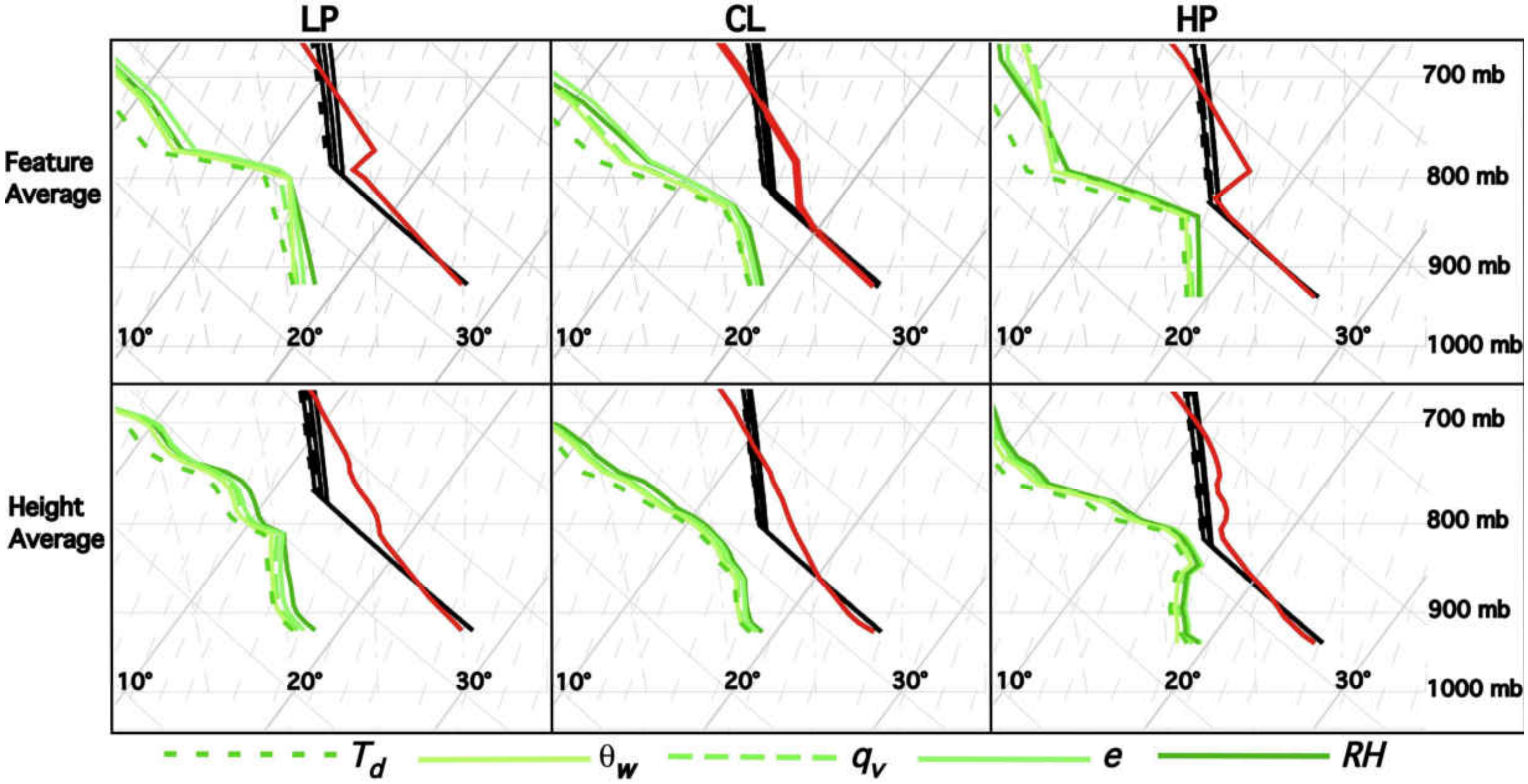

Fig. 22. Skew-T Log-p diagrams showing (top row) feature average soundings and (bottom row) height average soundings showing the result of using the following five different moisture variables during averaging (from left to right): T_d, $_w$, q_v, e, and RH. The temperature line (red) is only shown once for each case, as it does not differ. The line style used for each different moisture parameter is consistent for the moisture and updraft adiabat for that specific case.

For each classification, instead of using the 10 m s^{-1} threshold, the individual storms were deemed successful at 250 m grid spacing using the supercell detection algorithm described within Naylor et al. (2012). For the remainder of the results section below, the dx=250 m simulations are discussed. Recall that the feature average soundings preserved much more moisture through all cases compared to the height average soundings (refer to Table 3 above). In both the feature average and height average sounding cases, the trends between LP and CL were similar having the moisture parameters progressing from lowest to highest as follows (T_d, θ_w, q_v, e, RH). For the feature and height average sounding cases, the trend for HP were similar having the moisture parameters progressing from lowest to highest as follows (T_d, θ_w, q_v, RH, e). However, the differences among classes were larger for the height average. This detail about differences in feature and height average soundings is important when discussing the simulation results below.

The CL feature average storm lasted 1500 s following the supercell identification criteria from Naylor et al. (2012) where it was found that a storm simulated at dx=250 m grid spacing needs at least an 480 $m^2 s^{-2}$ updraft helicity value to be deemed a supercell at any given time. The CL storm had brief helicity values over 480 $m^2 s^{-2}$ past 2400 s but was short lived (not shown). The HP feature average storm lasted 1500 s, while the LP feature average storm lasted 1200 s, with only one supercell detection after the first 20 minutes (Figs. 23-25). In all cases (both feature and height average), supercells were not detected after 30 minutes. This is despite using the *RH* feature average soundings that had the highest CAPE and lowest CIN values. They were not able to produce long-lived supercells.

One can see that there are little differences in the evolution of the storms between the feature and height average composites, as viewed using plan view maps of radar reflectivity (Figs. 23-25) and thus neither averaging type is preferred in providing a long-lived storm. The gust front (and low-level updraft) is out ahead of the hook echo and midlevel updraft in all cases by t=30 min (Figs. 23-25). Part of this may be due to the large CAPE of the environment and excessive precipitation produced during the initiation phase using the w-forcing technique. Excessive precipitation is one well-known reason for storms “gusting out” (McPherson and Droegemeier 1991). Another possibility is that the LFO single-moment microphysical parameterization scheme tends to produce cooler cold pools compared to Morrison double moment scheme, which tends to have warmer cold pools (Figs. 26-28).

ii) Sensitivity of results to the microphysics scheme used

Thus, another simulation was conducted, for the LP/CL/HP feature average cases only, using the Morrison microphysics scheme (Morrison 2005). All parameters were identical to those described earlier in this results section, including horizontal grid spacing of 250 m and wforcing initiation time of 900 s. This was done to determine if a double moment scheme would be able to capture the radar reflectivity differences that the single moment did not between the three classifications LP/CL/HP. The updraft helicity is the maximum in the domain and usually associated with the supercell except for later times when it weakens. This might not always be true, however, for individual cases the maximum updraft was associated with the supercell in most cases, otherwise it was manually checked

Feature average low precipitation supercell sounding

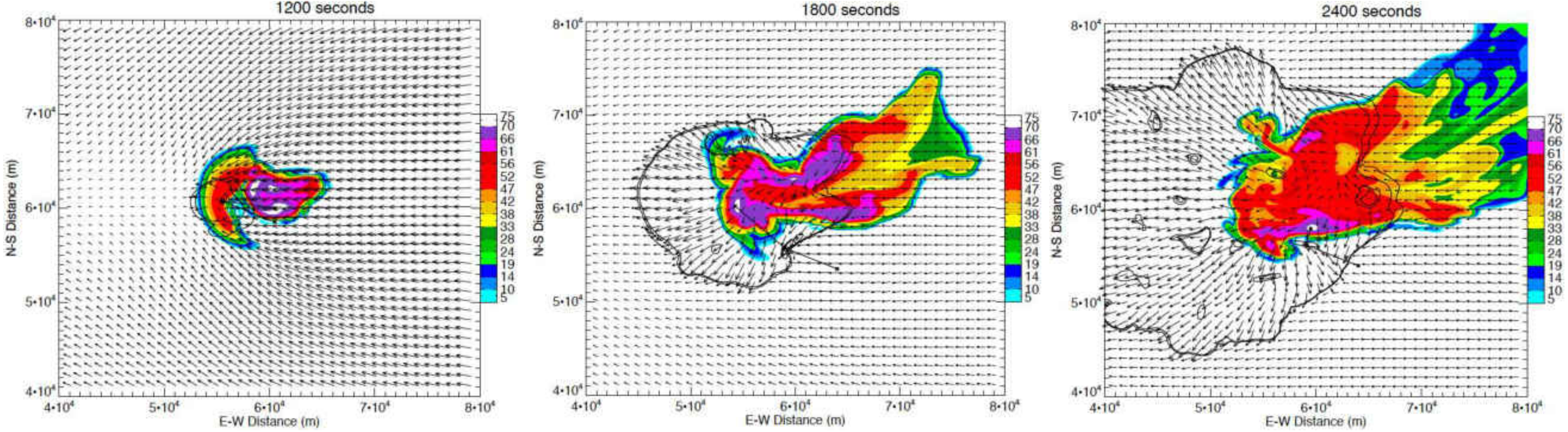

Height average low precipitation supercell sounding

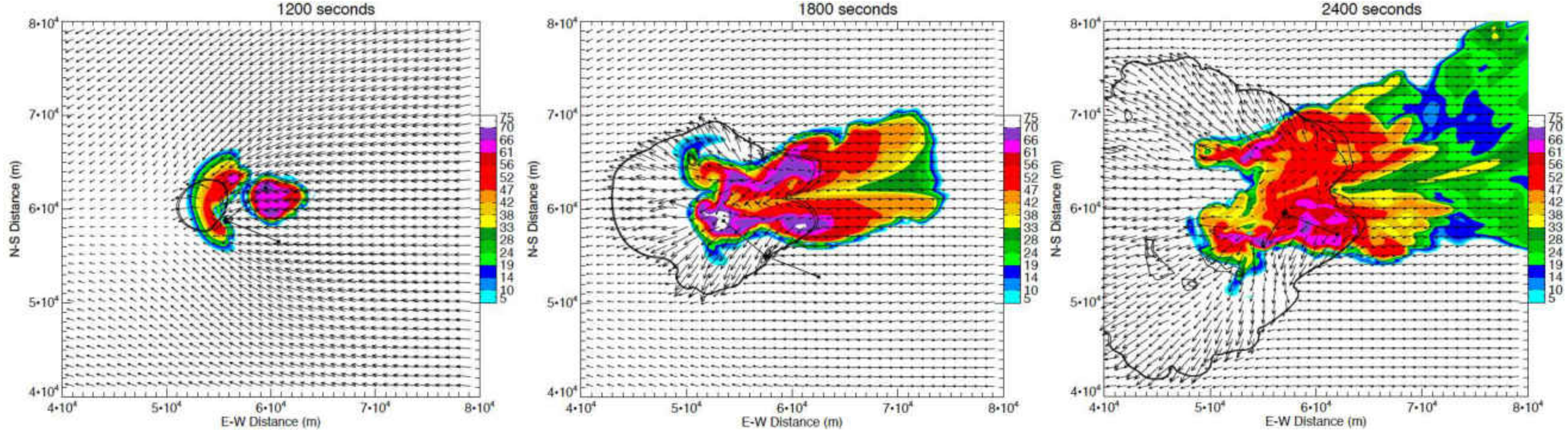

Fig. 23. Top showing a cross section of the simulated storm for the (top row) feature averaged LP supercell sounding and (bottom row) height average LP supercell sounding at dx=250 m grid spacing. Winds are shown at the surface with reflectivity plotted at the 2.5 km AGL. The outer black contour is the perturbation of -0.5° C.

Feature average classic supercell sounding

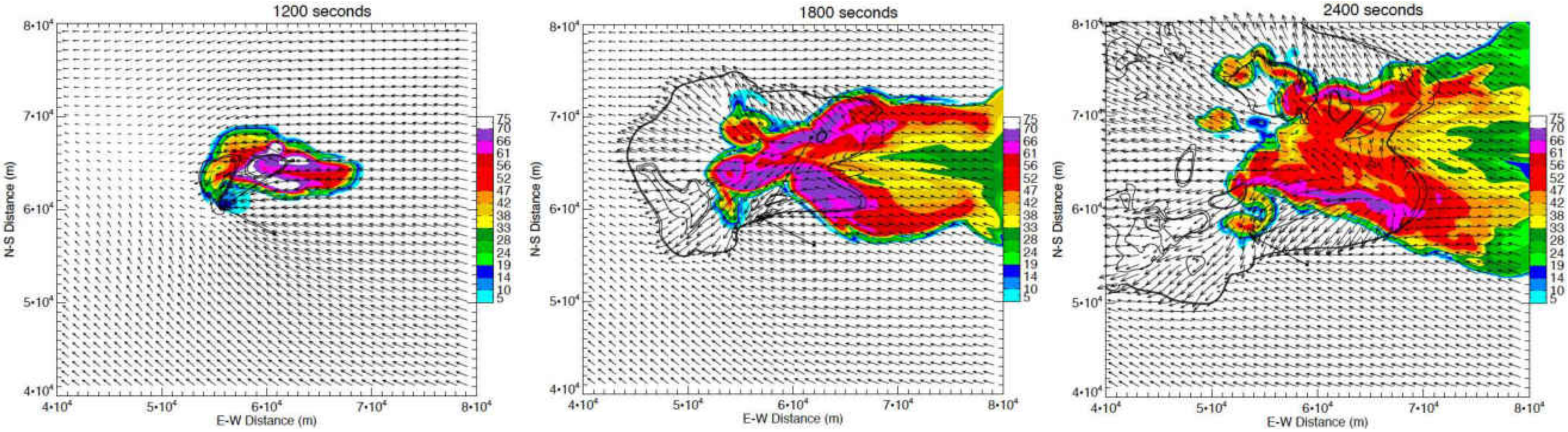

Height average classic supercell sounding

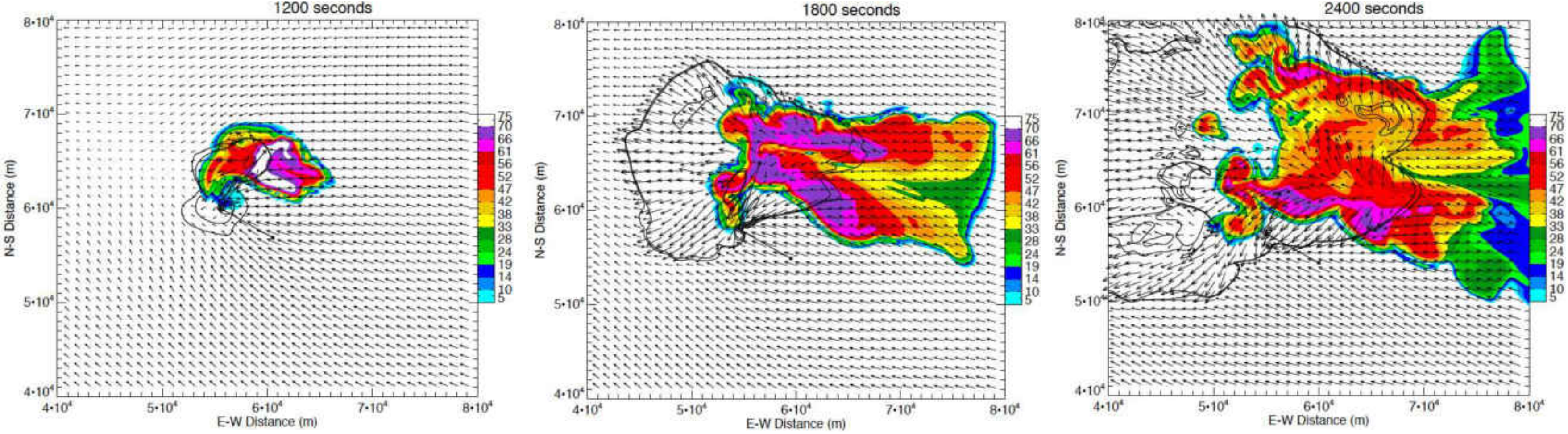

Fig. 24. Top showing a cross section of the simulated storm for the (top row) feature averaged CL supercell sounding and (bottom row) height average CL supercell sounding at dx=250 m grid spacing. Winds are shown at the surface with reflectivity plotted at the 2.5 km AGL. The outer black contour is the perturbation of -0.5° C.

Feature average high precipitation supercell sounding

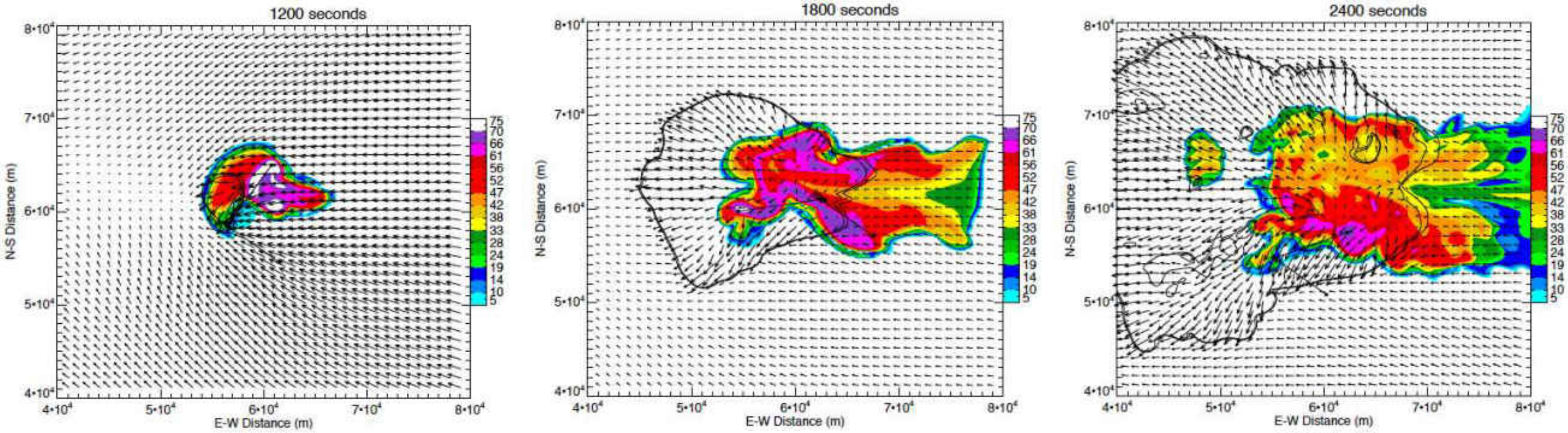

Height average high precipitation supercell sounding

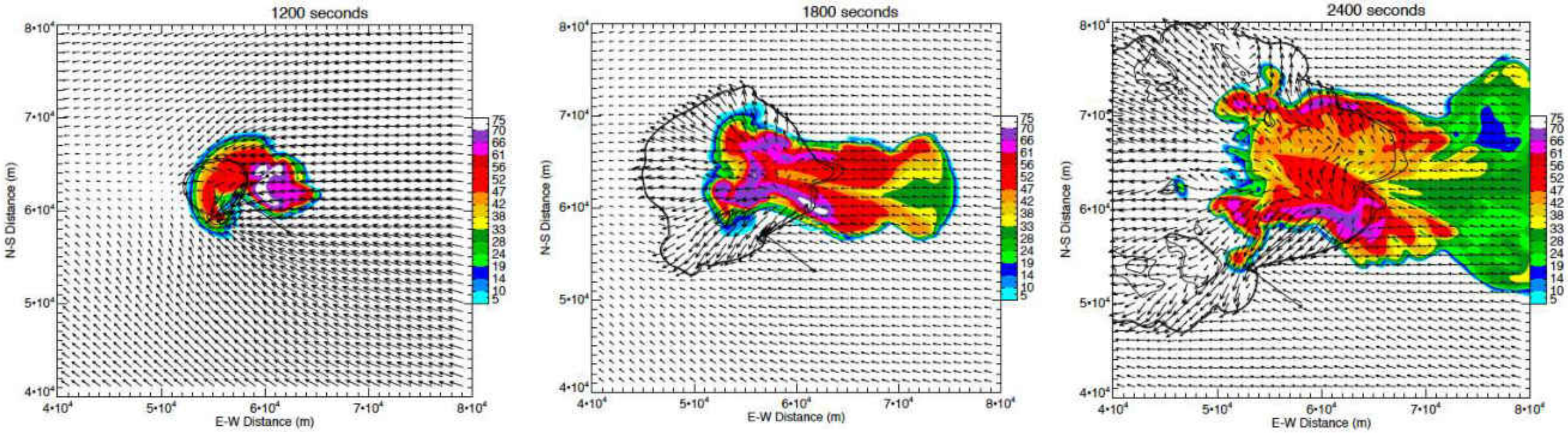

Fig. 25. Top showing a cross section of the simulated storm for the (top row) feature averaged HP supercell sounding and (bottom row) height average HP supercell sounding at dx=250 m grid spacing. Winds are shown at the surface with reflectivity plotted at the 2.5 km AGL. The outer black contour is the perturbation of -0.5° C.

Using the Morrison microphysics scheme did not solve the problem of the storm demise; in fact, the storm is actually weaker. Figure 26 shows similarities in the trends for maximum updraft helicity between the height and feature average LP supercell sounding cases and the maximum updraft helicity is only half as strong and occurs later in the simulation, lagging about 700 s, for the Morrison microphysics scheme (2005) with the feature average sounding compared to the LFO scheme. The maximum for the Morrison scheme lagged the LFO scheme maximum by 700 s. Both the feature and height average single moment microphysics maximum updraft helicity occurred at 1500 s, while the Morrison scheme maximum updraft helicity occurred at 2200 s. Although it survived longer and had a hook echo co-located with the gust front for a longer period (not shown), the supercell simulated using the Morrison scheme does not survive past 1 hour and thus it did not help in providing a long-lived storm to analyze.

There are slight differences in the maximum values of vertical vorticity between simulations using LFO and the feature average LP sounding, LFO and height average LP sounding, and Morrison microphysics with the feature average LP sounding (Fig. 26). The LFO LP feature average supercell peaks in maximum surface vertical vorticity at 0.1 s^{-1} near t=1500 s, decreases to 0.05 s^{-1} by 2000 s, and then rebounds to 0.1 s^{-1} by t=2500 s just before diminishing at all levels. The peak also occurs around the same time for the height average simulation. However, the LP feature average storm with the Morrison microphysics produced weaker maximum vertical vorticity at both the surface and z=1 km than both the feature and height average storms with LFO microphysics, but produced greater vertical vorticity at z=3 km.

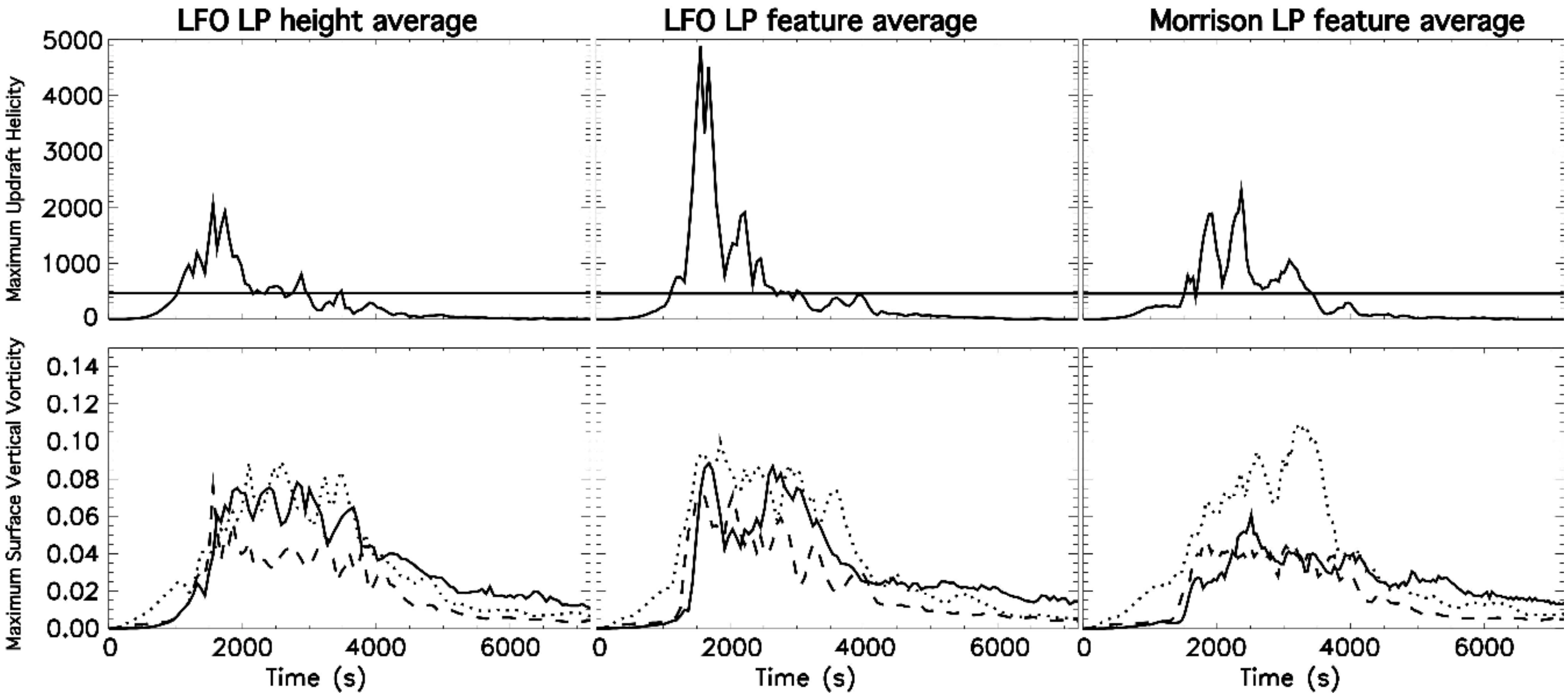

Fig. 26. Trends of (Top) maximum updraft helicity vs. time and (Bottom) maximum vertical vorticity vs. time for (Left) LP height average, (Middle) LP feature average, (Right) Morrison LP feature average simulations. In the bottom panels, the vorticity at surface shown as solid line, at 1 km shown as dashed line, at 3 km shown as dotted line.

Although trajectories have not been performed, this may be due to the weaker cold pool (less baroclinic generation of horizontal vorticity and less convergence amplification of vorticity along the gust front).

Figure 27 presents a similar analysis as was just shown for the LP average soundings. It shows that there are few differences between simulations using the LFO microphysics with the height average and feature average CL sounding separately simulated and the feature average CL simulated with the Morrison microphysics. There are slight differences in the maximum vertical vorticity in the CL height and feature average cases. The main difference for Fig. 27 is between the feature average sounding cases with two different microphysics schemes: the Morrison scheme produces a maximum vertical vorticity of 0.13 s^{-1} at 3 km occurring at 3500 s where as this occurs at 2500 s and similar magnitude with LFO. This could be due to the differences in the cold pool characteristics between the single and double moment microphysics. For the surface level, the height average LFO case has the highest maximum vertical vorticity at 0.1 s^{-1} but otherwise trends are similar for the three cases. The CL height average case maximum updraft helicity occurs sooner, at *t*=1500 s, during the simulation compared to the two CL feature average cases. For both microphysics schemes with the feature average sounding, the maximum updraft helicity occurs just after *t*=2000 s. It is interesting that the maximum updraft helicity, denoted as UH hereafter, is similar for the CL feature average Morrison scheme and the CL feature LFO scheme (Fig. 27), whereas the LP feature average Morrison scheme is much weaker than the LP feature average LFO scheme (Fig. 26).

Repeating the analysis for the HP sounding class, Fig. 28 shows subtle differences in the vertical vorticity among simulations. Similar to the CL sounding case, the height average sounding with LFO microphysics produced the largest maximum vertical vorticity at the surface at 0.11 s^{-1}. The feature average sounding with the LFO and Morrison microphysics produced very similar trends and maximum value with both near ~ 0.09 s^{-1}. The feature average single moment case has slight larger maximum vertical vorticity at 3 km compared to the double moment scheme. The LFO height and feature average cases have similar times when the maximum updraft helicity is reached, occurring just before 1500 s into the simulation. The Morrison feature average case reaches a maximum updraft helicity at 2000 s into the simulation.

The differences between the LFO height and feature average cases for LP, CL, and HP sounding classes is the maximum updraft helicity. The CL and HP height average LFO case has a larger updraft helicity compared to the CL and HP feature average LFO case. The LP feature average LFO case has a larger updraft helicity compared to the LP height average case and Morrison case. The Morrison feature average simulations have the updraft helicity maximum occurring later in the simulation at 2000 s in all three sounding classes.

Part of the updraft helicity computation is the vertical vorticity computation at any given altitude. The purpose of investigating the strength of the low-level vertical vorticity and comparing microphysics schemes is to determine the extent of the differences between the classifications for possible tornadogenesis. To what extent does the microphysics affect the amount of low-level vertical vorticity?

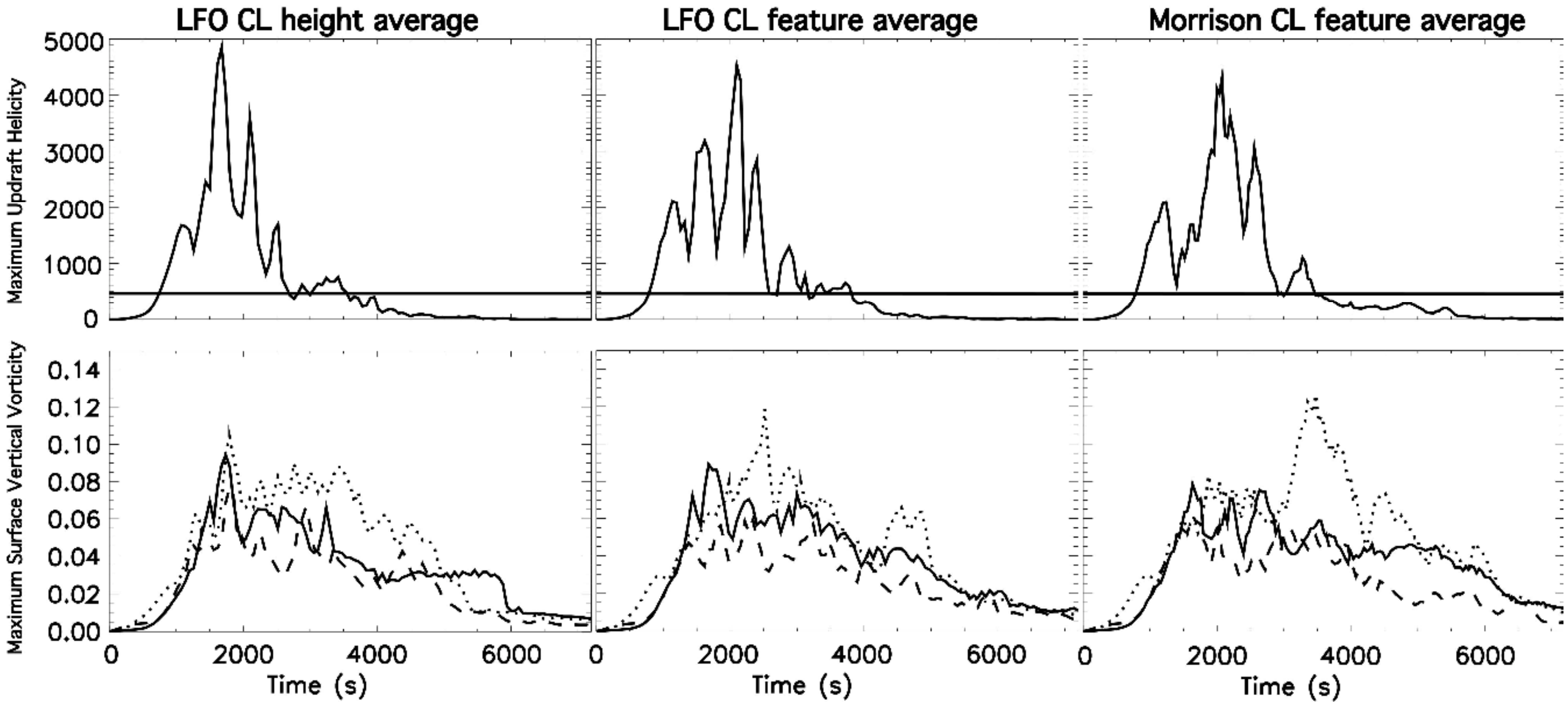

Fig. 27. Trends of (Top) maximum updraft helicity vs. time and (Bottom) maximum vertical vorticity vs. time for (Left) CL height average, (Middle) CL feature average, (Right) Morrison CL feature average simulations. In the bottom panels, the vorticity at surface shown as solid line, at 1 km shown as dashed line, at 3 km shown as dotted line.

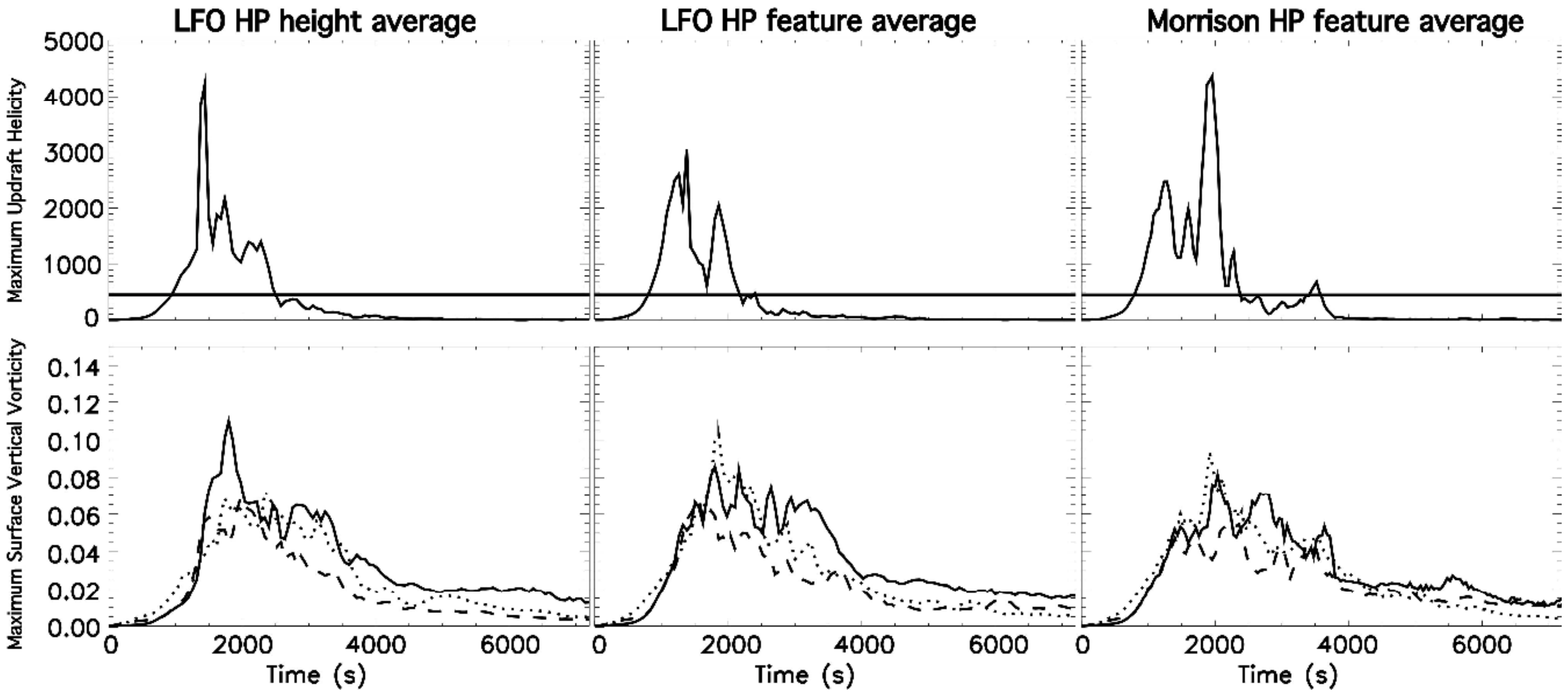

Fig. 28. Trends of (Top) maximum updraft helicity vs. time and (Bottom) maximum vertical vorticity vs. time for (Left) HP height average, (Middle) HP feature average, (Right) Morrison HP feature average simulations. In the bottom panels, the vorticity at surface shown as solid line, at 1 km shown as dashed line, at 3 km shown as dotted line.

If all three classifications have similar low-level vertical vorticity than more analysis would need to be performed in future work. Moller et al. (1994) stated that tornadoes are rare for HP and LP supercells. If all three have comparable low-level vertical vorticity what explains the difference in larger number of tornado occurrences for the CL supercell classification and not the LP and HP supercells? Finer grid spacing would be needed to investigate this further due to tornadogenesis processes occurring at spatial scales smaller than the 250 m grid spacing. This is a preliminary investigation.

Since the composite soundings made from every sounding in each class were unable to produce long-lived supercells in the model using LFO and Morrison microphysics, another strategy was needed. Thus, each individual sounding was simulated individually at 1 km horizontal grid spacing to determine if the sounding produced a supercell that lasted at least 7200 s (based upon updraft helicity threshold of 480 $m^2 s^{-2}$). If the individual sounding produced a storm that satisfied the conditions above, then the sounding was considered a “working case, hereafter denoted as WC”. A new feature and height average composite was created from the WC.

iii) Simulation of individual cases in each class

Individual plan view maps of radar reflectivity were inspected for every sounding considered herein case every 5 min to confirm supercell existence at 1 km horizontal grid spacing. For the three cases found to produce sustained supercells for the full 2 h in each class (hereafter defined as “working cases”), the sounding was then re-simulated at 250 m horizontal and vertical grid spacing for the same time interval.

Results from the 250 m grid spacing simulations will be discussed below starting with LP, then CL, and finishing with HP, with subsections labeled by the sounding name. Trends of maximum updraft helicity (UH) are shown in Fig. 29 with maximum values for the simulation shown in Table 4. Example reflectivity plots are shown for each case near *t*=5400 s.

Table. 4. Maximum updraft helicity for each case experienced during the simulation.

Case	Maximum updraft helicity $m^2 s^{-2}$
LP_KAMA27	4912
LP_KDDC0193	5620
LP_KOUN20	3291
LP Class Mean of Maximum UH	**4608**
CL_KAMA25	7469
CL_KOUN12	7237
CL_KOUN26	10653
CL Class Mean of Maximum UH	**8453**
HP_KAMA11	4645
HP_KOUN02	6129
HP_KOUN07	3709
HP Class Mean of Maximum UH	**4828**

The individual maximum UH during each of the CL sounding simulations, as well as the mean of all three maximum values, is larger for the CL soundings than for the LP and HP soundings (Table 4).) The time average value of UH appears to be largest for CL, followed by LP, and smallest for HP (Fig. 29). Some of the cases are cyclic in strength.

There has been discussion regarding the differences from the current study and Beatty et al. (2009) regarding the coordinate system used to determine the rear and forward flank precipitation mode. Beatty et al. (2009) uses radar derived estimated storm motion for the x-axis. The current study uses the 0.5 to 4 km shear vector as the x-axis, hereafter referred to as modified Beatty analysis. All of the following analysis will be in regards to the 0.5 to 4 km shear vector as the x-axis unless stated otherwise.

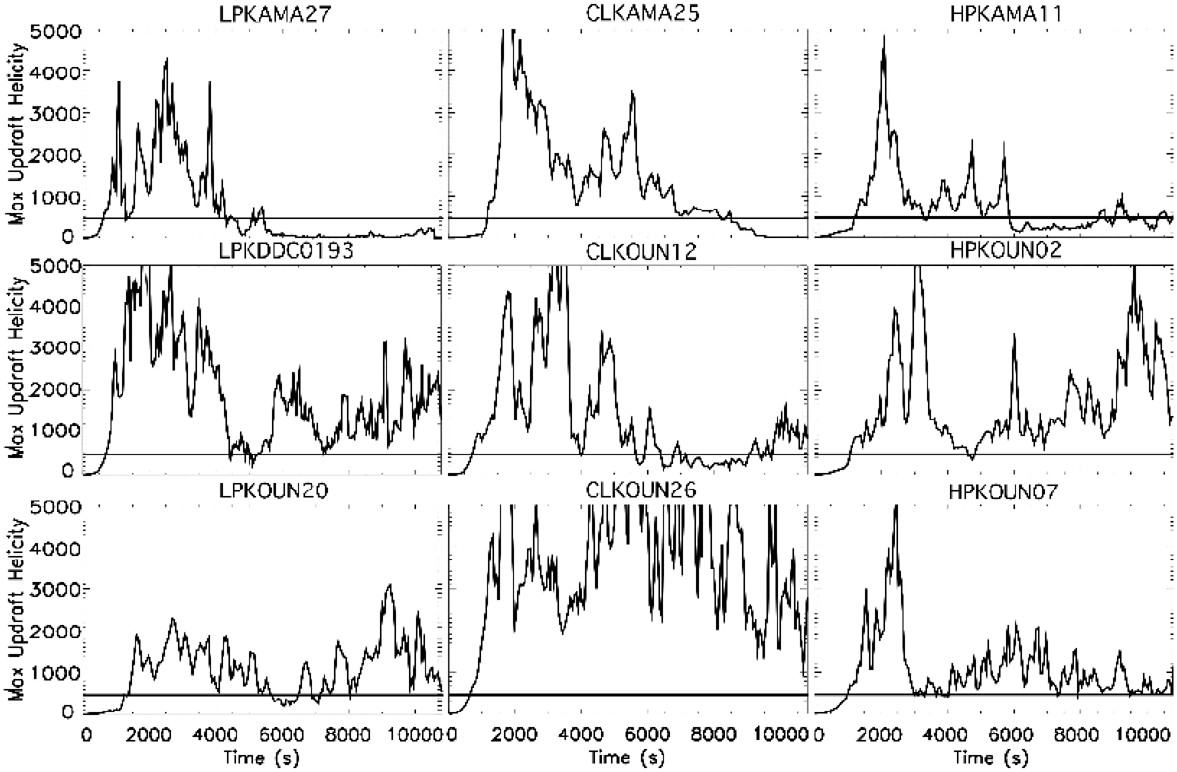

Fig. 29. (Left) LP working cases, (Middle) CL working cases, and (Right) HP working cases plots of maximum updraft helicity $m^2 s^{-2}$ with respect to time. Black horizontal indicates updraft helicity threshold for supercell detection.

iv) Simulations of individual LP sounding cases: Before listing details about each individual case, it is worth considering the differences and similarities. The important differences between the cases are as follows: supercells, as defined by UH, are first detected at slightly different times (900 s or 1200 s); some last the full 3 h while others only last up to 2 h; one LP sounding produces a storm that transitions to HP appearance (with strongest reflectivity in the rear; KOUN20) whereas the other ones do not. (A modified Beatty analysis plot will be shown below for the storm that transitioned.) This category had the following similarities: an apparent hook echo forming at 3000 s into the simulation (not shown) and a NE-SW reflectivity orientation of the strongest echo at t=5400 s (Fig. 30). Now that the similarities and differences have been summarized, the details of each individual storm case will now be described.

KAMA27: The storm is first detected as a supercell by the UH algorithm at 900 s (Fig. 29) and has classic supercell features determined by the reflectivity field starting at 2100 s. Larger reflectivity values exist from 2100 to 2400 s to the northeast of the updraft region (not shown) and by 3000 s into the simulation, the storm has a supercell appearance from a reflectivity standpoint (c.f. section 1 on the following supercell characteristics: prominent hook echo in reflectivity and maximum reflectivity to the forward flank of the maximum updraft helicity). By 3900 s, precipitation is location in and around the updraft region and the maximum reflectivity centroid is located to the forward flank of the updraft location (not shown). The storm keeps a similar shape and behavior (hook echo and forward flank maximum precipitation centroid) for the remainder of the simulation (Fig. 30a). The storm lasts until 7200 s into the simulation with the modified Beatty analysis representing an LP or forward flank storm.

KDDC0193: The storm is first detected as a supercell at 1200 s by the UH algorithm (Fig. 29) and obtains supercell features determined by the hook echo in the reflectivity field starting at 2100 s just prior to splitting at 2400 s (not shown). By 3000 s into the simulation there is a strong right moving supercell present, with the majority of the maximum reflectivity being north and slightly forward flank of the updraft region and maximum updraft helicity (not shown). The maximum reflectivity centroid alternates from rear flank to forward flank with respect to the updraft region from 3600 to 6000 s (not shown). At t=5400 s the maximum reflectivity is still north of the maximum updraft helicity, close to being either rear or forward flank precipitation dominant (Fig. 30). By t=7200 s the supercell is appears to be diminishing from the reflectivity maximum values not as large as previously (not shown). The supercell remains consistent with the maximum precipitation to the north of the updraft region alternating between forward and rear until 8700 s. After this point random convection is flowing in from the southern boundary and becomes difficult to analysis any further with confidence.

KOUN20: The first supercell detection occurs at 1500 s into the simulation (Fig. 29). The storm splitting process starts to occur at 2100 s. From 2400 – 4200 s the supercell reflectivity is forward-flank precipitation maximum with a distinct hook echo. The modified Beatty analysis shows the storm alternating from forward and rear flank maximum reflectivity centroid location with respect to the updraft.

After 4200 s there is not another supercell detection until 6600 s (Fig. 30c), by then the storm looks more HP and the reflectivity is aligned linear to the gust front. At 7800 s a more discrete supercell forms on the southern flank of the linear reflectivity feature (not shown). From 8100 s until the end of the simulation at 10800 s the storm has HP supercell characteristics from the Beatty analysis showing a maximum reflectivity centroid to the rear of the maximum updraft region (Fig. 31). Recall that RS98 stated that all supercells would trend toward HP structure with time. It is difficult to determine if this actually happened for this simulation due to no supercell detection from 4200 – 6600 s.

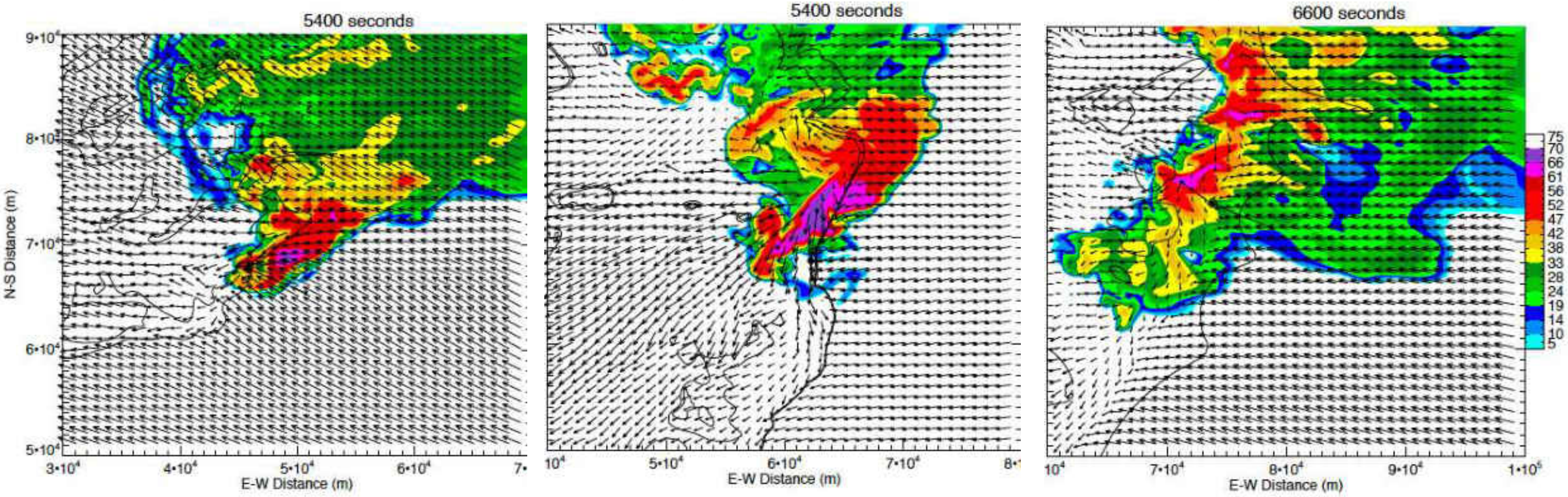
a) LP_KAMA27

b) LP_KDDC0193

c) LP_KOUN20

Fig. 30. Zoomed-in view of radar reflectivity for the simulations with 250 m grid spacing. Winds are shown at the surface denoted by the arrow vectors with reflectivity plotted at the 2.5 km AGL. The outer black contour is the perturbation of -0.5° C. The diamond indicates the maximum updraft helicity location, with one line segment and star showing the Bunkers predicted storm motion direction (to the east and southeast) and the second line segment with star showing where the maximum precipitation is located (to the northeast to northwest).

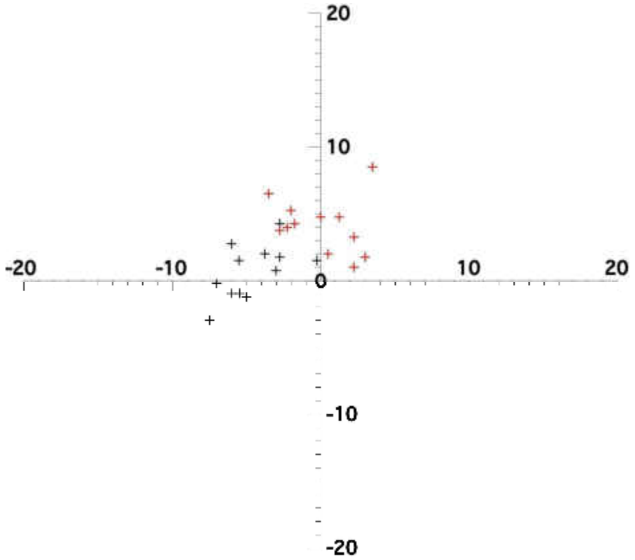

Fig. 31. Beatty et al. (2009)-like analysis from LPKOUN20 case using a sounding rotated so that the 0.5 to 4 km shear vector points along the x-axis. The red crosses represent when storm was a forward mode precipitation, black crosses indicate when storm transitioned to rear precipitation mode. The transition occurred at 8100 s of simulation time. This plot aligns the x-axis with the 500 m-4 km shear vector (and not the storm motion vector).

The forward-flank versus rear-flank precipitation behavior for this case is summarized in Fig. 31, which shows that the majority of the red crosses in the forward flank are at the beginning of the simulation 1500 – 7800 s, while the black cross indicate rear flank storm (HP) towards the end of the simulation 8100 – 10800 s. The rear flank precipitation detection became more consistent along with the radar reflectivity representing an HP supercell for the last 45 minutes of the simulation.

v) Simulations of individual CL sounding cases: This category had more differences than similarities among the simulated storms. Important differences between the cases are as follows: supercells are first detected at slightly different times (900 s or 1200 s); some supercells, as defined by UH, last the full simulation time while others only last up to 2 h; one supercell transitions from forward-flank precipitation dominant to rear-flank precipitation dominant (KOUN12). The three simulations in this category have the following similarities: an apparent hook echo forming by 2100 s and persistent thereafter. Now that the similarities and differences have been summarized, the details of each individual storm case will now be described.

KAMA25: The storm is first detected as a supercell at 1200 s. The storm has supercell radar characteristics with a prominent hook echo and forward flank precipitation maximum region starting at 2100 s into the simulation as the storm splitting process begins. The larger reflectivity values are located within a 10 km radius of the storm's updraft region. By 5400 s (Fig. 32a) the cold pool begins to outrun the updraft region and by 6600 s, the cold pool has out run the updraft location by several km (not shown). The last supercell detection is at 7200 s (not shown).

KOUN12: The storm is first detected as a supercell at 900 s. The storm has supercell characteristics starting around 2100 s into the simulation as the storm splitting process is taking place (not shown). A hook echo shaped reflectivity last until 5400 s (Fig. 32b). The cell loses supercelluar characteristics after 6900 s and falls below the supercell detection threshold (Fig. 29). By 9300 s the simulation has supercell detection and the storm takes on HP supercell characteristics because the majority of the heaviest precipitation is located in the rear flank of the storm with respect to the updraft. From 9300 – 10500 s the supercell has all maximum precipitation in the rear flank.

KOUN26: The storm is first detected as a supercell at 900 s. This is the most impressive looking supercell from a hook echo, classic supercell reflectivity standpoint. There is an apparent hook echo present for much of the simulation and it satisfies the UH detection of a supercell for the entire simulation (Fig. 29). The storm has supercell radar characteristics with a prominent hook echo and forward flank precipitation maximum region starting at 1500 s. The storm splitting process occurs around the 2100 s time. The persistent hook is visible from 1500 s until 6600 s. At 6900 s the storm appears to be transitioning to a rear flank precipitation dominant supercell due to the two consecutive rear flank hits. After 7200 s the simulation has random convection coming in from the outer boundaries to the end of the simulation, thus making it difficult to analysis with confidence. The reflectivity at 5400 seconds is shown above in Fig. 32c.

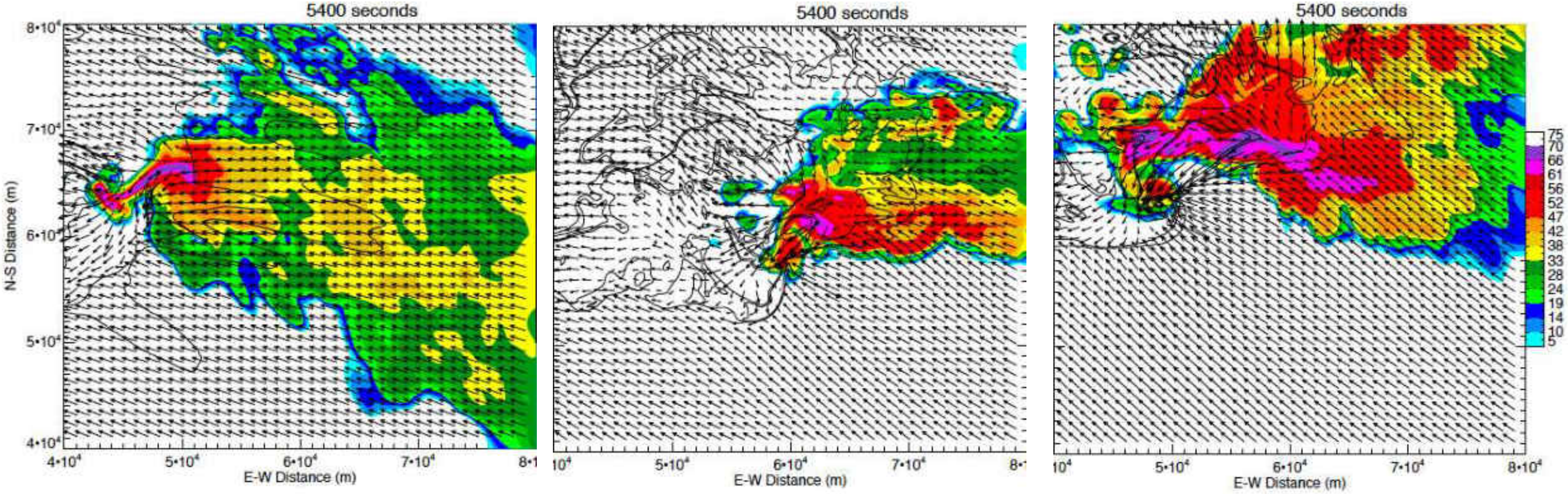
a) CL KAMA25

b) CL KOUN12

c) CL KOUN26

Fig. 32. Zoomed-in view of radar reflectivity for the simulations with 250 m grid spacing. Winds are shown at the surface denoted by the arrow vectors with reflectivity plotted at the 2.5 km AGL. The outer black contour is the perturbation of -0.5° C. The diamond indicates the maximum updraft helicity location, with one line segment and star showing the Bunkers predicted storm motion direction (to the east and southeast) and the second line segment with star showing where the maximum precipitation is located (to the northeast to northwest).

vi) Simulations of individual HP sounding cases: This category had more differences than similarities among storms. The three simulations in this category had the following differences: they are first detected as a supercell at slightly different times (900 s or 1200 s) as defined by UH. The KAMA11 sounding lasted the entire simulation with the reflectivity field representing more of a CL reflectivity shape (visible hook echo for the storm duration). The KOUN07 sounding produces a linear reflectivity mode towards the end of the simulation. The KOUN02 appears to represent a true HP supercell with the maximum reflectivity in the rear flank of the storm but only towards the end of the simulation. For similarities, all three cases have a hook echo early in the simulation, but it is short lived. Now that the similarities and differences have been summarized, the details of each individual storm case will now be described.

KAMA11: The storm is first detected as a supercell at 1500 s. By 2100 s into the simulation the storm splitting process is starting to occur. The storm is producing high reflectivity values to the rear of the storm, but the maximum reflectivity values are still in the forward flank of the storm ahead of the updraft region. This is consistent from 2100 – 2700 s. At 3000 s the maximum reflectivity is located in the rear of the storm. This is short lived with the maximum reflectivity being primarily forward flank for the remainder of the simulation. The reflectivity at 5400 s will be shown in Fig. 33a.

KOUN07: The storm is first detected as a supercell at 1200 s. For this case the Bunker's storm motion direction is much different compared to the other HP and LP/CL supercell cases. The storm motion is predicted to be 15.3 m s^{-1} at 163° and indeed, the storm does move to the SSE. The storm split does not start to occur until 3600 s. By 4500 s there is a boundary setting up at the leading edge of the cold pool with southerly inflow. Reflectivity continues to grow along this boundary at 5400 s creating a long linear reflectivity feature (Fig. 33b). This case produces two storms with large reflectivity coverage spatially with the maximum updraft helicity alternating between the two storms. By 5700 s the right mover is slightly stronger producing high reflectivity values along the aforementioned boundary interaction with the remaining maximum updraft helicity associated with the right mover. This boundary stays consistent through the simulation producing high reflectivity values along this boundary. It would be hard to conclude that this case produced a discrete HP supercell; rather the case appears to produce a linear line of strong convection along the boundary that formed during the simulation.

KOUN02: The storm is first detected as a supercell at 1200 s (Fig. 29). The storm splitting process begins at 2100 s into the simulation. By 3000 s there is a dominant right moving supercell with a distinct hook echo in the reflectivity field. It is hard to determine what type of supercell it would be based solely from the reflectivity field. Following the modified Beatty analysis, it would initially be considered a forward flank mode supercell, since the maximum reflectivity centroid is to the right of the updraft region (red crosses in Fig. 34).

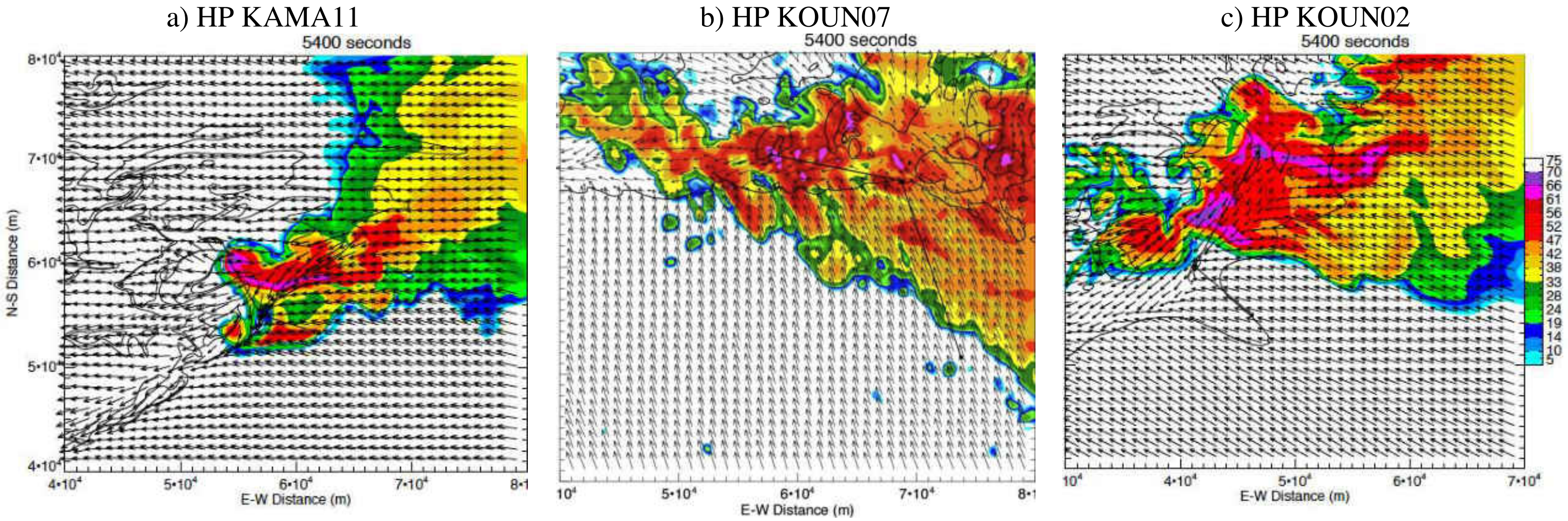
a) HP KAMA11
b) HP KOUN07
c) HP KOUN02

Fig. 33. Zoomed-in view of radar reflectivity for the simulations with 250 m grid spacing. Winds are shown at the surface denoted by the arrow vectors with reflectivity plotted at the 2.5 km AGL. The outer black contour is the perturbation of -0.5° C. The diamond indicates the maximum updraft helicity location, with one line segment and star showing the Bunkers predicted storm motion direction (to the east and southeast) and the second line segment with star showing where the maximum precipitation is located (to the northeast to northwest).

By 4200 s the reflectivity field appears HP due to the lima bean type shape (Moller et al. 1990) from section 1. At 4500 s the storm's highest reflectivity values are to the north of the updraft alternating between the forward and rear flank. At 5400 s the storm is starting to form an elongated reflectivity shape (Fig. 33c). This elongated shape stays consistent through 8400 s. At 8700 s there is still the elongated reflectivity but the maximum reflectivity is to the rear of the updraft region. For the last 35 minutes of the simulation, the storm's maximum precipitation was in the rear flank (black crosses in Fig. 34).

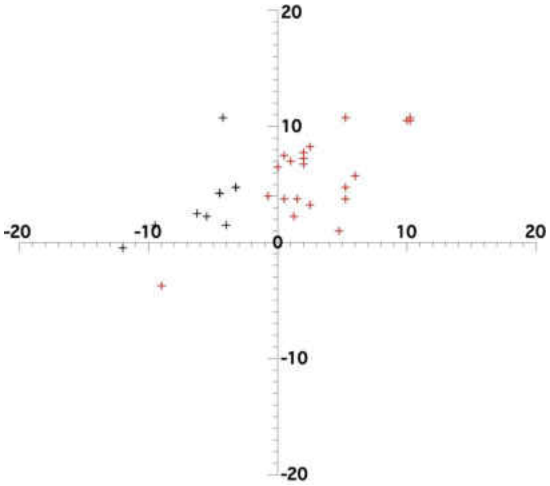

Fig. 34. Beatty et al. (2009)-like analysis from HPKOUN02 case using a sounding rotated so that the 0.5 to 4 km shear vector points along the x-axis. The red crosses represent when storm was a forward mode precipitation, black crosses indicate when storm transitioned to rear precipitation mode. The transition occurred at 8700 s of simulation time. This plot aligns the x-axis with the 500 m-4 km shear vector (and not the storm motion vector).

vii) Sensitivity of the Beatty analysis to the choice of coordinate system

The following analysis compares the simulations herein with the Beatty et al. (2009) radar results to distinguish a forward vs. rear precipitation mode for classifying supercell thunderstorms. There are slight differences between studies. The current study uses LP/CL/HP soundings simulated in CM1 producing simulated radar images, while the Beatty et al. (2009) study used storms depicted by actual radar. The Beatty method uses the radar-observed storm motion to determine the x-axis for separating forward from rear flank precipitation maxima. The current study herein can investigate the use of the storm motion as well as using a different method (such as 0.5 to 4 km shear vector as the x-axis). For both cases, the updraft location and distance to the maximum reflectivity centroid was determined. These were known precisely in the current study whereas the updraft location was inferred in Beatty et al. (2009).

The purpose herein is two fold. First, it is desirable to understand if the result is sensitive to the choice of x-axis in the Beatty analysis. If so, then it is desirable to determine if the model is able to capture this forward and rear flank precipitation mode between classes based upon the soundings used. If the model is able to determine the mode, then further analysis of the model behavior could give the community a better understanding how each classification and environment differs. The following, Fig. 35, shows the Beatty et al. (2009) method of determining LP/CL/HP supercells as forward and rear flank, along with two difference approaches to how and determine what is forward and rear flank. As discussed in section 2 there are issues with Beatty's methodology that arise from the x-axis being orientated with the storm motion vector. The storm motion vector is not Galilean invariant, meaning if two hodographs represent the same shear magnitude throughout each layer but only differ by a constant translation on a hodograph, the storm will be identical except for the motion vector, (refer to Figs. 11 and 12). Thus, this changes the orientation of the x and y-axis that depicts whether the storm is a forward or rear flank storm. By rotating the points to have the x-axis represent the storm motion, following Beatty, the proportion of forward and rear reflectivity detections change (Fig. 35). By having the x-axis represent the storm motion, this increases the rear flank hits in the HP cases by 19%, going from 18 hits in the non-rotated plot to 29 hits for the rotated case. This is largely due to HP storms having highly deviate storm motion angles to the right of the mean flow. There were no significant changes in the position of the LP/CL cases for either version since the storm motion vector is more similar to the 0-0.5 to 4 km shear vector in those cases.

One cannot say that one version is better than another. The x-axis alignment with the 0.5 km to 4 km shear vector (Fig. 35, left) is somewhat arbitrary and another vector could have been chosen. It is unclear how the results might have changed with a different shear vector choice.

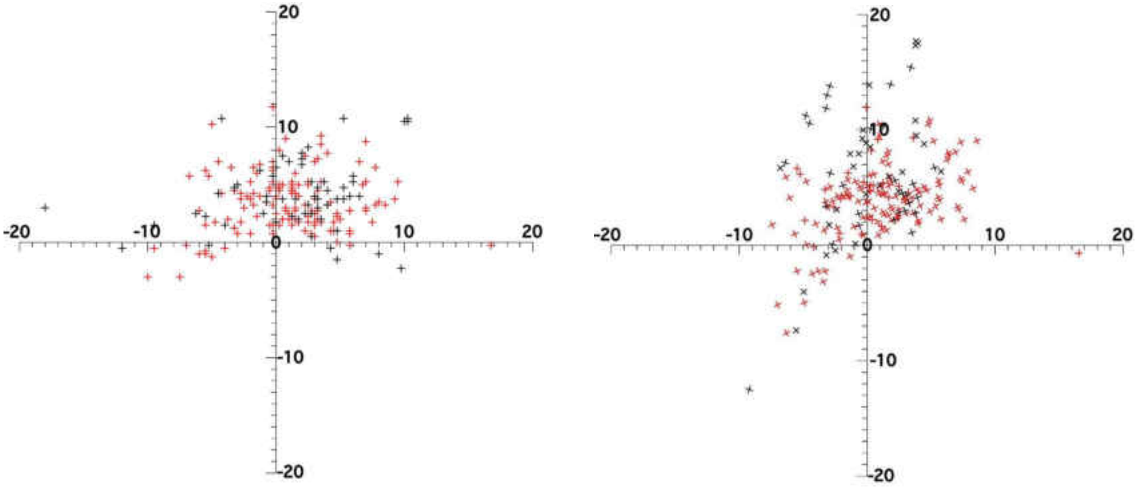

Fig. 35. Beatty analysis of the precipitation location with respect to the updraft every 5 minutes for each of the three working cases in each class (LP/CL/HP) for the feature average soundings. Updraft relative to the maximum rain rate centroid locations for all three cases, red crosses are for LP/CL and HP black crosses. (Left) is where the x-axis is represented by the 0.5-4 km shear vector, (Right) Points have been rotated so that the x-axis is aligned with the Bunkers predicted storm motion vector in each case.

e) Re-simulation of LP/CL/HP feature and height average from only successful cases

The composite feature and height averages were redone with only the working cases, referred to as "revised" hereafter, determined by the following criteria: last at least

7200 s and has an updraft helicity strength of 480 $m^2 s^{-2}$ determined from Naylor et al. (2012). This was done to determine if the new composite storm represents what an average LP/CL/HP storm would be from a radar reflectivity standpoint. The new composites are from the cases denoted in Table 5. There are three working cases from each category.

Table 5. Composite feature and height average soundings based off of the working cases showing sounding parameters of ML*CAPE, MLCIN, MLLCL, MLLFC, and PW*.

	CAPE	CIN	LCL (m)	LFC (m)	PW (in.)
LP Feature Avg. WC	2286	56	1052	2044	1.419
LP Height Avg. WC	2645	32	1111	1596	1.333
CL Feature Avg. WC	2813	13	880	1277	1.531
CL Height Avg. WC	2443	16	950	1435	1.191
HP Feature Avg. WC	2272	96	1047	2232	1.624
HP Height Avg. WC	2536	43	973	1883	1.414

Table 5 shows that the height average composite has larger CAPE than the feature average composites for the LP and HP categories. This is opposite what was originally found when all soundings were included in the compositing. However, the CL case is consistent with the previous averaging whereby the feature average case has more CAPE than the height average. One of the HP soundings did not have an inversion and thus could not participate in the feature averaging at that level. The two other HP soundings had very large CIN values indicative of a strong inversion. If the two soundings have strong inversions, then the feature average composite will preserve these features. The height average composite smoothed the sounding where the capping inversion was much less compared to the feature average. The revised LP feature average composite, when simulated in the model, dies due to the cold pool propagating past the location of the maximum updraft helicity region. The revised LP height average composite also dies but last slightly longer compared to the feature average composite perhaps due to larger CAPE and less CIN. The LP environment also lacked low-level shear and 0-3 km Strom Relative Environmental Helicity (SREH) meaning that the dynamic updraft forcing was lacking (e.g., Weisman and Klemp 1984) thereby not helping supercell sustenance. The run statistics comparing the original composites to the revised composites can be found in Table 6.

Table 6. Simulation statistics on how long each supercell lasted from each type of composite sounding. WC denotes that the sounding composite was derived from the three cases that within each class. The regular "feature average" and "height average" was derived from all soundings within a class.

	Feature Average (s)	Height Average (s)	Feature Average WC (s)	Height Average WC (s)
LP	3000	2400	3900	6000
CL	3600	3300	10800	10800
HP	2400	2400	3900	10800

One can immediately see that by using only the working cases in the averaging, the result is longer-lived supercells than if every sounding was used in the averaging. Fig. 36 will show corresponding reflectivity plots for the revised composites. The composite CL feature and height average composites are both produce long-lived supercell simulations (Table 6) and appear to produce "average" CL supercell updrafts from the three working cases (Fig. 36). Both the LP and HP height average composite supercells outlast their respective feature average composite, (Table 6; columns 3 and 4) likely due to the weaker capping inversions in the case of height averaging. The maximum updraft dies for the feature and height average LP composite while the individual cases last longer in the simulation (Fig. 36; top). The CL composite feature and height average soundings both produce an average maximum updraft velocity compared to the other two cases (Fig. 36; middle). The HP feature average case has similar trend at the beginning of the simulation but dies (Fig. 36; bottom), likely due to high CIN values, while the height average composite produces a storm that appears to have roughly the average storm updraft from the three cases (Fig. 36).

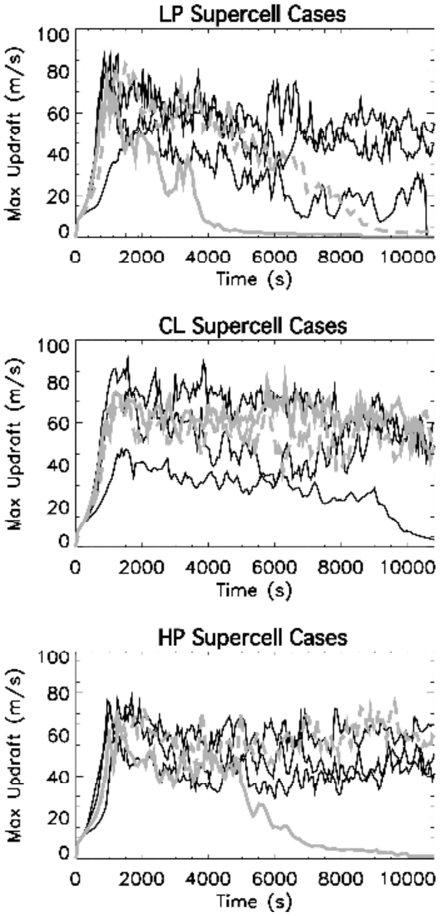

Fig. 36. Maximum updraft velocity with respect to time in the simulation, (top) LP, (middle) CL, (bottom) HP with the solid black lines denoting the three individual case trends, thick solid gray line denoting the feature average case, and the thick dashed gray line denoting height average case. These are the composite soundings from the working cases.

The compositing technique does not always produce a storm with average storm characteristics based off of the run statistics from the individual cases for that particular class. The next section will discuss how varying the upper level winds and keeping a constant thermodynamic profile will affect the storm precipitation morphology (LP/CL/HP).

The time of t=3900 s (Fig. 37) was chosen to display the reflectivity for commonality purposes due to the feature average LP and HP composites not lasting longer than this time. For the LP feature and height average composites the reflectivities have a NE to SW orientation. The LP height average composite shows a much stronger right mover and larger reflectivity values (Fig. 37, bottom left) compared to the feature average composite storm, which is dissipating (Fig. 37, top left). Neither composite produces a long-lived supercell, but the LP height average composite last longer in the simulation (not shown). The CL feature and height average composites show similar orientation of the anvil location of the reflectivity being due E for both cases. Both cases are showing similar strength for the reflectivity values. The height average composite has a much stronger left mover at this time (Fig. 37, bottom middle). The feature average composite is showing a much stronger right moving supercell (Fig. 37, top middle) compared to the height average composite. This is determined by the maximum updraft helicity location. Both composites produce a long-lived supercell (not shown). For the HP feature and height average composites the reflectivity has an ESE to WNW orientation associated with them. The HP height average composite has larger reflectivity values (Fig. 37, bottom right) compared to the HP feature average composite, which is dissipating (Fig. 37, top right). At the current time the HP height average is showing a strong left mover (Fig. 37, bottom right).

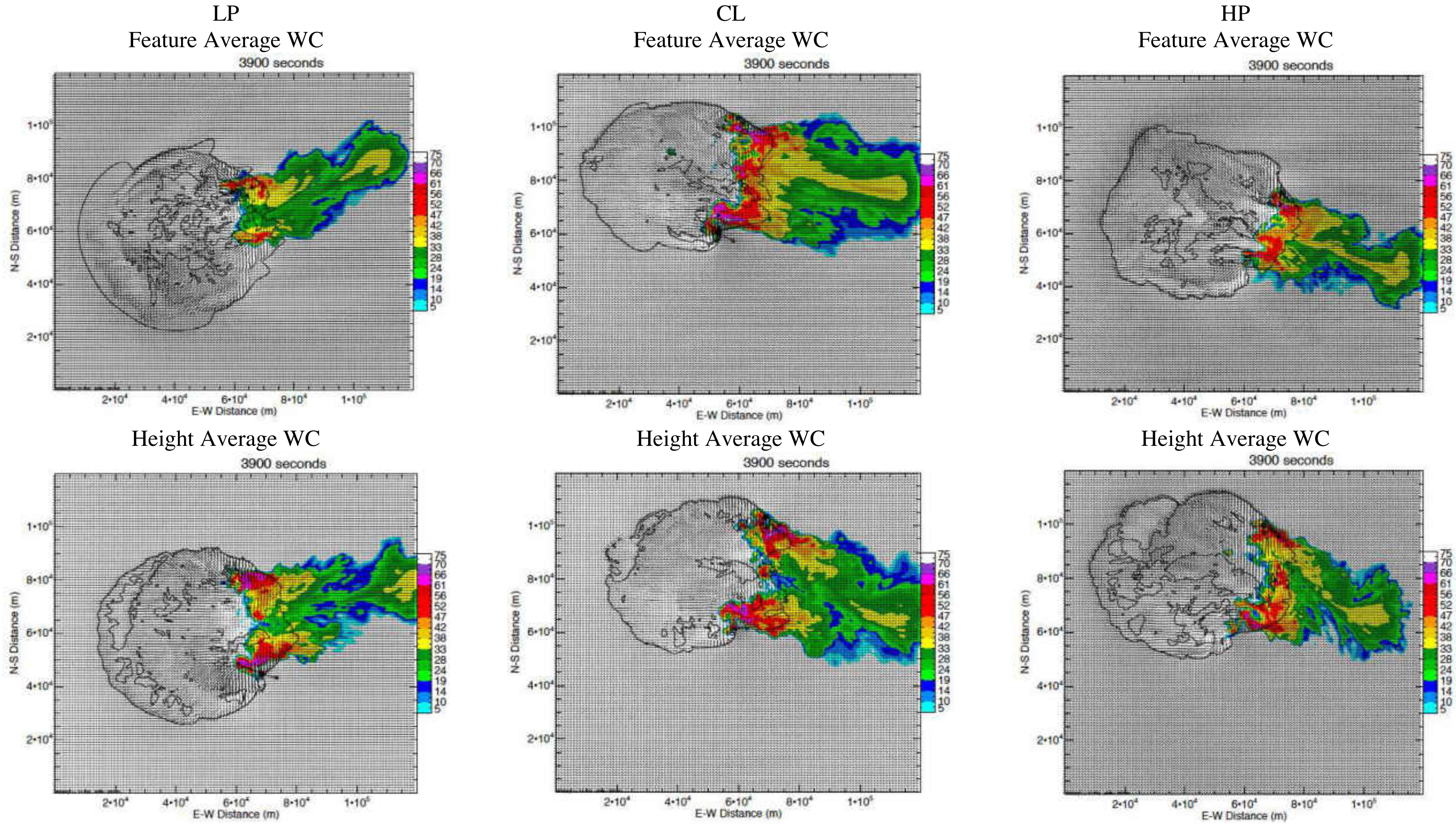

Fig. 37. Full domain 120 km by 120 km showing radar reflectivity for the working case composite simulations with 250 m grid spacing. Winds are shown at the surface denoted by the arrow vectors with reflectivity plotted at the 2.5 km AGL. The outer black contour is the perturbation of -0.5°. The diamond indicates the maximum updraft helicity location, with one line segment and star showing the Bunkers predicted storm motion direction (to the east and southeast) and the second line segment with star showing where the maximum precipitation is located (to the northeast to northwest).

Later in the simulation the HP height average produces a long-lived right moving supercell (not shown). It appears to be consistent, regardless of which averaging technique is used that the reflectivity orientation goes from NE to SW for LP, due E for CL, and ESE to WNW for HP. The following (Fig. 38) will show the modified Beatty analysis for the feature and height average composites from the working cases.

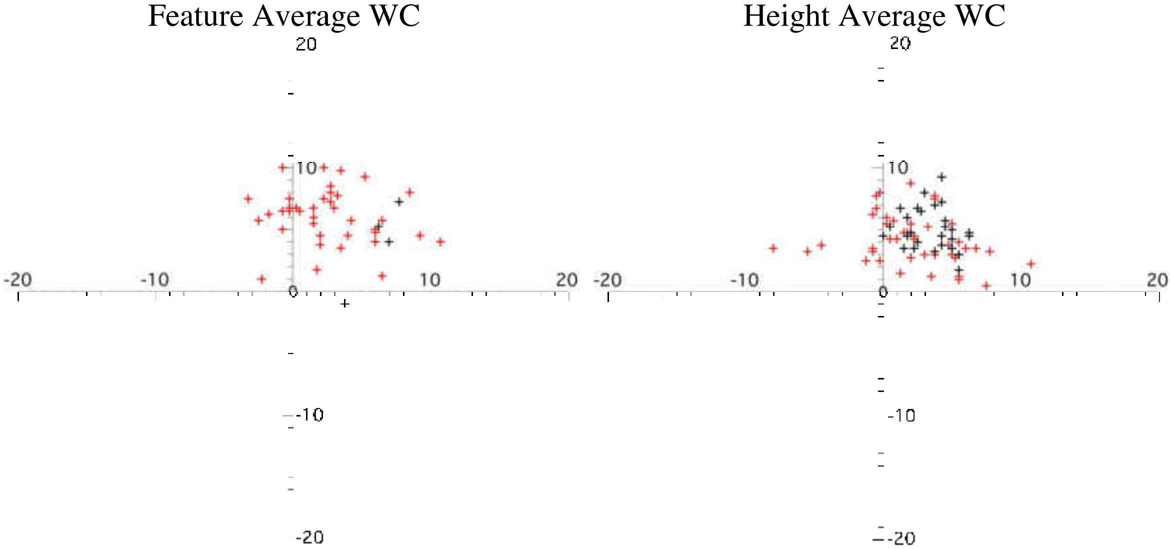

Feature Average WC

Height Average WC

Fig. 38 (Left) Feature average composites from the working cases. The red + indicate LP/CL composite and the black + indicate HP composite. (Right) Height average composites with same color scheme. The 0 indicates updraft location with + indicating where the precipitation maximum is located with respect to the updraft. The grid is in units of km.

From the modified Beatty analysis it is clear that the LP/CL supercell composites (Fig. 38, red +) for either the feature or height average technique will produce a forward flank precipitation mode, consistent with Beatty et al. (2009). The HP supercell feature and height average composites fail to represent a rear flank precipitation mode. The HP composite does not show a transition to the rear flank precipitation mode either. The HP height average composite lasts much longer than the feature average composite, yet all of the maximum precipitation locations are to the forward flank of the updraft location.

Are the three cases that were averaged for the HP composite sounding really representative of an HP environment? There is one sounding that did transition to an HP supercell towards the end of the simulation (rear precipitation mode). The other two soundings did not show this behavior, which can explain why there is not a rear flank precipitation mode for the HP composite due to the averaging process of the three soundings.

f) CL thermodynamics LP/HP winds

RS98 proposed that one of the main differences across the precipitation mode spectrum is the storm relative upper level wind. Therefore, to test this sensitivity, the upper-level winds from the HP and LP feature average composites of the working cases were merged with the feature average classic thermodynamic profile; it was found to have the most CAPE and least CIN among all of the working cases (Table 5) and produced consistently strong updrafts (Fig. 39). The CL wind profile below 2 km was also used in an effort to provide similar dynamic forcing among all cases (Weisman and Klemp 1984). Figure 39 shows similar updraft strength, however, the updraft helicity differs. By having the same thermodynamic profile and 0-2 km winds, the importance of the mid to upper level storm relative winds on supercell structure can be determined. From Fig. 39 the three cases have very similar maximum updraft values, which might be expected, due to the identical thermodynamic profiles, however, the updraft is partially based upon dynamical forcing as well. The main difference from Fig. 39 is the maximum updraft helicity; with the HP and CL wind profiles having larger updraft helicity values compared to the LP wind profile case.

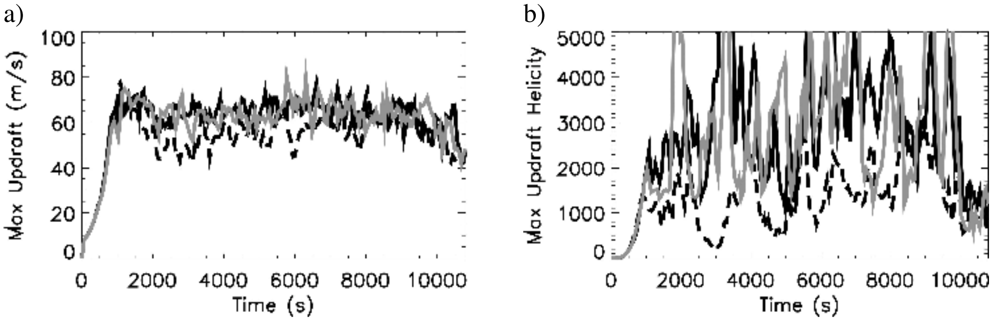

Fig. 39. (a) Maximum updraft velocity with respect to time with the solid black line indicating CL thermodynamics with HP 2-10 km winds and dashed black line indicating CL thermodynamics with LP 2-10 km winds and CL thermodynamics and wind profile in gray. (b) Maximum updraft helicity with respect to time with the same color and line style scheme in (a).

Thus, this means that despite best efforts to make these cases as similar as possible, the mid to upper level winds influence the updraft helicity strength. The CL thermodynamics merged with the HP winds produces a long-lived supercell but fails to produce an HP type supercell with lima bean shape in the reflectivity. The modified Beatty analysis fails to show rear flank maximum reflectivity centroid locations (not shown). It would be expected towards the end of the simulation to have all rear flank maximum reflectivity and that does not happen in this simulation. The simulation depicts more of a CL supercell signature determined from the reflectivity (Fig. 40b).

The CL thermodynamics merged with the LP winds also produces a long-lived supercell but the modified Beatty analysis alternates between a forward and rear flank precipitation maximum location during the simulation (not shown). The LP winds case does show less precipitation spatially distributed compared to the HP winds case at t=7200 s (Fig. 40a, b) and this is consistent throughout the simulation (not shown). The orientation of the reflectivity in the LP winds case is what would be expected with the reflectivity having an orientation to the NE of the updraft region, due to the upper-level winds associated with the composite (Fig. 40a).

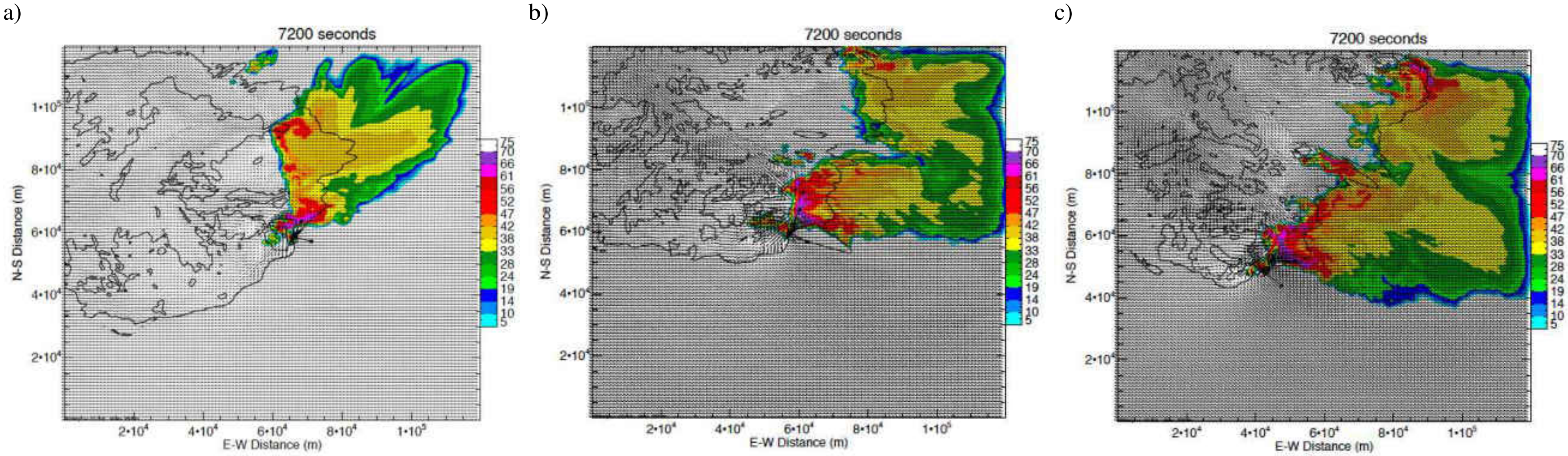

Fig. 40. Full domain 120 km by 120 km showing radar reflectivity for the working case composite simulations with 250 m grid spacing. Winds are shown at the surface denoted by the arrow vectors with reflectivity plotted at the 2.5 km AGL. The outer black contour is the perturbation of -0.5°. The diamond indicates the maximum updraft helicity location, with one line segment and star showing the Bunkers predicted storm motion direction (to the east and southeast) and the second line segment with star showing where the maximum precipitation is located (to the northeast to northwest). a) CL thermodynamics with LP winds and b) CL thermodynamics and winds and c) CL thermodynamics with HP winds.

The reflectivity images for the LP individual cases, revised LP feature and height average composites, and CL thermodynamic paired with 2-10 km LP winds are very similar and consistent with the reflectivity orientation being to the NE to SW. There is one LP sounding that transitioned to a rear flank precipitation mode supercell. That is the only transition seen for the LP individual cases, composites, and merged sounding.

The reflectivity images for the CL individual cases and revised CL feature and height average composites are similar and consistent in the behavior of the reflectivity orientation being to the E. The CL individual soundings and feature and height average all had a persistent hook echo present for the majority of the simulation. The CL individual cases and composites did not transition to a rear flank precipitation mode supercell.

The reflectivity images for the HP individual cases, revised HP feature and height average composites, and CL thermodynamics paired with the 2-10 km HP winds are not similar in reflectivity across the three type of simulations. The HP individual cases have one case with NE to SW reflectivity orientation, one with ESE to WNW reflectivity orientation, and one with E to W reflectivity orientation. The HP feature and height average composite reflectivity is similar to the CL thermodynamics paired with the 2-10 km HP winds having an orientation ESE to WNW. There is one HP sounding that transition to a rear flank precipitation mode supercell. That is the only transition seen for the HP individual cases, composites, and merged sounding. Therefore, the results seem to suggest that the upper level winds alone do not control the precipitation mode.

CHAPTER IV

CONCLUSION

There are two main components to this study. The first half of this study explores, from an observational standpoint, different ways of producing composite soundings, why those composites differ from one another, how the compositing technique itself affects the resulting thermodynamic and wind parameters, and which technique results in preserving features. The groups of soundings that were composited were collected in close proximity to supercell storms in three sub categories: low-precipitation (LP), classic (CL), and high precipitation (HP). The soundings came from Rasmussen and Straka 1998 (RS98) and Beatty et al. (2009). The second half of this study attempts to reproduce previously-reported LP, CL, and HP supercell behavior, as revealed by radar (through the technique of Beatty et al. 2009), from the both the original proximity soundings as well as the composite soundings in an idealized three-dimensional cloud model.

a) Observational

The feature average compositing technique resulted in soundings that, in theory, more accurately capture the capping inversion that is present in the majority of the cases. It also preserves more moisture in the boundary layer (BL), which is extremely important for CAPE and CIN calculations. In contrast, height averaging has a smoothing effect whereby, in most cases, the mean moisture content is reduced in the BL and the capping inversion is smoothed. It was also determined that averaging *RH* for the LP and CL feature and height average soundings would produce the largest CAPE values and least amount of CIN (perhaps beneficial for modeling work), but that averaging water vapor mixing ratio, q_v, is arguably the most accurate and appropriate. Only in the HP composite soundings does averaging vapor pressure, e, produce the largest CAPE and least amount of CIN, with *RH*-averaging producing slightly smaller values.

Comparisons between wind profiles and wind parameters are similar between soundings groups regardless of whether using the feature or height averaging technique compared to the large differences in thermodynamic parameters like moisture. Unlike the thermodynamic parameters, feature average wind parameters are mostly larger than height average wind parameters except LP BL-9 km shear and LP 4-10 km shear where the feature and height average values are equal.

In agreement with RS98, there are statistically different means ($p < 0.05$) between the HP soundings and LP and CL soundings for the BL to 9 km shear and the 4-10 km shear magnitude, also, significant ($p < 0.02$) is the 9-10 km storm relative wind for the HP soundings compared to the LP and CL soundings. In contrast, RS98 found the mean BL-9 km and 4-10 km shear magnitudes for LP and HP supercells were different at a significance level of 0.02. Regarding surface based parcel calculations; CL SBLFC has differences at a significance level of 0.05 relative to the two other supercell classifications, while RS98 found differences in the means at a significance level of 0.05 for both CL SBCAPE and LP SBLFC comparing to the other supercell classifications. RS98 also found differences in the means at a significance level of 0.02 for HP PW, LP SBCAPE, CL SBLFC, and HP SBLFC. The results should not necessarily be expected to agree between the studies due to RS98's alternation of the surface data in their soundings and the large sensitivity of surface-parcel-based parameters to that altered surface data. The current study presents a reanalysis of the means tests based upon lowest-100mb-layer parcels, as those results would be less sensitive to the surface conditions. There are three thermodynamic parameters that have means that are statistically significant with a *p*-value 0.05: LP MLLCL, LP MLLFC, and HP MLLFC.

Furthermore, while CAPE, CIN, LFC, and LCL parameters (Fig. 17) and wind parameters (Fig. 13) for both the feature and height average techniques are always within one standard deviation of the distribution mean, the feature average values are not consistently closer. Also, the difference from the distribution mean gets larger for parameters computed using mixed-layer parcels instead of surface based parcels. For example, in Fig. 17 the MLCAPE feature and height average values are overall further from the distribution mean (not as close to each other) as the corresponding feature and height average values for SBCAPE. So, while the feature average technique preserves capping inversions and low level moisture better, the technique is sensitive to which moisture variable is averaged and parameters from the feature average sounding do not consistently reside closer to the distribution mean.

Differences in height average soundings, hodographs, surface-based parcel parameters, and wind parameters between the current study and the RS98 study are likely attributed to two factors: 1) only RS98 replaced the sounding surface data with closer-to-storm surface station observations; and 2) the set of sounding cases differ slightly. In addition, it is not clear that RS98 tested the parameter distributions for normality and normalized them prior to means testing. The study herein appropriately tested the distributions and some were found to be non-normal requiring transformation.

The following section provides discussion as to why many feature and height average soundings failed to produce long-lived supercells.

b) Model-based

As mentioned previously, the goal of the modeling portion of this study was to use the original proximity soundings as well as the composite soundings to run simulations with an idealized three-dimensional cloud model and then process the model output using a radar-based method developed by Beatty et al. (2009) to semi-objectively determine storm precipitation type (forward flank or rear flank). Initially, the class composites included *all* available soundings. Because many of the original soundings, as well as original feature and height average composites, did not produce long-lived supercells in the model, compositing was done again using only the cases that produced sustained supercells. From the dataset, 29 individual sounding cases were simulated--10 CL, 10 LP, and 9 HP supercells-- but only three were deemed successful from each class (lasting at least 7200 seconds with an updraft helicity greater than 480 m^2 s^{-2}). It was hypothesized that the most likely reason that the original composite soundings did not produce sustained supercells is because most of the individual cases did not either. When only the individual successful working cases were used in the compositing procedure, this resulted in a composite sounding that provided a longer-lived supercell in every class. In particular, the new composite CL feature and height average soundings successfully produced long-lived supercells, like the CL individual cases. However, some of the LP and HP composite sounding cases were less reliable at producing long-lived storms compared to the individual soundings. Three LP and three HP individual cases produced long-lived supercells, albeit weaker than the CL ones. For the working cases, neither of the LP supercell composite storms last 7200 s, with the height average composite producing a longer-lived supercell compared to the feature average composite. The CL feature and height average composites both last the entire simulation (10800 s). The HP height average composite produces a supercell that lasts throughout the entire simulation (10800 s), while the feature average composite dies early in the simulation. The inconsistency from the working case composites is probably due to the small sample size for each classification. Ironically, the HP feature average sounding with weaker CIN is shorter lived than the individual HP soundings that have larger CIN. This raises the question as to why this occurs and is discussed further below (future work).

The modified Beatty analysis is the analysis method used to classify the supercell precipitation mode. Recall that to be forward or rear flank precipitation mode dominant, the storm needs to have clearly forward or rearward maximum precipitation locations with respect to the updraft. The analysis indicated forward flank precipitation mode supercells for the majority of the working LP and CL supercell soundings, as well as the composite LP/CL soundings produced from the working soundings. This is consistent with the Beatty et al. (2009) findings that were based upon use of the storm motion vector to determine forward and rear flank precipitation modes. One original LP sounding and one original HP sounding switched modes from forward flank to rear flank near the end of their simulations. The LP feature and height average composite simulations, and the HP feature average sounding simulation, did not last long enough in the model to determine whether a switch in precipitation mode would have occurred. Furthermore, the HP height average composite provided a forward flank precipitation mode, which is not consistent with the observations from Beatty et al. (2009). There was some subjectivity in the Beatty et al. (2009) study regarding the visual and radar classifications. Also, unlike RS98, there was no mention of an LP supercell transitioning to an HP supercell. There were explicitly classified as LP, CL, or HP in the study. The study gives specific times of when the storms were observed visually and/or with radars to determine the supercell storm mode. Once the storm was classified as LP/CL/HP, the radar updraft interpolation method was used to determine updraft location and maximum rain rate centroid location (see Beatty et al. 2009; methodology). Discussion of how the study handled supercell storm splitting and merging was provided, but supercell evolution was not addressed. In their study, a storm was classified as LP/CL (forward flank precipitation mode), or HP (rear flank precipitation mode). In the current study, only two out of nine individual cases transitioned from forward flank to rear flank precipitation dominant. Why seven of the cells did not transition is unclear and puzzling given that RS98 state that most supercells will trend over time towards an HP classification.

c) Study limitations

A limitation of this study is the limited number of working cases per class (3). From a statistical standpoint, more working soundings for each classification LP/CL/HP are needed to determine what an average storm behavior storm statistics are for each classification, and then compare the composite sounding (LP/CL/HP) storm results to what the average storm (LP/CL/HP) behavior is. Another limitation is the assumption that the proximity soundings that were used are representative of the environment in which storms formed and evolved. If a proximity sounding does not provide a good representation of the actual environment of a storm, perhaps one would not expect the resulting simulated storm to provide a good representation of that class. A third limitation is that if LP/CL/HP storms are indeed sensitive to internal microphysical process (RS98), then even a perfect proximity sounding may not enable simulation of the correct precipitation mode if the microphysics are not sophisticated enough to capture all of the ice, liquid, and mixed phase processes that affect a supercell's characteristics and morphology.

The two individual cases that transitioned to a rear-flank dominant precipitation mode (one each from the LP and HP sounding classes) were compared to previous studies. RS98 hypothesized that this switch to rear-flank dominance occurs either due to hydrometeor seeding from a storm located upstream or due to weaker upper-level storm-relative winds (compared to CL and LP supercells). Brooks et al. (1994) demonstrated that in weak midlevel shear cases; the precipitation will stay near the updraft region of the supercell, which leads to the mesocyclone pulling the precipitation around the west and southwest side of the updraft. The LP and HP sounding cases herein that switch from forward to rear flank dominance occur in low-shear environments with 0-3 km SREH < 300 $m^2 s^{-2}$ - similar to what Brooks et al. (1994) and Moller et al. (1990) found for HP supercells. However, these soundings also have 9-10 km SR winds of 17.6 $m s^{-1}$ (Table 7), which is more consistent with CL supercells (RS98; Bunkers et al. 2006). Thus, the weak 0-3 km SREH and moderate 9-10 km SR winds are an insufficient condition for predicting whether the switch to occur because, other cases with even weaker 0-3 km SREH and weaker 9-10 km SR winds do not make the switch, (Table 7). Also, the LP and HP soundings that make the switch have BL-9 km shear magnitudes that unexpectedly fall on the high end of the HP BL-9 km shear magnitude distribution meaning that there are other HP sounding cases with weaker BL-9 km shear magnitudes that do not make a switch form forward to rear flank precipitation dominance.

Table 7. Characteristics associated with the working cases from each group and with the corresponding composites. Shown are Bunker's storm motion, 0-1 km SREH, 0-3 km SREH, 9 km SR wind, 10 km SR wind, 9-10 km average SR wind, BL-9 km wind magnitude difference, and 4-10 km wind magnitude difference. The two individual cases that transitioned into a rear flank dominant supercell are emboldened.

Class	Case	Bunkers Storm Motion	0-1 km SREH	0-3 km SREH	9 km SR	10 km SR	9-10 km avg. SR	BL-9 km mag. diff.	4-10 km mag. diff.
LP	LPKAMA27041976	15.1@115°	137	194	26.3	26.5	26.4	36.0	21.5
	LPKDDC01071993	13.1@88°	61	226	14.2	17.5	15.9	23.0	7.8
	LPKOUN20061979	**14.6@114°**	**98**	**203**	**17.6**	**17.6**	**17.6**	**29.4**	**10.7**
	Avg. of above 3		99	208	20.0	21.0	19.9	29.4	13.3
	LP Feature Average	13.2@107	82	174	17.6	20.2	18.9	25.6	8.9
	LP Height Average	14.1@107	82	180	18.4	18.8	18.6	28.5	10.7
CL	CLKAMA25051999	16.6@122°	104	240	18.6	18.6	18.6	34.9	9.0
	CLKOUN12041991	14.6@120°	145	187	13.2	13.0	13.1	25.2	6.1
	CLKOUN26041991	14.5@118°	194	341	15.7	25.7	20.7	26.0	15.9
	Avg. of above 3		148	256	15.9	19.5	17.5	28.7	10.3
	CL Feature Average	15.5@120.3	143	227	20.5	23.1	21.8	32.8	15.5
	CL Height Average	15.6@122.9	143	233	17.2	20.5	18.9	31.1	12.8
HP	HPKAMA11051982	22@108°	323	424	5.9	4.8	5.3	23.0	5.5
	HPKOUN07061993	15.3@163°	70	64	13.8	16.8	15.3	23.9	8.1
	HPKOUN02091992	**15@133°**	**85**	**117**	**17.6**	**17.6**	**17.6**	**29.3**	**7.3**
	Avg. of above 3		159	202	12.4	13.1	12.7	25.4	7.0
	HP Feature Average	16@133.2	134	214	14.4	15.4	14.9	27.2	6.7
	HP Height Average	16.3@131.5	133	177	11.5	10.9	11.2	24.2	6.2

The 4-10 km shear magnitude and 9-10 km storm relative average winds are consistent, as both fall in the HP regime near the mean values of the HP distribution (refer to Fig. 11a). When looking at identical thermodynamic environments that have different upper-level storm relative winds, it is clear that the upper level storm relative winds influence the overall distribution of hydrometeors (see Fig. 35). It is unclear exactly how the transition from forward flank to rear flank dominance occurs, since this particular set of experiments only has two such shifts. Further investigation with a case study is needed for the two transitioning cases, and perhaps after a larger database of soundings is developed for each classification.

d) Future work recommendations

A recommendation from the current study is that there may be more value in simulating each case individually, as compared to creating a composite sounding using either the feature or height average method. It was found that the compositing technique does not always produce a storm that has average storm characteristics based off of the run statistics from the individual cases that behaved consistently within a particular class. Also, because of the lack of consistency in behavior within some classes, it is unclear how well the feature and height averaged composites would represent those classes.

Another recommendation is that feature average compositing should be preferred when one wants to preserve BL moisture structure, including the top of the BL near the capping inversion. The feature average techniques produces higher CAPE and typically lower CIN values using a lowest-100 mb mixed-layer parcel, regardless of which moisture parameter was used in the averaging. Because the feature average technique does not "smear out" larger moisture values in the BL with lower moisture values within the capping inversion, then the feature average technique maintains larger moisture values through a greater depth in the boundary layer, which manifests as larger mixed-layer CAPE.

Third, if future simulations are performed to understand the role of upper-level storm relative winds, perhaps a greater number of soundings with weaker shear would help to elucidate the behavior of the precipitation field being orientated with the upper-level storm relative winds (Fig. 40). This study will impact future modeling research providing a baseline for such work as: this study provides a list of soundings that can be used by others to further study transitioning behavior to see why some storms transition into other classifications of supercells while others do not. This modeling study is believed to be one of the first to have provided single soundings that are associated with such transitioning in a three dimensional *idealized* cloud model. Finley et al. (2001) analyzed a simulated supercell case using the Regional Atmospheric Modeling System (RAMS) version three, which provides horizontally inhomogeneous simulations (not idealized) similar to the Weather Research Forecast Model (WRF). Finley's simulation produced a brief CL supercell that first transitioned into an HP supercell, and then subsequently transitioned to a bow echo. Despite the identification of "transitioning soundings", the behavior observed herein is inconsistent with the findings of RS98, wherein the majority of supercells in nature transition to an HP mode before demise.

Future work will include simulations using each of the soundings from working cases and feature and height average composite soundings with a simple liquid-only microphysical parameterization scheme. If the results are reproducible using simpler microphysics, then the storm's shear environment and sedimentation is likely dominating the storm precipitation mode. If not, then microphysics likely (also) plays a significant role. “Reproducible” would be measured using spatial reflectivity structure, reflectivity orientation relative to the updraft (similar modified Beatty analysis results), intensity, and longevity (similar updraft strength and updraft helicity trends). This would follow Brooks et al. (1994), who suggested that mesocyclone strength and midlevel winds seemed to determine supercell precipitation classification. If the results are not reproducible, then perhaps more sophisticated microphysics will be needed—e.g., more ice species represented. Other possible experiments could pair current HP feature and height average thermodynamic soundings with the Bunkers (2000) highly deviant HP hodograph composite.

APPENDICES

Appendix A

Predicting Supercell Motion from Environmental Wind Hodographs

There have been numerous methods for predicting supercell storm motion given the environmental wind profile: Maddox 1976, Davies and Johns 1993, Rasmussen and Blanchard 1998, and Bunkers 2000. The mean wind does not work well because the supercell propagates to the right of the mean wind. The mean wind is sometimes determined by the storm relative winds from the surface to 200 mb (Maddox 1976) and sometimes by the air density weighted mean winds from 0 to 6 km (Weisman and Klemp 1982). Previously used to adjust from the mean wind was to take 75% of the mean wind speed and 30 degrees to the right of the mean wind direction (Maddox 1976), which is abbreviated as 30R75, to determine supercell storm motion. Davies-Jones (1993) modified Maddox's methodology by only using 30R75 for a mean wind less than 15 m s^{-1} and otherwise using 20 degrees to the right of the mean wind direction at 85% of the mean wind speed, abbreviated 20R85. However, Davies (1998) found that the storm motion can be much more than 30 degrees to the right of the mean winds when the mean winds are weak. To remedy these issues, Rasmussen and Blanchard (1998; RB98) developed a shear-relative storm motion prediction method based upon 45 isolated supercell cases from the Central and Southern Plains. It is calculated as an 8.6 m s^{-1} deviation from the 0-0.5 to 4 km wind shear vector orthogonal to the shear vector and starting at the point that is 60% of the magnitude of the shear. Unlike the other methods discussed above, the RB98 method is Galilean invariant, and most similar to what has become the most popular method: the Bunkers et al. (2000) "internal dynamics (ID) method". Bunkers et al. (2000) improved upon Rasmussen and Blanchard by including many more supercell cases and found it performed best in minimizing the absolute mean error between the predicted and actual storm motions compared to the other methods mentioned above. Bunkers et al. additionally divided their soundings into typical and atypical, where atypical hodographs were subjectively defined with 0-6 km mean wind less than 10 m s^{-1} or those with both surface wind magnitude of greater than 5 m/s and a northwesterly flow at the surface (Bunkers 2000). Composite hodographs for both the typical and atypical supercell datasets did not reveal any significant differences in vertical wind shear between the two environments (c.f., Fig. 5 of Bunkers et al. 2000).

Appendix B

Algorithm Modrich

The “Modrich” algorithm, developed by UND Assistant Professor, Dr. Matthew Gilmore, modifies the thermodynamic (or wind) profile on a sounding so that the moist Richardson Number (hereafter *Ri*) becomes greater than 0.25 everywhere in the sounding, and is defined by the following:

$$Ri = \frac{g\frac{\partial\theta}{\partial z}}{\theta\left(\frac{\partial V}{\partial z}\right)^2} \qquad \text{(1B).}$$

If *Ri* for any layer in the sounding is less than 0.25, any perturbation to the layer will cause overturning within the absolutely unstable layer and possibly initiate new convection in the model domain if near saturation, which may interfere with the main supercell storm. Thus, it is desirable to modify such layers so that such overturning does not occur. The first step in the algorithm is to calculate the moist *Ri* for every layer to determine if it is less than 0.25. The algorithm starts at the top of the sounding and works towards the surface because most changes are usually located at the bottom of the soundings (where a superadiabatic layer or extreme low-level vertical wind shear layer is usually located). Thus, this results in less change to the overall sounding. This is because any required changes to the lower level of a layer are automatically propagated as a constant through the rest of the sounding in the direction that the algorithm is progressing (either up or down) so that the original lapse rate and/or vertical wind shear is maintained for subsequent layers until the algorithm judges that layer. The algorithm will modify the profile of either lapse rate or shear such that the moist *Ri* is greater than a value set by the user (herein 0.251 which is about the minimum necessary to prevent spontaneous overturning). Herein, it was decided to not modify the vertical wind shear due to its importance on supercell storms. Only the lapse rates are modified.

For each layer considered, theta and q_v are adjusted iteratively in a loop until the *Ri* is greater than or equal to 0.251 for that layer. When marching downward, this means the lowest point is cooled such that *Ri* increases. The q_v of the lower point of the layer is also moistened such that its θ_w of that point is maintained. However, if cooled past the point of saturation, the q_v value is automatically adjusted such that *RH* is 95% instead of 100%. This re-defines the T_d point at that bottom of the layer. If *RH*=100%, an undesirable layer of clouds would form. The new θ value is diagnosed iteratively for the lowest point by the new q_v values and θ_v from the sounding using the following:

$$\theta = \frac{\theta_{v\_sounding}}{\left(\frac{1+\left(\frac{qv}{\epsilon}\right)}{1+qv}\right)}, \tag{1}$$

the new θ values are calculated. The next step determines if there are any levels of supersaturation resulting from the modified theta and, if so, lowers the q_v to 95% of its saturated value. This is determined by calculating new saturation vapor pressures from the new q_v and θ values.

The code can also be run such that shear is reduced (instead of thermodynamics) to achieve a *Ri* value of .251, however, that is not used herein. It is important to realize that modification of moist Richardson Number occurs just prior to running the model. The soundings presented elsewhere in this thesis are showing the environment ***before*** the modrich is applied.

Appendix C

An Alternative Feature-Averaging Technique

Recall that herein, a feature is defined by one of the following: a single point, linear (two points), or nonlinear (approximated with three points – two linear segments). Because the averaging is done at the separate points for higher altitude point "a" and lower altitude point "b", the average lapse rate that is created is

$$\bar{L} = \frac{\bar{\theta}_a - \bar{\theta}_b}{\bar{z}_a - \bar{z}_b} \tag{1C}$$

One may substitute (2) and (3) into (1A) resulting in

$$\bar{L} = \frac{\frac{\sum(\theta_{1a}+\theta_{2a}+\cdots+\theta_{na})}{n_a} - \frac{\sum(\theta_{1b}+\theta_{2b}+\cdots+\theta_{nb})}{n_b}}{\frac{\sum(z_{1a}+z_{2a}+\cdots+z_{na})}{n_a} - \frac{\sum((z_{1b}+z_{2b}+\cdots+z_{nb}))}{n_b}} \tag{2C}$$

and assuming that there is a feature "b" for every sounding that has a feature "a", then $n_a = n_b$ and those terms cancel giving, after rearrangement,

$$\bar{L} = \frac{\sum(\theta_{1a}-\theta_{1b})+(\theta_{2a}-\theta_{2b})+\cdots+(\theta_{na}-\theta_{nb})}{\sum(z_{1a}-z_{1b})+(z_{2a}-z_{2b})+\cdots+(z_{na}-z_{nb})} \tag{3C}$$

or

$$\bar{L} = \frac{\sum(\Delta\theta_1+\Delta\theta_2+\cdots+\Delta\theta_n)}{\sum(\Delta z_1+\Delta z_2+\cdots+\Delta z_n)} \tag{4C}$$

An alternative feature average technique (not used in the current study) would average the lapse rate between *n* soundings located between features "*a*" and "*b*" that are located through depth Δz, and this is denoted by:

$$\bar{L}_{r2} = \frac{\sum\left[\frac{\Delta\theta_1}{\Delta z_1}+\frac{\Delta\theta_2}{\Delta z_2}+\cdots+\frac{\Delta\theta_n}{\Delta z_n}\right]}{n} \tag{5C}$$

Note that (4C) and (5C) are not equivalent. In 5C, the lapse rates themselves are averaged whereas in 4C, the lapse rates arise as a consequence from independently averaging points at different levels. Preliminary testing using two soundings and a variety of lapse rates has shown that neither method consistently changes the resulting sounding lapse rate and associated parameters. Thus, because the differences appear to be random and not systematic, there is little motivation here for re-doing all of the composite soundings.

Table C1. Shows the different between averaging for a point, which was preform in current study (Method 1) and lapse rate method that averages lapse rates instead points (Method 2).

Example1

This case starts with different lapse rates spread over different dz

			Method 1	**Method 2**	
	Sounding1	Sounding2		From Avg. Lapse Rate	
theta1 (K)	300.00	300.00	300.00		300.00
theta2 (K)	301.00	301.00	301.00		301.07
ht1 (km)	0	0	0		0
ht2 (km)	0.75	1.25	1.00		1.00
Lapse Rate	1.33333333	0.8	1.00		1.07
				Method2 has more CIN (less steep lapse rate)	

Example2

This case starts with different lapse rates spread over different dz

			Method 1	**Method 2**	
	Sounding1	Sounding2		From Avg. Lapse Rate	
theta1 (K)	302.00	300.00	301.00		301.00
theta2 (K)	302.00	301.00	301.50		301.40
ht1 (km)	0	0	0		0
ht2 (km)	0.75	1.25	1.00		1.00
Lapse Rate	0	0.8	0.50		0.40
				Method2 has less CIN (steeper lapse rate)	

The application of this method from (5C) is slightly different and it is direction dependent. For instance, moving down the sounding will result in a different answer than moving up the sounding.

Appendix D

Table D1. Wind hodograph indices such as storm-relative (SR) helicity, storm relative winds, and wind shear between two levels for indices for soundings associated with a sustained simulated supercell lasting more than 2 hours. SR quantities use an estimated supercell storm motion based the ID method of Bunkers et al. (2000).

Class	Case	Bunkers Storm Motion	0-1 km SR Helicity	0-3 km SR Helicity	9 km SR wind	10 km SR wind	9-10 km layer average SR wind	BL-9 km wind magnitude difference	4-10 km wind magnitude difference
LP	LPKAMA27041976	15.1@115°	137	194	26.3	26.5	26.4	36.0	21.5
	LPKDDC01071993	13.1@88°	61	226	14.2	17.5	15.9	23.0	7.8
	LPKOUN20061979	14.6@114°	98	203	17.6	17.6	17.6	29.4	10.7
	Avg. of above 3		**99**	**208**	**20.0**	**21.0**	**19.9**	**29.4**	**13.3**
	LP Feature Average	13.2@107	82	174	17.6	20.2	18.9	25.6	8.9
	LP Height Average	14.1@107	82	180	18.4	18.8	18.6	28.5	10.7
CL	CLKAMA25051999	16.6@122°	104	240	18.6	18.6	18.6	34.9	9.0
	CLKOUN12041991	14.6@120°	145	187	13.2	13.0	13.1	25.2	6.1
	CLKOUN26041991	14.5@118°	194	341	15.7	25.7	20.7	26.0	15.9
	Avg. of above 3		**148**	**256**	**15.9**	**19.5**	**17.5**	**28.7**	**10.3**
	CL Feature Average	15.5@120.3	143	227	20.5	23.1	21.8	32.8	15.5
	CL Height Average	15.6@122.9	143	233	17.2	20.5	18.9	31.1	12.8
HP	HPKAMA11051982	22@108°	323	424	5.9	4.8	5.3	23.0	5.5
	HPKOUN07061993	15.3@163°	70	64	13.8	16.8	15.3	23.9	8.1
	HPKOUN02091992	15@133°	85	117	17.6	17.6	17.6	29.3	7.3
	Avg. of above 3		**159**	**202**	**12.4**	**13.1**	**12.7**	**25.4**	**7.0**
	HP Feature Average	16@133.2	134	214	14.4	15.4	14.9	27.2	6.7
	HP Height Average	16.3@131.5	133	177	11.5	10.9	11.2	24.2	6.2

Table D2. Thermodynamic sounding indices for soundings associated with a sustained simulated supercell lasting more than 2 hours. These parameters are derived from the original soundings (before algorithm “modrich”).

LP Soundings	CAPE	CIN	LCL level AGL	LFC level AGL	PW
KAMA27041976	2132	6	709	1086	0.97
KDDC01071993	3570	9	1310	1461	1.65
KOUN20061979	1261	209	1322	2618	1.61
Avg.	**2321**	**74**	**1114**	**1721**	**1.41**
CL Soundings					
KAMA25051999	1273	48	917	1487	1.10
KOUN12041991	2830	12	825	1597	1.20
KOUN26041991	4151	13	790	1109	1.52
Avg.	**2752**	**24**	**844**	**1398**	**1.27**
HP Soundings					
KAMA11051982	1492	98	1152	2157	0.67
KOUN07061993	3318	7	641	807	1.71
KOUN02091992	2616	126	1095	2616	1.69
Avg.	**2475**	**77**	**963**	**1860**	**1.36**

Appendix E

Table E1. A list of storm locations and corresponding sounding locations and dates that were used in the current study.

Type	Storm Location	Date	Sounding Location	Source
LP	Illif, CO	1-Jul-89	North Platte, NE	RS98
	MacDonald, KS	1-Jul-93	Dodge City, KS	RS98
	Dodge City, KS	30-May-78	Dodge City, KS	RS98
	Wilbarger, TX	13-May-89	Norman, OK	RS98
	Norman, OK	20-Jun-79	Norman, OK	RS98
	Guthrie, OK	13-Jun-98	Norman, OK	Beatty
	Texas Panhandle	18-May-90	Amarillo, TX	RS98
	Western Texas	27-Apr-76	Amarillo, TX	RS98
	Lubbock, TX	25-May-94	Midland, TX	RS98
	Western Texas	26-Apr-76	Midland, TX	RS98
CL	Broken Bow, NE	1-Jun-90	North Platte, NE	RS98
	Grand Island, NE	3-Jun-80	North Platte, NE	RS98
	Alma, NE	30-May-91	North Platte, NE	RS98
	Hays, KS	10-May-85	Dodge City, KS	RS98
	Central OK	3-May-99	Norman, OK	Beatty
	Enid, OK	12-Apr-91	Norman, OK	RS98
	Geary, OK	15-May-90	Norman, OK	RS98
	Red Rock, OK	26-Apr-91	Norman, OK	RS98
	Near Lubbock, TX	25-May-99	Amarillo, TX	Beatty
	Tulia, TX	28-May-80	Amarillo, TX	RS98
HP	Beloit, KS	15-Jun-92	Topeka, KS	RS98
	Southern, NE	16-Jun-90	Topeka, KS	RS98
	Orla, TX	22-May-92	Midland, TX	RS98
	Goodland, KS	28-Jun-89	Dodge City, KS	RS98
	Memphis, TX	11-May-82	Amarillo, TX	RS98
	Wellington, TX	29-May-80	Amarillo, TX	RS98
	Kaw Reservoir, OK	6-May-94	Norman, OK	RS98
	Altus, OK	7-Jun-93	Norman, OK	RS98
	Purcell, OK	2-Sep-92	Norman, OK	RS98

Appendix F

Table F1. A list of acronyms and definitions used throughout the current study in order of occurrence.

Acronym	Definitions
NOAA	National Oceanic and Atmospheric Administration
LP	Low Precipitation supercell
CL	Classic supercell
HP	High Precipitation supercell
RS98	Rasmussen and Straka 1998
LCL	Lifted Condensation Level
CAPE	Convective Available Potential Energy
CIN	Convective Inhibition
LFC	Level of Free Convection
RH	Relative Humidity
PW	Precipitable Water
SBCAPE	Surface Based Convective Available Potential Energy
SBCIN	Surface Based Convective Inhibition
SBLCL	Surface Based Lifted Condensation Level
SBLFC	Surface Based Level of Free Convection
q	mixing ratio
ρ	air density
BF76	Browning and Foote 1976
CM1	Cloud Model 1
θ	Potential temperature
u	east-west component of the wind
v	north-south component of the wind
T_d	Dewpoint temperature
θ_w	Wet-bulb potential temperature
BL	Boundary Layer
AGL	Above Ground Level
ID	Internal Dynamics
z	height
EML	Elevated Mixed Layer
θ_e	Equivalent Potential Temperature
Ri	Richardson Number
MLCAPE	Mixed Layer Convective Available Potential Energy
MLCIN	Mixed Layer Convective Inhibition
MLLCL	Mixed Layer Lifted Condensation Level
MLLFC	Mixed Layer Level of Free Convection
e	vapor pressure
e_s	saturation vapor pressure
W-forcing	Updraft nudging technique used in CM1
LFO	Microphysical parameterization scheme named after Lin, Farley, and Orville
WC	Working Cases
UH	Updraft Helicity
SREH	Storm Relative Environmental Helicity

REFERENCES

Beatty, K., E. N. Rasmussen, and J. M. Straka, 2008: The supercell spectrum. Part I: A review of research related to supercell precipitation morphology. *Electronic J. Severe Storms Meteorology*, **3(4)**, 1-21.

––, ––, ––, and L. R. Lemon, 2009: The supercell spectrum. Part II: A semi-objective method for radar classification of supercell type. *Electronic J. Severe Storms Meteorology*, **4(1)**, 1-12.

Beebe, R. G., 1955: Types of airmasses in which tornadoes occur. *Bull. Amer. Meteor. Soc.,* **36,** 349–350.

Blanchard, D. O., 2011: Supercells in environments with atypical hodographs. *Wea. Forecasting*, **26**, 1075–1083.

Bluestein, H. B., and C. R. Parks, 1983: A synoptic and photographic climatology of low-precipitation severe thunderstorms in the southern plains. *Mon. Wea. Rev.,* **111**, 2034- 2046.

––, and Peter C. Banacos, 2002: The vertical profile of wind and temperature in cyclones and anticyclones over the eastern two-thirds of the United States: A climatology. *Mon. Wea. Rev.*, **130**, 477–506.

––, and G. R. Woodall, 1990: Doppler-radar analysis of a low-precipitation severe storm. *Mon. Wea. Rev.*, **118**, 1640–1665.

Bohren, F. C., *Clouds in a Glass of Beer*. (Stephen Kippur, 1987), pp. 17.

Bolton, David, 1980: The computation of equivalent potential temperature. *Mon. Wea. Rev.*, **108**, 1046–1053.

Brooks, H. E., C. A. Doswell, and R. B. Wilhelmson, 1994: The role of midtropospheric winds in the evolution and maintenance of low-level mesocyclones. *Mon. Wea. Rev.*, **122**, 126–136.

Brown, R. A., 1993: A compositing approach for preserving significant features in atmospheric profiles. *Mon. Wea. Rev.*, **121**, 874- 880.

Browning, K.A. and G. B. Foote, 1976: Airflow and hail growth in supercell storms and some implications for hail suppression. *Quart. J Roy. Meteor. Soc.,* **102,** 499-534.

Bryan, George H., and J. M. Fritsch, 2002: A Benchmark Simulation for Moist Nonhydrostatic Numerical Models. *Mon. Wea. Rev.*, **130**, 2917–2928.

Bunkers, M. J., B. A. Klimowski, J. W. Zeitler, R. L. Thompson, and M. L. Weisman, 2000: Predicting supercell motion using a new hodograph technique. *Wea. Forecasting*, **15**, 61–79.

——., 2002: Vertical wind shear associated with left-moving supercells. *Wea. Forecasting*, **17**, 845–855.

——., M. R. Hjelmfelt, and P. L. Smith, 2006: An observational examination of long-lived supercells. Part I: Characteristics, evolution, and demise. *Wea. Forecasting*, **21**, 673–688.

——., J. S. Johnson, L. J. Czepyha, J. M. Grzywacz, B. A. Klimowski, and M. R. Hjelmfelt, 2006: An observational examination of long-lived supercells. Part II: Environmental conditions and forecasting. *Wea. Forecasting*, **21**, 689–714.

Burgess, D. W., and R. P. Davies-Jones, 1979: Unusual tornadic storms in eastern Oklahoma on 5 December 1975. *Mon. Wea. Rev.*, **107**, 451–457.

Cohen, C., and E. W. McCaul, 2006: The sensitivity of simulated convective storms to variations in prescribed single-moment microphysics parameters that describe particle Distributions, sizes, and numbers. *Mon. Wea. Rev.*, **134**, 2547–2565.

Cronce, L. (2006). Hail embryo differences between simulated High Plains and Oklahoma storms. Unpublished master thesis, University of Illinois Urbana-Champaign, Champaign, Illinois.

Darkow, G. L., 1969: An analysis of over sixty tornado proximity soundings. Preprints, *Sixth Conf. on Severe Local Storms,* Chicago, IL, Amer. Meteor. Soc., 218–221.

Davies-Jones, R. P., 2002: Linear and nonlinear propagation of supercell storms. *J. Atmos. Sci.*, **59**, 3178–3205.

–––, (2003) Reply. *J. Atmos. Sci.* **60**:19, 2420-2426.

–––, 2008: Can a descending rain curtain in a supercell instigate tornadogenesis barotropically? *J. Atmos. Sci.*, **65**, 2469–2497.

Doswell, C. A., and E. N. Rasmussen, 1994: The effect of neglecting the virtual temperature correction on CAPE calculations. *Wea. Forecasting*, **9**, 625–629.

Dye, J. E., and P. V. Hobbs, 1968: The influence of environmental parameters on the freezing and fragmentation of suspended water Drops. *J. Atmos. Sci.*, **25**, 82–96.

Fawbush, E. J., and R. C. Miller, 1952: A mean sounding representative of the tornadic airmass environment. *Bull. Amer. Meteor. Soc.,* **33,** 303–307.

–––, and –––, 1954: The types of air masses in which North American tornadoes form. *Bull. Amer. Meteor. Soc.,* **35,** 154–165.

Fujita, T. T., 1975: New evidence from the April 3–4, 1974 tornadoes. *Preprints, Ninth Conf. on Severe Local Storms*, Norman, OK, Amer. Meteor. Soc., **107**, 248–255.

Finley, Catherine A., W. R. Cotton, and R. A. Pielke, 2001: Numerical simulation of tornadogenesis in a high-precipitation supercell. Part I: Storm evolution and transition into a bow echo. *J. Atmos. Sci.*, **58**, 1597–1629.

Gilmore, M. S. and L. J. Wicker, 1998: The influence of midtropospheric dryness on supercell morphology and evolution. *Mon. Wea. Rev.*, **126**, 943–958.

—–, J. M. Straka, and E. N. Rasmussen, 2004a: Precipitation and evolution sensitivity in simulated deep convective storms: Comparisons between liquid-only and simple ice and liquid phase microphysics*. *Mon. Wea. Rev.*, **132**, 1897–1916.

—–, —–, and —–, 2004b: Precipitation uncertainty due to variations in precipitation particle parameters within a simple microphysics scheme. *Mon. Wea. Rev.*, **132**, 2610-2627.

—–, —–, R. B. Wilhelmson, S. van den Heever, and W. Cotton, 2004c: Constant slope or constant intercept? The impact on precipitation using single-moment microphysics. *14th International Conference on Clouds and Precipitation*, Bologna, Italy. July 2004.

Humphreys, W. J., 1964: *Physics of the Air*. 3d ed. Dover, 676 pp.

James, R. P., J. M. Fritsch, and P. M. Markowski, 2005: Environmental distinctions between cellular and slabular convective lines. *Mon. Wea. Rev.*, **133**, 2669–2691.

Kain, J. S., S. R. Dembek, S. J. Weiss, J. L. Case, J. J. Levit, and R. A. Sobash, 2010: Extracting unique information from high-resolution forecast models: Monitoring selected fields and phenomena every time step. *Wea. Forecasting*, **25**, 1536–1542.

Klemp, J. B., and R. Rotunno, 1983: A study of the tornadic region within a supercell thunderstorm. *J. Atmos. Sci.*, **40**, 359–377.

Koenig, L. Randall, 1963: The glaciating behavior of small cumulonimbus clouds. *J. Atmos. Sci.*, **20**, 29–47.

—–, 1965: Drop freezing through drop breakup. *J. Atmos. Sci.*, **22**, 448–451.

Kundu, P. K., *Fluid Mechanics*, 1990, Academic Press, 638 pp.

Lucas, C. and E. J. Zipser, 2000: Environmental variability during TOGA COARE. *J. Atmos. Sci.*, **57**, 2333–2350.

Maddox, R. A., 1976: An evaluation of tornado proximity wind and stability data. *Mon. Wea. Rev.*, **104**, 133–142.

Magnus, G., 1844: Versuche uber die spannkrafte des wasserdampfes. *Ann. Phys. Chem.,* **61**, 225.

McCaul, E. W., C. Cohen, and C. Kirkpatrick, 2005: The sensitivity of simulated storm structure, intensity, and precipitation efficiency to environmental temperature. *Mon. Wea. Rev.*, **133**, 3015–3037.

Market, P. S., A. M. Oravetz, D. Gaede, E. Bookbinder, A. R. Lupo, C. J. Melick, L. L. Smith, R. Thomas, R. Redburn, B. P. Pettegrew, and A. E. Becker, 2006: Proximity soundings of thundersnow in the central United States. *J. Geophys. Res.*, 111, D19208.

Markowski, P. M., 2002: Hook echoes and rear-flank downdrafts: A review. *Mon. Wea. Rev.*, **130**, 852–876.

––, J. M. Straka, and E. N. Rasmussen, 2003: Tornadogenesis resulting from the transport of circulation by a downdraft: Idealized numerical simulations. *J. Atmos. Sci.*, **60**, 795–823.

McPherson, R. A., and K. K. Droegemeier, 1991: Numerical predictability experiments of the 20 May 1977 Del City, OK supercell storm. *Preprints, 9th Conf. on Numerical Weather Prediction*, Denver, CO, Amer. Meteor. Soc., 734-738.

Miller, L. J., J. D. Tuttle, and G. B. Foote, 1990: Precipitation production in a large Montana hailstorm: Airflow and particle growth trajectories. *J. Atmos. Sci.,* **47,** 1619–1646.

Moller, A. R., C. A. Doswell, M. P. Foster, and G. R. Woodall, 1994: The operational recognition of supercell thunderstorm environments and storm structures. *Wea. Forecasting*, **9**, 327–347.

——, ——, and R. Pryzybylinski, 1990: High precipitation supercells: A conceptual model and documentation. Preprints, *16th Conf. on Severe Local Storms,* Kananaskis Park, Alberta, Canada, Amer. Meteor. Soc., 52-57.

Morrison, H., J. A. Curry, and V. I. Khvorostyanov, 2005: A new double-moment microphysics parameterization for application in cloud and climate models. Part I: Description. *J. Atmos. Sci.*, **62**, 1665–1677.

Naylor, J., M. S. Gilmore, R. L. Thompson, R. Edwards, and R. B. Wilhelmson, 2012: Comparison of objective supercell identification techniques using an idealized cloud model. *Mon. Wea. Rev., In press*

——, and ——, 2012: Convective initiation in an idealized cloud model using an updraft nudging technique. *Mon. Wea. Rev., In press*

Nelson, S. P., 1987: The hybrid multicellular–supercellular storm—an efficient hail producer. Part II: General characteristics and implications for hail growth. *J. Atmos. Sci.*, **44**, 2060–2073.

NOAA, 1997: *Rawinsonde and Pibal Observations, Federal Meteorological Handbook No. 3, FCM-H3-1997*, U.S. Dept of Commerce/NOAA, 191 pp. [Available online at http://www.ofcm.gov/fmh3/text/default.htm]

——, 2006: NWS Storm Prediction Center. [Available online at http://www.spc.noaa.gov/]

Rasmussen, E. N., and J. M. Straka, 1998: Variations in supercell morphology. Part I: Observations of the role of upper-level storm-relative flow. *Mon. Wea. Rev.*, **126**, 2406- 2421.

Ramsay, H. A., and C. A. Doswell, 2005: A sensitivity study of hodograph-based methods for estimating supercell motion. *Wea. Forecasting*, **20**, 954–970.

Rotunno, R., and J. Klemp, 1985: On the rotation and propagation of simulated supercell thunderstorms. *J. Atmos. Sci.*, **42**, 271–292.

Straka, J. M., and M. S. Gilmore, 2006: Does the influence of oblate-like distortions in larger raindrops make a difference in collection and evaporation parameterizations? *J. Appl. Meteor. Climatol.*, **45**, 1582–1591.

Tessendorf, S. A., L. J. Miller, K. C. Wiens, and S. A. Rutledge, 2005: The 29 June 2000 supercell observed during STEPS. Part I: Kinematics and microphysics. *J. Atmos. Sci.*, **62**, 4127–4150.

Thompson, R. L., R. Edwards, J. A. Hart, K. L. Elmore, and P. Markowski, 2003: Close proximity soundings within supercell environments obtained from the rapid update cycle. *Wea. Forecasting*, **18**, 1243–1261.

Tsonis, A. A., *An Introduction to Atmospheric Thermodynamics*, 2007, Cambridge University Press, 113 pp.

van den Heever, S. and W. R. Cotton, 2004: The impact of hail size on simulated supercell storms. *J. Atmos. Sci.*, **61**, 1596-1609.

Weisman, M. L., and J. B. Klemp, 1982: The dependence of numerically simulated convective storms on vertical wind shear and buoyancy. *Mon. Wea. Rev.*, **110**, 504–520.

——, and ——, 1984: The structure and classification of numerically simulated convective storms in directionally varying wind shears. *Mon. Wea. Rev.*, **112**, 2479–2498.

Wilhelmson, R. B., and J. B. Klemp, 1978: A numerical study of storm splitting that leads to long-lived storms. *J. Atmos. Sci.*, **35**, 1974–1986.